A Characterization Scheme to Assess the Heating Performance of Developed Biological Solders for Laser Tissue Welding

by

Michelle Dieu Thao Huynh

A thesis
presented to the University of Waterloo
in fulfillment of the
thesis requirement for the degree of
Master of Applied Science
in
Mechanical and Mechatronics Engineering (Nanotechnology)

Waterloo, Ontario, Canada, 2025

© Michelle Dieu Thao Huynh 2025

Author's Declaration

This thesis consists of material all of which I authored or co-authored: see Statement of Contributions included in the thesis. This is a true copy of the thesis, including any required final revisions, as accepted by my examiners.

I understand that my thesis may be made electronically available to the public.

Abstract

Laser tissue welding (LTW) is an alternative, suture-less wound closure technique. It involves positioning opposite wound edges in close proximity, followed by near-infrared laser irradiation until a temperature of approximately 60°C is reached. At this temperature, protein interdigitation and tissue coagulation occur, resulting in a re-homogenized continuous tissue matrix. Heat localization at the site of joining is essential to produce strong tissue bonds while minimizing thermal damage to the surrounding region. One method to achieve heat localization is through the administration of photothermally responsive biological solders (biosolders).

For the presented work, nanocomposite gels (NCGs) were developed as biosolders. They were prepared by dissolving hyaluronic acid (HA) and guar gum (GG) to a final polymeric concentration of 3% w/v in aqueous solutions with up to 1.4 nM gold nanorods (GNRs). The addition of GG was found to stabilize GNR dispersion through the gel and enhance their heat generation under laser irradiation. To assess the clinical relevance of the gel formulations, a simplified photothermal characterization scheme was developed. The method relies on a custom-built measurement system that can confine gel samples to clinically relevant thicknesses as thin as 100 μm. This setup was used to measure temperature increases (ΔT) of gel specimens with and without GNRs, with a repeatability of ΔT = 0.123°C.

A plasmonic heat amplification factor, ξ, is proposed as a new safety metric for assessing the clinical relevance of a biosolder formulation. It is defined as the ratio of ΔT for an NCG by ΔT of its corresponding control gel. A subset of the developed NCG formulations were found to possess ξ >1.3, indicating their thermal suitability for safe LTW. The presented method aims to establish a new standard foundation for the temperature monitoring of laser-irradiated gels in isolation, allowing for the cost-effective screening of preliminary NCG formulations for eventual administration to tissue models.

The developed photothermal characterization system was further used to determine the photothermal conversion efficiency, or fraction of heating power per absorbed light, η, of developed NCGs. Although a standardized method for determining η in liquid photothermal solutions has been previously proposed, it is unsuitable for semisolid materials such as viscous gels that are considered for medical applications like LTW. As such, a simple, yet robust approach is proposed for estimating η of viscous photothermal gels via the direct determination of thermal conductance. The method allows for more confident reports of η for optimizing the photothermal response of photoresponsive materials.

Acknowledgements

I would like to acknowledge my supervisor, Dr. Michael Mayer, for his guidance and support throughout my graduate studies. He has provided me with invaluable life lessons for research and personal growth. I would also like to acknowledge Kai Zhang, Jansen Zhou, Mihir Patel, and Saira Hadi, all of whom I have worked alongside on this project. As well, I am grateful to the rest of CAMJ for their shared community.

I am grateful to Dr. Shazia Tanvir and Dr. Bill Anderson for usage of their lab space and guidance for nanoparticle growth. Thank you to Dr. Bill Anderson and Dr. Elisabeth Prince for also being members of my committee. I would like to thank Dr. Charles Dal Castel and Dr. Faten Salim for their assistance with rheological measurements, Mishi Groh for providing TEM training and assistance, and Dr. Yves Leclerc for his helpful perspectives as a surgeon.

I would also like to thank my childhood friends, Sarah, Yuvik and Marissa, and university friends, Rebecca and Sahad, for keeping life entertaining despite the hardships. I want to especially thank my parents, Steven and Le Thuy, and my brother Michael for their never-ending support of my academic pursuits.

Finally, I am forever grateful to my boyfriend Jon for his love, support, and peculiar yet endearing sense of humour throughout my academic studies and beyond.

Table of Contents

Author's Declaration ii

Abstract iii

Acknowledgements iv

List of Figures ix

List of Tables xiv

Code Listings xv

List of Abbreviations xvi

1 Introduction 1

1.1 Laser Tissue Welding (LTW) 1

1.2 Literature Review 3

1.2.1 Protein Architecture and Denaturation 3

1.2.2 Role of Collagen and Hyaluronic Acid in Connective Tissue 4

1.2.3 Biological Solders (Biosolders) 6

Biosolder Classification 6

Matrices for Biosolders 6

Photoabsorbing Agents for Biosolders . . . 7
Existing Biosolder Formulations . . . 9
Biocompatibility of GNR Biosolders . . . 10
1.2.4 LTW Tissue Joining Mechanism . . . 11
1.2.5 Photothermal Conversion Efficiency (η) . . . 13
1.3 Objectives . . . 15
1.4 Statement of Contributions . . . 15
1.5 Summary . . . 16

2 Development of a Nanocomposite Gel Biosolder **17**
2.1 Summary of Seed-Mediated Growth . . . 17
2.2 Colloidal GNR Synthesis . . . 18
2.2.1 GNR Synthesis Procedure . . . 18
2.2.2 Synthesis Procedure Deviations and Justifications . . . 20
2.2.3 Post-Processing Procedure . . . 22
2.2.4 GNR Characterization . . . 24
2.3 Gel Biosolder Development . . . 25
2.3.1 Composition and Preparation . . . 25
2.3.2 Rheological Characterization . . . 30
2.3.3 Cost Breakdown for Developed Biosolder . . . 32
2.4 Summary . . . 33

3 RTD-Based Photothermal Characterization Scheme **34**
3.1 Motivation and Current Methods . . . 34
3.2 Laser-Temperature Sensor System Design . . . 35
3.3 Achieving Measurement Repeatability and Stability by Defined Geometric Arrangements . . . 41
3.4 Temperature Collection Scheme . . . 44
3.5 Cost Estimation for Characterization System . . . 46
3.6 Summary . . . 47

4 Assessing the Clinical Relevance of Developed Biosolders **48**

4.1 Main Factors for LTW with Biosolders: Quantifying Effects on Heating Performance (ΔT) using DOE/ANOVA 48

4.1.1 Design Space Selection and DOE/ANOVA Methods 48

4.1.2 DOE/ANOVA: Results and Discussion 50

4.1.3 Comparison of New Laser-NCG Configurations to Prior Literature 52

4.2 The Plasmonic Heat Amplification Factor (ξ) as a Design Metric 52

4.2.1 Thermal Damage Considerations for LTW 52

4.2.2 Predicting Clinical Relevance of Developed Biosolders for LTW 54

4.3 Summary 56

5 Alternative Method for Determining Photothermal Conversion Efficiency (η) of NCGs **57**

5.1 Motivation and Current η Determination Methodologies 57

5.2 Steady-State Simplification of η Definition 58

5.3 Experimental Determination of hA to Bypass the Usage of $\sum_i m_i C_{p,i}$ and Fitted Parameter τ_s 59

5.4 Determination of hA using RTD-Self Heating Method 59

5.5 Power Contribution of Gel Media and Glass (Q_0) 61

5.6 Determination of η for Developed Biosolders 62

5.7 Summary 64

6 Conclusions and Future Work **65**

6.1 Conclusions 65

6.2 Future Work 66

6.2.1 *Ex vivo* or *in vivo* Validation of the Design Metric, ξ 66

6.2.2 *Ex vivo* or *in vivo* Welding with Developed Biosolders 66

6.2.3 Gel Shelf-Life Testing 66

6.2.4 Cytotoxicity Testing 67

6.2.5 Laser Heating and RTD-Self Heating 67

6.2.6 Handheld Laser Design 67

Copyright Permission **68**

References **77**

APPENDICES **90**

A Biosolder-Relevant Concentration Calculations **91**

A.1 Polymer Concentration Conversions for Literature Values 91

A.2 GNR Concentration Conversions for Literature Values 92

A.3 Uncertainty in Concentration Curve-Derived Values 94

B GNR Size Distribution by ImageJ Analysis **96**

C CAD Technical Drawings **98**

C.1 Laser Holder Clamp 98

C.2 Stacked Glass Filter Holder 100

D Python Scripts for Photothermal Characterization System **101**

E Laser Spot Size Estimation **107**

F Internal SOPs **112**

F.1 Gold Nanorod Synthesis SOP 112

F.2 Preparation of Hyaluronic Acid Guar Gum Gold Nanorod Gel SOP 136

List of Figures

1.1 Visualization of the heat localization effect on tissue by biosolders during LTW. . 2

1.2 The orders of protein structure include the (a) primary structure, (b) secondary structure, (c) tertiary structure, and sometimes (d) quaternary structure. Adapted from Genetics Glossary: Protein (genome.gov). 3

1.3 Free energy landscape, or folding funnel, of a protein. Troughs in the landscape indicate unfolded conformations. Distinct regions of unfolded conformations are categorized by denaturant type. Obtained from Lapidus. 4

1.4 Hierarchical assembly of collagen fibers. Graphics from Freepik. 5

1.5 Chemical structure of hyaluronic acid. Obtained from Wikipedia (public domain image). 5

1.6 Absorption coefficient spectra of different tissue components. The NIR region (between 600 nm and 1000 nm) is termed the optical window since light penetration is highest. HHb = deoxyhemoglobin, O_2Hb = oxyhemoglobin, CtOx = cytochrome oxidase. Obtained from Scholkmann *et al*. with permission. 8

1.7 LSPR phenomenon responsible for GNR photothermal property: (a) Transverse plasmon mode, (b) Longitudinal plasmon mode. 9

1.8 Joining mechanism of the LTW process: (a) A discontinuity in the connective tissue is created by surgical incision or injury. The LTW procedure begins with (b) wound edge apposition then (c) application of a gel biosolder containing GNRs dispersed in a polymeric or protein matrix. (d) NIR laser irradiation induces amplified and localized heating mediated by the LSPR effect, resulting in protein interdigitation, and consequently (e) the formation of a tissue bond. 12

2.1 Overview of modified seed-mediated growth method for the generation of GNRs, adapted from Nikoobakht and El-Sayed's method. (a) Preparation of seed solution, (b) Preparation of growth solution, (c) Addition of seed solution to growth solution and incubation. Graphics produced with BioRender. 19

2.2 Comparison of seed solutions prepared with (a) 0.01 M $NaBH_4$ per the original protocol and (b) 0.03 M $NaBH_4$. (c) The resulting GNR solution using the seed solution in (b). 21

2.3 Absorbance spectrum for seed solution prepared with 0.03 M $NaBH_4$ (obtained with the Biotek Epoch microplate reader, path length $\approx$ 5.26 mm). Optical density (OD) is synonymous with absorbance. 21

2.4 GNR purification and size selection procedures. Graphics produced with BioRender. 22

2.5 Absorbance spectra of GNR solutions following (a) the first and second rounds of centrifugation at 6500 rpm for 15 min (obtained with the HP 8452A Diode Array spectrophotometer), (b) the third round of centrifugation at various speeds (obtained with the Biotek Epoch microplate spectrophotometer). 23

2.6 Photograph of ready-to-use GNR stock solution ($\approx$4nM–5 nM) in 1X PBS. . . . 24

2.7 Size characterization of prepared GNRs in 1X PBS. (a) TEM micrograph, obtained by Mishi Groh, (b) GNR size distribution by aspect ratio based on collected TEM micrographs (n = 144). 25

2.8 Standard curve of commercial GNRs (AR = 4.0, Nanopartz) for λ = 808 nm (n = 3). The OD values were obtained using the Biotek Epoch microplate reader. . . 26

2.9 Chemical structure of guar gum. Obtained from Wikipedia (public domain image). 26

2.10 Photographs of all nine gel formulations with varied GG and GNR concentrations 27

2.11 Overview of biosolder gel preparation with constituent material interactions highlighted. The final gel is comprised of an interpenetrating network of GG and HA chains. Graphics produced with BioRender. 28

2.12 The importance of pre-mixing GG and GNRs prior to addition to HA. There is visibly more aggregation (i.e., a greyish purple hue) in the gel where pre-mixing was omitted. The pre-mixed gel retained the pale pink colour of the GNR solution indicating dispersion stability. Middle and right gels contain 0.4 nM GNRs, 0.25% w/v GG. 29

2.13 Optical microscopy of gel specimens on stainless steel substrate without GNRs (left) and with 1.4 nM GNRs (right). 29

2.14 Rheological characterization of control gel (0 nM GNRs) and NCG (1.4 nM GNRs) containing 0.25% w/v GG. (a) Storage modulus (G') and loss modulus (G''), measured at a constant shear strain of 1%. (b) Complex viscosity ($|\eta^*|$) and loss factor ($\tan(\delta)$), measured at a constant shear strain of 1%. (c) Dynamic viscosity over shear rate. All rheology curves were obtained by Dr. Charles Dal Castel and Dr. Faten Salim at the UW Department of Chemical Engineering's Analytical Facilities. 32

3.1 Photographs of commercial thin film Pt100 RTD. From submitted manuscript. . . 36

3.2 Schematic for all connections of the integrated laser-temperature sensor system. . 37

3.3 Characterization of laser output control by PWM: (a) Operating principle of PWM with an example of 50% duty cycling, (b) Full RPi duty cycle range with the linear region limited to between 0.25 W to 3.78 W laser output, (c-d) Lower and upper edges of duty cycle-laser power relationship exhibit stepwise behaviour. 38

3.4 Photothermal characterization setup: (a) Overview of photothermal characterization system. Integrated laser control and temperature sensing is enabled by the RPi microprocessor using Python. Custom 3D-printed laser clamp allows for vertical height adjustment of the laser. (b) Detailed illustration of process zone of setup. 39

3.5 Photograph of the full benchtop photothermal characterization setup with microscope and attached glass filters for observing laser spot. 40

3.6 Photothermal characterization setup with microscope and attached glass filters for observing laser spot: (a) Front view of glass filter attachment on microscope head positioned overhead the Pt100 (b) Side view. 41

3.7 Comparison of temperature curves when a gel sample (0 nM GNRs, 0% w/v GG) is absent versus present under 2.4 W (41.3 W/cm^2) laser irradiation. The gel plays an active role in dissipating heat from the setup. Curves were obtained using the dual glass slide setup depicted in Fig. 3.4. 42

3.8 Comparison of temperature curves recorded with laser irradiation commencing at t = 0 s for various nominal gel thicknesses (a) 0.1 mm, (b) 0.4 mm, (c) 0.6 mm, (d) 1.1 mm. (e) Summarized. All curves were obtained using the dual glass slide setup in Fig. 3.4, except the distance between the collimator lens mount and fiber end is 0 mm, instead of 1.1 mm. 43

3.9 Long-term measurement stability for 150 s of continuous lasing. There were no observations of carbonization. 44

3.10 Example curves characterizing the heating behaviour of gel samples using the custom setup: (a) Gel specimens with 1.4 nM GNRs and without GNRs, (b) Gel specimens with increasing GG concentration. Laser power was 2.4 W (41.3 W/cm^2). Duration of irradiation was 30 s. 45

3.11 Overview of RTD measurement scheme for a gel sample. 45

3.12 Overview of photothermal characterization scheme for control and GNR-containing NCG biosolders. From this, biosolder-relevant properties can be determined, such as the plasmonic heat amplification factor, ξ, and the photothermal conversion efficiency, η. 46

3.13 Example data set for 10 gel samples prepared from the same batch (1.4 nM GNRs, 0.1% w/v). 47

4.1 Design space containing DOE factors and levels. The nine unique gel formulations with varied GNR concentration and GG concentration correspond to those photographed in Fig. 2.10. Graphic produced with BioRender. 49

4.2 Box and whisker plots of average ΔT of gel specimens irradiated under (a) 0.98 W, (b) 1.7 W, and (c) 2.4 W laser power, n = 10. Baseline temperatures ranged from 22.2°C –24.8°C. The asterisks indicate statistically significant differences from the corresponding control group (0% w/v GG, same GNR level) based on Tukey's HSD test; $p \leq 0.05$ (*),$p \leq 0.01$ (**), $p \leq 0.001$ (***). 50

4.3 Thermal effects expected to occur in skin tissue based on temperature and exposure. Threshold functions 1, 2, and 3 define the minimum conditions for which hyperthermia, partial thickness burn, and full thickness burn occur, respectively. (a–f) LTW process parameters from literature. 53

4.4 Effect of guar gum on plasmonic heat amplification factors for GNR-containing NCGs (n = 5). 55

5.1 Schematic of experimental setup and measurement circuit for determining thermal resistance, R_{th}. 60

5.2 Determination of thermal conductance, hA, which is the inverse of thermal resistance, Rth. (a) Measured current as a function of voltage applied to Pt100. Measurements were taken after 30 s of self-heating. (b) The inverse of the slope of the Pt100 power-temperature relationship gives hA (n = 4, reported as mean ± SD). 61

5.3 Photothermal conversion efficiencies for all GNR-containing NCG groups (n = 5). 63

6.1 First prototype of a handheld laser case with built-in tweezers. (a) Photograph of the case, (b) Different-sized finger adapters for small, medium and large hands, (c) Location for inserting tweezers at bottom of case; the tweezers snap in place, (d) Device application to a porcine skin sample. 67

B.1 Example of a raw TEM micrograph obtained using the Philips CM10 TEM. . . . 97

B.2 ImageJ analysis of a single GNR from Fig. B.1 micrograph, showing how the length is measured. The same can be done for the diameter. 97

C.1 CAD schematic for laser clamp (AutoCAD). 98

C.2 CAD schematic for the front piece of the stand clamp. Unit = mm, created in AutoCAD. 99

C.3 CAD schematic for the back piece of the stand clamp. Unit = mm, created in AutoCAD. 99

C.4 CAD schematic for stacked glass filter holder which is attached to a USB microscope head for laser spot observation. Unit = mm, created in FreeCAD. 100

E.1 Example micrograph used for laser spot size estimation for the laser configuration illustrated in Fig. 3.4: (a) Original image, (b) Processed image in ImageJ software with line plot indicated. 107

E.2 Intensity profile of the example micrograph shown in Fig. E.1. The Gaussian fitted parameters are listed as well. The black dots indicate the half-maximum points on either side of the Gaussian curve. 108

List of Tables

1.1 Summary of prior biosolder formulations and the tissue models on which they were applied. 10

2.1 Composition overview of reagent stock solutions and how often they are prepared. 18

2.2 Required stock solution volumes to prepare 5 mL seed solution and 30 mL total GNR growth solution. 20

2.3 Composition overview of all nine biosolder formulations with varying GG and GNR concentrations. The provided amounts produce 1 mL of each formulation and are based on a GNR stock concentration of 4.40 nM. 30

2.4 Cost breakdown for 1 mL of gel biosolder (1.4 nM GNRs, 0.25% w/v GG). . . . 33

3.1 Cost breakdown for photothermal characterization system. 46

4.1 Three-way ANOVA to evaluate the effect of GNR concentration, GG concentration, laser power, and two-way interactions thereof on ΔT of NCG samples irradiated for 30 s. 51

5.1 Estimated Q_0 values using developed control gel biosolders. 61

E.1 FWHM values calculated for each micrograph. 109

Code Listings

D.1 LTW class for laser control functions. 102
D.2 Python script for outputting constant laser power via PWM. 104
D.3 Python script for user-set temperature collection and concurrent laser irradiation. 104
E.1 Jupyter (Python) Notebook for estimating laser spot size. Analysis for one laser spot image is provided. 109

List of Abbreviations

AA L-ascorbic acid 17–20, 22, 33

$AgNO_3$ silver nitrate 17–20, 33

AR aspect ratio 9, 20, 22–24

AuNP gold nanoparticle 8, 11, 22

CTAB cetyltrimethylammonium bromide 10, 11, 17–20, 24, 33

CW continuous wave 36, 44

ECM extracellular matrix 4, 5, 13

FBG fiber Bragg grating 34, 35

FWHM full width at half maximum 108

GG guar gum 25–27, 31, 33, 62

GNR gold nanorod 8–11, 13, 15

HA hyaluronan or hyaluronic acid 5, 7, 11, 17, 25, 26, 31, 33, 62

$HAuCl_4 \cdot 3H_2O$ gold (III) chloride trihydrate 17–20, 33

ICG indocyanine green 7

IR infrared 34

LSPR localized surface plasmon resonance 8, 9, 11, 13, 23

LTW laser tissue welding 2, 4, 6, 7, 9, 11, 13, 15, 57

MW molecular weight 25, 26

$NaBH_4$ sodium borohydride 17–20, 33

NCG nanocomposite gel 9, 13, 15, 17, 34, 35, 42, 44–47, 54, 58

NIR near-infrared 7

PBS phosphate buffered saline 18, 23, 26, 27, 33

PWM pulse width modulation 36

RPi 2B Raspberry Pi 2 Model B 35, 36

RTD resistive temperature detector 34, 35, 38, 40, 47, 58, 60

SL:WL suture length-to-wound length ratio 33

TEM transmission electron microscopy 24

WD working distance 38

Chapter 1

Introduction

This chapter provides the necessary background information for the laser tissue welding process, as well as an overview of biological solder components, examples and formulation considerations. Discussions of tissue joining mechanisms are also provided. The derivation for photothermal conversion efficiency, η is described. The objectives of this thesis are highlighted, and a statement of contributions is provided, which lists the sections of this thesis that contain content from a manuscript submitted to a journal.

1.1 Laser Tissue Welding (LTW)

Wound closure devices employed in the current standard of care include sutures, staples, and adhesives. These devices work by bringing the wound edges in close proximity (i.e., apposition) to one another and providing mechanical support for wound healing. Although these devices—sutures, particularly—have been a historical constant for post-operative tissue repair [1], they possess several shortcomings that have inspired research towards the development of alternative methods.

Since conventional wound closure methods merely appose the wound edges to one another, the resulting bond is not always fully watertight. The major consequences of this are increased risks for bacterial infection and wound dehiscence or reopening of the wound [2, 3, 4]. Moreover, the surfaces of sutures and staples can promote bacterial adhesion, thus increasing the risk of infection to the patient [5]. Furthermore, medical adhesives can suffer from low bond strength, as well as inconsistent application by the physician [6]. Sutures and staples prove to be disadvantageous for the closure of softer tissues, like liver tissue which are susceptible to tearing.

Inadequate suturing of the liver can result in massive and intractable blood loss, while stapling the liver may result in bile leakages [7]. Even for sturdier tissues, the act of repeatedly inserting sharp implements, like sutures and staples, can increase trauma to the surgical site. For externally visible wounds, sutures are also known to create unsightly scars [1]. In addition to addressing the practical and functional shortcomings of conventional closure techniques, patients consider the improvement of the cosmetic appearance of a healed wound to be important [1].

Laser tissue welding (LTW) is a "suture-less" alternative wound closure technique that can address each of the aforementioned shortcomings of conventional techniques. LTW was first proposed in the 1970s [8] and has shown potential for accelerated healing, increased wound strength, faster procedural time, reduced scar formation, decreased infection, reduced inflammatory response, higher suitability for soft tissues, and instantaneous water-tight sealing when compared to sutures [9, 10, 11, 12]. The LTW technique involves bringing the edges of an incision or wound in close proximity, followed by laser irradiation. Typical irradiation times range from 2 min–7 min, while laser power densities range from 2 W/cm^2–35 W/cm^2 [9, 10, 13, 14, 15, 16]. Across these reports, the tissues reached temperatures of 60°C or higher. At these temperatures, protein denaturation and disassembly, and tissue coagulation occur, re-homogenizing the wound site to create a continuous tissue matrix and water-tight seal [10]. A more detailed description of these mechanisms is provided in Section 1.2.4.

To assist with heat amplification and heat localization during the LTW process, exogenous materials called biological solders (biosolders) can be applied to the apposed wound edges prior to laser irradiation (Fig. 1.1). Biosolders contain photoabsorbing agents that transduce incident laser light into heat in an amplified manner. When biosolders are selectively applied onto a tissue surface, the covered region heats under irradiation to a greater extent than the uncovered surroundings. This permits the use of a lower laser power to achieve the same level of heating as a bare laser operating at higher power, essentially localizing the heat to a specific area. The benefit of this strategy is the minimization of thermal damage to peripheral or surrounding tissue and confinement of the weld to the desired site of joining [17]. Biosolders are discussed in further detail in Section 1.2.3.

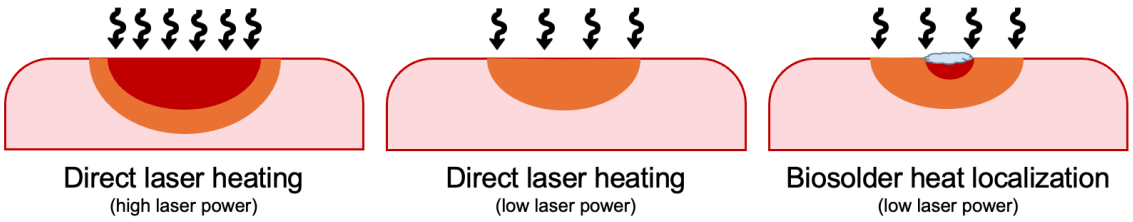


Figure 1.1: Visualization of the heat localization effect on tissue by biosolders during LTW.

1.2 Literature Review

1.2.1 Protein Architecture and Denaturation

Proteins are one of the key biological macromolecules that are necessary for life. There exist thousands of different proteins in the human body, all of which perform complex and individual biological functions. A protein is a polymer composed of monomeric amino acids, which then assemble into a functional structure through a series of hierarchical molecular interactions (Fig. 1.2). The primary structure is formed through covalent linking of amino acids in a chain-like sequence. Following this, the secondary structure is formed into a series of α-helices and β-pleated sheets. These secondary structures then undergo complex folding into the tertiary structure through an abundance of intermolecular interactions, such as hydrogen bonding, ionic forces, hydrophobic interactions, and van der Waals forces [18]. For some proteins, the tertiary structures self-assemble into a superstructure called the quaternary structure.

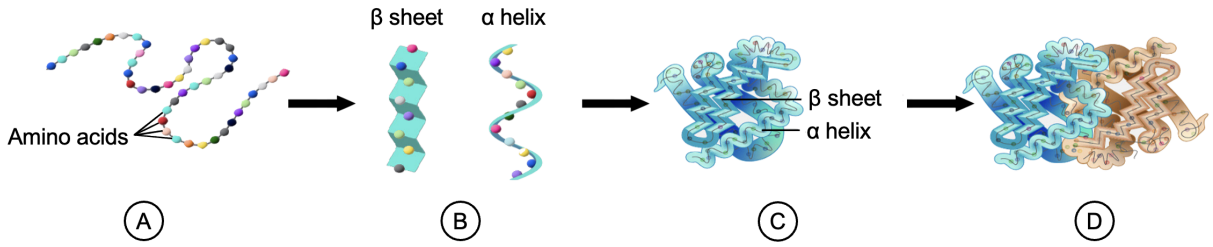


Figure 1.2: The orders of protein structure include the (a) primary structure, (b) secondary structure, (c) tertiary structure, and sometimes (d) quaternary structure. Adapted from Genetics Glossary: Protein (genome.gov).

The structural conformation of a protein is imperative to protein function since it influences the accessibility of functional groups on the surface of the protein and thus determines how it interacts with other biomolecules in the body. The process of destabilizing the tertiary structure of a protein is known as denaturation or unfolding. Denaturation occurs due to changes in the environment of the protein, such as temperature, pressure, pH, and salt concentration, or the application of chemical denaturants or microscopic forces [19, 20]. A delicate balance of these parameters is required for a protein to assume its native conformation, or the most stable conformation with the lowest free energy.

A free energy landscape, or folding funnel, is used to illustrate the conformational behaviour of a protein (Fig. 1.3) [20]. Troughs in the landscape correspond to local free energy minima

of different protein conformations (i.e., locally stable states), with the native protein state occupying the absolute free energy minimum. In a stable environment, it is thermodynamically less favourable for proteins to assume denatured, or unfolded states, as this would increase their free energy. However, if a disturbance is applied (e.g., high temperature during LTW), the favourability of unfolded states increases. This effectively "traps" the protein in a non-native state within a free energy local minimum, even after environmental conditions return to normal. Depending on the denaturant used, unfolded states occupy distinct regions of the free energy landscape [20].

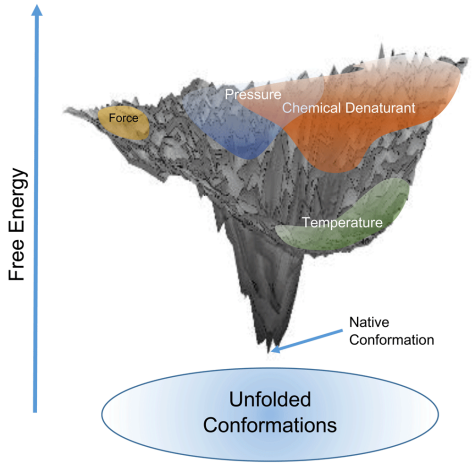


Figure 1.3: Free energy landscape, or folding funnel, of a protein. Troughs in the landscape indicate unfolded conformations. Distinct regions of unfolded conformations are categorized by denaturant type. Obtained from Lapidus [20], under a Creative Commons Attribution (CC BY) license.

1.2.2 Role of Collagen and Hyaluronic Acid in Connective Tissue

Connective tissue is important for providing mechanical support, movement, tissue fluid transport, cell migration, control of metabolic processes, and wound healing in all other tissues in the body [21]. Collagen, the most abundant protein in mammals, plays a key role in maintaining the structure of the extracellular matrix (ECM) in connective tissues [22]. Healthy and intact collagen matrices assume a quasi-crystalline, densely packed, rope-like structure. As with other proteins, the formation of the final quaternary structure of collagen requires a series of intermolecular interactions (Fig. 1.4). Briefly, three peptide chains entwine into a triple helix, called tropocollagen, via hydrogen bonding [23]. These helices then aggregate, or self-assemble to

form fibrils [24], which then assemble into fibers. Glycosylated proteins, called proteoglycans, further fortify the alignment of collagen fibers within the ECM [25]. With respect to wound healing, the synthesis and deposition of collagen is vital for restoring the physical strength of the wound site [26].

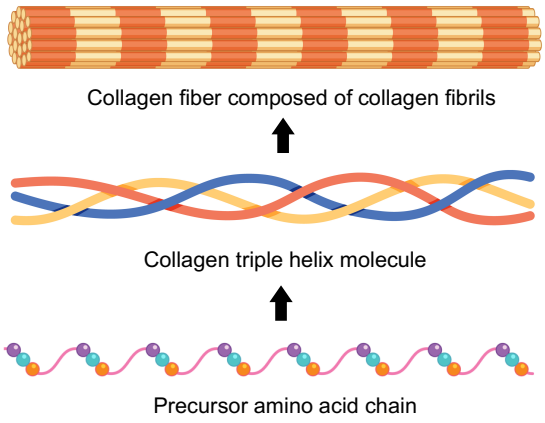


Figure 1.4: Hierarchical assembly of collagen fibers. Graphics from Freepik.

Hyaluronan or hyaluronic acid (HA) (Fig. 1.5) is ubiquitously distributed in mammalian tissues, including connective tissue [27], acting as a structural and functional support network between other tissues. HA performs critical functions during the inflammatory, proliferative and remodelling phases of wound healing. Large HA fragments couple with fibrinogen to induce clot formation at the site of injury. In addition, the abundance of large HA fragments creates a porous network by which immune cells can migrate to the wound. Conversely, small HA fragments have stimulatory properties that promote fibroblast migration and collagen production during wound healing [28].

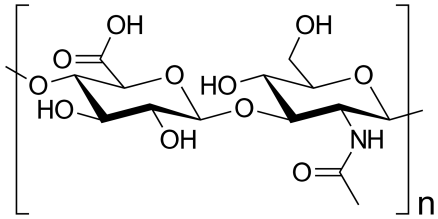


Figure 1.5: Chemical structure of hyaluronic acid. Obtained from Wikipedia (public domain image).

1.2.3 Biological Solders (Biosolders)

Biosolder Classification

In traditional soldering, the function of the solder is to act as additional filler material to bridge a connection between separate metal entities. The ideal solder is inert and has a melting temperature well below that of the joining base metals to avoid damage.

Biosolders require an altered definition. Although biosolders also act as additional filler material in the LTW process [29], they undergo interactive mechanisms with the interfaces of the biological material, making them distinct from traditional solders. To briefly describe these interactive mechanisms, the following accepted definitions of a "biosolder" from literature are provided:

1. A proteinaceous material that undergoes denaturation to form bonds with the adjacent tissue [30].
2. An exogenous (proteinaceous or polymeric) paste that coagulates on heating to form an artificial solid clot [29].
3. A topically applied semisolid material that is activated by laser light to induce thermal modifications within tissue [17].
4. A material that is interposed between wound edges to selectively absorb laser radiation and prevent thermal damage to adjacent tissue [11].

The joining mechanisms are described and illustrated in more detail in Section 1.2.4. Following laser irradiation, all biosolder material, including residual non-irradiated biosolder, is eventually broken down and cleared away by immune cells such as neutrophils through phagocytosis (the engulfing and digestion of foreign materials) [31]. This process incites the eventual resorption and clearance of the biosolder material from the body [29].

Matrices for Biosolders

The purpose of the matrix is to act as a vehicle for administering photoabsorbers to the site of joining. Natural biopolymers like proteins or polysaccharides are selected as biosolder matrices owing to their biocompatibility, biodegradability and lower likelihood of eliciting a strong immune response [32]. Moreover, it is important that the matrix material be chemically inactive to

avoid unintended reactions with the exposed tissue. Miscibility of the embedded photoabsorber within the matrix is also of importance.

Due to the key functions of collagen and HA in wound healing (as described in Section 1.2.2), these specific biomolecules have been employed in several biosolder formulations [9, 29, 33, 17, 34]. Other reported biosolder matrices include proteins such as silk fibroin and albumin, and chitosan, a polysaccharide. A summary of previously reported biosolder formulations with details on composition is provided in Section 1.2.3.

Several biosolder form factors have been previously explored, such as liquid solution [35, 36, 29], spreadable gel [33, 17, 13], thin films [37, 13], and solid and semisolid discs [10, 9]. Non-solid formulations offer procedural versatility and fabrication scalability, whereas solid formulations provide application uniformity. To elaborate, the administration of non-solid formulations is not limited by wound topography, geometry or size, as they can be spread over and into the tissue. In contrast, thin films and solid or semisolid discs have a fixed geometry, with typically small dimensions (diameter $<$12 mm). However, their rigid form allows for easier handling and placement to the wound site. Non-solid formulations can be susceptible to uniformity issues or inconstant application, similar to medical adhesives. These tradeoffs should be considered depending on the target tissue or organ for LTW.

Photoabsorbing Agents for Biosolders

As mentioned in Section 1.1, the purpose of the photoabsorbing agent in a biosolder is to convert incoming laser light into heat. Selecting an appropriate photoabsorbing agent for a biosolder formulation first requires selecting an appropriate laser wavelength. Several constituent materials within biological tissue possess unique absorption peaks. The absorption of light by these materials reduces the amount of light that can be readily absorbed by the photoabsorbing agents within the biosolder. Fig. 1.6 shows the absorption coefficient spectra for the major absorbing tissue components [38]. Within the near-infrared (NIR) region ($\lambda \approx$ 600 nm to 1000 nm), the light is minimally absorbed by these tissue components and thus, the penetration depth of light is largest [39]. Because of this, the NIR region is also called the "therapeutic window" or "optical window" [40] as these wavelengths are well-suited for biomedical laser applications.

Indocyanine green (ICG) is an example chromophore that can achieve NIR light transduction into heat. It is a water-soluble tricarbocyanine dye with a peak spectral absorption at around 800 nm [42]. Although it has been widely used for biosolder formulations [35, 43, 36], it suffers from slow heating, limited efficiency, poor stability and chemical inflexibility [13, 29]. Since the advent of plasmonic metallic nanoparticles, which also possess a photothermal conversion property, ICG has been increasingly replaced by metallic nanoparticles for LTW biosolder formulations.

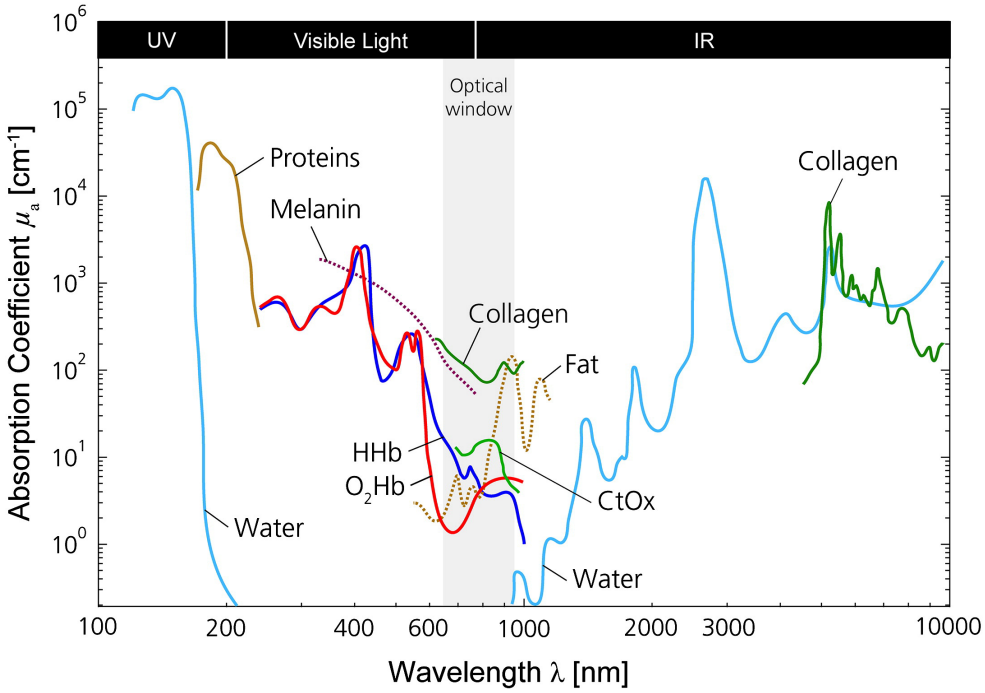


Figure 1.6: Absorbance spectra of different tissue components. The NIR region (between 600 nm and 1000 nm) is termed the optical window since light penetration is highest. HHb = deoxyhemoglobin, O_2Hb = oxyhemoglobin, CtOx = cytochrome oxidase. Obtained from Scholkmann *et al*. with permission [41].

Metallic nanoparticles exhibit strong photothermal conversion due to localized surface plasmon resonance (LSPR), in which incident photons of a characteristic wavelength induce a collective oscillation of the free electrons surrounding the nanoparticles (i.e., a plasmon is generated) [44]. Non-radiative decay of the plasmon then results in the localized generation of heat [45, 46]. Although spherical gold nanoparticles (AuNPs) are popularly used in biomedical applications, their LSPR band exists in the spectrum between $\lambda \approx 500$ nm to 600 nm, thus overlapping with the absorption band of hemoglobin species in blood [47, 48] and limiting the amount of light that can be absorbed by the spherical AuNPs. On the other hand, gold nanorods (GNRs) possess both a longitudinal and a transverse plasmon mode due to their >1 aspect ratio [49]. As the particle aspect ratio increases, the longitudinal LSPR peak shifts to longer wavelengths in the NIR region and the oscillation strength increases [49]. An illustration of the LSPR mechanism in GNRs is shown in Fig. 1.7. The position of the longitudinal plasmon band in the absorbance spectrum of

GNRs can be directly tuned by adjusting the aspect ratio (AR) of the GNRs. A larger AR results in a shift of the longitudinal band towards longer wavelengths [50].

GNRs are the preferred class of plasmonic nanoparticles for photothermal therapies since they possess the strongest LSPR peak in the NIR region. Other gold nanostructures such as nanoprisms and nanocages also possess LSPR bands within the NIR region, but their absorbance is weaker or broader compared to that of GNRs [48]. GNRs have been incorporated into numerous LTW biosolder formulations. Section 1.2.3 provides specific literature examples of these formulations.

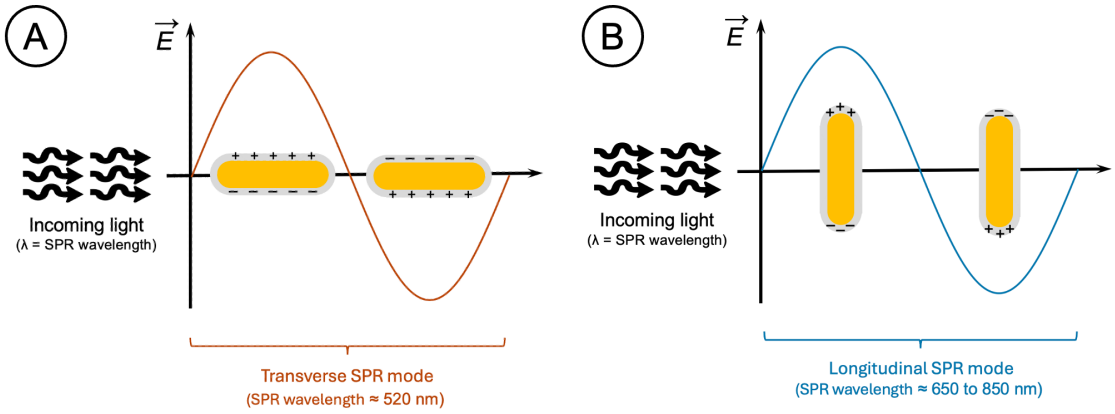


Figure 1.7: LSPR phenomenon responsible for GNR photothermal property: (a) Transverse plasmon mode, (b) Longitudinal plasmon mode.

Existing Biosolder Formulations

Table 1.1 provides a summary of a subset of previous studies that developed novel biosolder formulations for LTW. In the earlier biosolder formulations of the 1990s, ICG was the photoabsorbing agent of choice. However, beginning in the early 2000s, research has trended toward the usage of GNRs instead, for the reasons cited in Section 1.2.3. Proteins and polymers have remained the matrix material of choice owing to their useful properties and functions, as previously described in Sections 1.2.2 and 1.2.3. Although the variety of biosolder formulations presently described have demonstrated success in literature, this thesis focuses on the development of biosolders consisting of a spreadable gel matrix with embedded GNRs, also called nanocomposite gels (NCGs).

Table 1.1: Summary of prior biosolder formulations and the tissue models on which they were applied.

Authors, Year	**Biosolder Format** (Dimensions, if applicable)	**Matrix** (Optimal Concentration)	**Photoabsorber** (Optimal Concentration)	**Tissue Model**
Oz *et al.*, 1990 [43]	Solid mixture	Human fibrinogen from plasma(None given)	ICG (None given)	*In vivo* rabbit carotid artery
Schwartz *et al.*, 1998 [35]	Liquid	Human albumin (50% w/v)	ICG (0.83 mg/mL)	*In vivo* rat skin
McNally *et al.*, 1999 [36]	Liquid; Solid strips (3×1×0.15 mm)	Bovine serum albumin (25% w/v for liquid); Bovine serum albumin (60% w/v for solid strips)	ICG (0.25 mg/mL)	*Ex vivo* bovine thoracic aorta
Ratto *et al.*, 2009 [29]	Liquid	Collagen (<10% w/v)	GNR (0.1 nM)	*Ex vivo* porcine eye lens capsule
Matteini *et al.*, 2010 [33]	Spreadable gel	Hyaluronic acid from *Streptococcus equi*, MW ≈ 1000 kDa (3% w/v)	GNR (0.9 nM)	*In vivo* rabbit carotid artery
Matteini *et al.*, 2010 [37]	Thin films (⌀ ≈ 8 mm, h ≈ 40 µm)	Chitosan (<3% w/v)	GNR (<0.2 nM)	*Ex vivo* arterial tissue
Esposito *et al.*, 2012 [17]	Spreadable gel	Hyaluronic acid from *Streptococcus equi*, MW ≈ 1000 kDa (≈ 11.1% w/v)*	GNR (1.6 nM)	*In vivo* rabbit carotid artery
Huang *et al.*, 2013 [10]	Solid disc (⌀ ≈ 10 mm, h ≈ 247 µm)	Elastin-like polypeptide with 12 repeating cysteines (0.2% w/v)	GNR (≈ 614.4 nM)**	*Ex vivo* porcine intestine
Urie *et al.*, 2015 [9]	Semisolid disc (⌀ ≈ 12 mm, h <2 mm)	Collagen (0.4% w/v)	GNR (≈ 568.9 nM)**	*Ex vivo* porcine intestine
Urie *et al.*, 2018 [13]	Thin films (⌀ ≈ 10 mm, h ≈ 200 µm); Spreadable gel	Silk from *Bombyx mori*, MW ≈ 100 kDa (≈ 6.38% w/v)*	GNR (≈ 239.3 nM)**	*Ex vivo* porcine intestine (for thin film); In vivo mice skin (for spreadable gel)
Zhang *et al.*, 2024 [34]	Semisolid disc (⌀ ≈ 6.5 mm, h ≈ 1 mm)	Collagen (0.4% w/v)	GNR (1.126 nM)	*Ex vivo* porcine skeletal muscle

* These protein/polysaccharide concentrations were originally reported in wt%. Conversion calculations wt% to % w/v are provided in Section A.1 (Appendix).
** These GNR concentrations were originally reported in wt%. Conversion calculations from wt% to nM are provided in Section A.2 (Appendix).

Biocompatibility of GNR Biosolders

Despite the attractiveness of GNRs for photothermal therapies, an enduring challenge to their application in biomedical settings is the cytotoxicity of the cetyltrimethylammonium bromide (CTAB) surfactant which is used to direct anisotropic growth during synthesis and to stabilize the formed GNRs [51].

Management strategies for the cytotoxicity of CTAB include chemisorption methods, such as displacement with thiolated alkanethiols [52], and physisorption methods, such as gum encapsulation or replacement [53, 54, 55, 56]. Gum-based strategies are of particular interest due to the low cost, accessibility, biocompatibility, biodegradability, and low antigenicity of plant-derived gums [57]. Furthermore, their inherent mucoadhesive properties make them suitable for maintaining tissue contact in wound healing and drug delivery applications [57].

A previous cytotoxicity study found that gum arabic-coated GNRs applied to non-tumorigenic fibroblasts resulted in 80-90% cell viability up to a GNR concentration of 1.8 mg/L (or on the order of 10^0 pM) [54]. This suggests that gum-GNR materials, such as the formulations reported here, have the potential to possess low cytotoxicity and reasonable biocompatibility potential. Furthermore, in another study reporting on HA-coated AuNPs [58], a 90% biocompatibility was found for nanoparticle concentrations of 0.01 mg/mL (or on the order of 10^0 nM). The study further indicates that the presence of HA may prevent reactive oxygen species pathways that cause cell death.

1.2.4 LTW Tissue Joining Mechanism

The LTW joining mechanism is illustrated in Fig. 1.8. For simplicity, only collagen within the connective tissue ECM is depicted. After cleaving a network of collagen fibers, the matrix becomes permanently separated. The process of LTW involves bringing the disjointed ends into close proximity and then applying the biosolder. Under ambient conditions, the biosolder is passive and does not provide any joining capability. It is only by irradiation of NIR laser light, that the LSPR effect creates a substantial thermal response. The increase in temperature causes the collagen fibers in the connective tissue to loosen and the proteoglycan bridges to break, thereby creating separation between collagen fibrils. Once ambient temperatures are restored, new hydrogen bonds form between the collagen fibrils on the opposite wound edges, and the water in the surrounding medium [59]. The result is protein interdigitation or the re-homogenization of the tissue matrix. As mentioned in Section 1.1, this process typically unfolds at or above 60°C.

Interestingly, the heat generated during LTW causes the proteoglycan bridges between collagen fibers to dissociate well below the temperature threshold for collagen denaturation [60], inducing the dissociation of collagen fibers. At laser surgery temperatures up to 65°C, thermally induced alteration of collagen fiber alignment was observed while the individual collagen fibrils themselves remained intact [60]. This is noteworthy as it implies that as long as similar temperatures are maintained during LTW, the extent of collagen degradation can be minimized. From an immunological perspective, the degradation of collagen upon injury is known to enhance the ensuing inflammatory response [61]. Therefore, minimizing the extent of this degradation has the

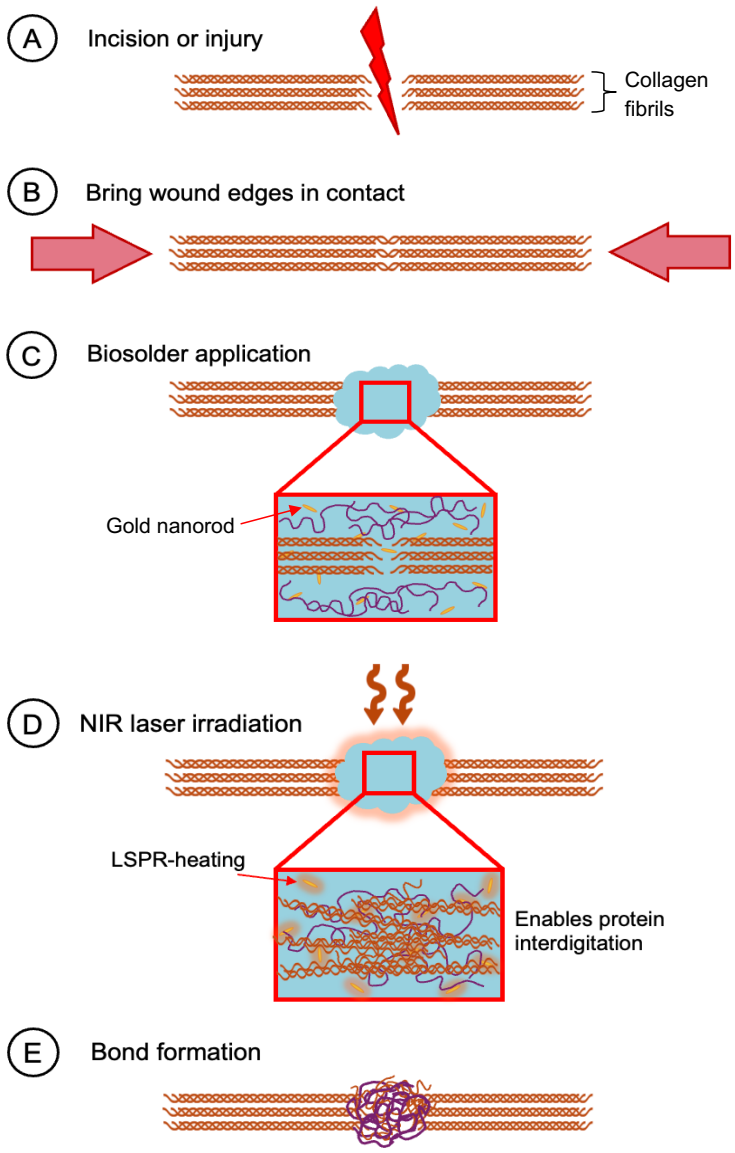


Figure 1.8: Joining mechanism of the LTW process: (a) A discontinuity in the connective tissue is created by surgical incision or injury. The LTW procedure begins with (b) wound edge apposition then (c) application of a gel biosolder containing GNRs dispersed in a polymeric or protein matrix. (d) NIR laser irradiation induces amplified and localized heating mediated by the LSPR effect, resulting in protein interdigitation, and consequently (e) the formation of a tissue bond.

potential to lessen inflammation and improve healing outcomes. However, since non-collagenous components in the tissue ECM are still damaged below 65°C, it is important to confine the laser heating as much as possible to the site of joining during LTW (e.g., with a biosolder).

1.2.5 Photothermal Conversion Efficiency (η)

A material property of interest for the development of NCG biosolders is the photothermal conversion efficiency, η. After LSPR is established, the generated plasmons can decay either radiatively (through photon re-emission) or non-radiatively (in the form of heat) [62]. Discussions of photon re-emission are beyond the scope of this project. η is defined as the ratio of laser power the NCG transduces to heat divided by the total absorbed laser power. It is effectively a measure of how well a photothermal material can convert absorbed light into heat. The incident laserRoper *et al.* were the first to report the definition and quantification of η [63] and η has since been reported for a wide range of photothermal nanomaterials in aqueous solutions [64, 65, 66, 67, 68] and gel media [69, 70].

In [63], η is determined by first stating the thermal power balance equation for a solution of colloidal gold nanoparticles fixed in place using supporting objects (e.g., glass cell) at room temperature and heated under laser irradiation starting at time, $t = 0$ s,

$$\sum_i m_i C_{p,i} \frac{\mathrm{d}T}{\mathrm{d}t} = Q_{in} + Q_0 - Q_{ext} \qquad \text{[W]} \quad (1.1)$$

where m_i represents the masses of the gel sample and supporting objects in contact with the gel sample, $C_{p,i}$ represents the specific heat capacities of the gel sample and supporting objects, T is the temperature, and t is time. The source term Q_0 represents the power dissipated by the supporting objects and gel medium without the presence of GNRs. The source term Q_{in} represents the power generated by plasmon decay of GNRs under irradiation,

$$Q_{in} = I_0(1 - 10^{-A_\lambda})\eta \quad (1.2)$$

where I_0 is the incident laser power at the longitudinal plasmonic peak wavelength λ and A_λ is the absorbance of the GNR solution at the same wavelength λ. By the Beer-Lambert Law, A_λ is dimensionless and specific for a certain wavelength, GNR concentration, and photon path length. The source term Q_{ext} represents the power dissipated to the external environment, as described by Newton's Law of Cooling,

$$Q_{ext}(t) = hA[T(t) - T_{amb}] \quad (1.3)$$

where h is the thermal transfer coefficient [W·m^2·°C^{-1}], A is the cross-sectional area through which heat transfers, and T_{amb} is the ambient temperature. Furthermore, a dimensionless driving force temperature,

$$\theta \equiv \frac{T(t) - T_{amb}}{T_{max} - T_{amb}} \tag{1.4}$$

and system time constant,

$$\tau_s \equiv \frac{\sum_i m_i C_{p,i}}{hA} \quad \text{[s]} \tag{1.5}$$

are defined in [63] to be used in what follows. Equations (1.1) and (1.3)–(1.5) can be combined and rearranged into the differential equation

$$\frac{\mathrm{d}\theta}{\mathrm{d}t} = \frac{1}{\tau_s}\left[\frac{Q_{in} + Q_0}{hA(T_{max} - T_{amb})} - \theta\right] \tag{1.6}$$

In the cooling regime, $\tau_s = \tau_{s,c}$, the laser is off, and $Q_{in} + Q_0 = 0$. Therefore, (1.6) can be solved with the initial condition $T = T_{max}$ at $t_c = 0$ s and rearranged to give

$$-\ln\theta = \frac{1}{\tau_{s,c}} t_c \tag{1.7}$$

where t_c is the time after which the laser has been turned off. Within the heating regime, $\tau_s = \tau_{s,h}$ and (1.6) can be solved with the initial condition $T = T_{amb}$ at $t_h = 0$ s,

$$\theta_{GNR} = \frac{Q_{in} + Q_0}{hA(T_{max} - T_{amb})}\left[1 - \exp\left(-\frac{-t_h}{\tau_{s,h}}\right)\right] \tag{1.8}$$

where t_h is the time after which the laser has been turned on.

Temperature curves that contain both laser heating and cooling data are then fitted to Equations (1.7) and (1.8) to obtain $\tau_{s,h}$ and $\tau_{s,c}$, respectively. From this, hA, or the thermal conductance, is calculated using the fitted τ_s value(s) and an assumed value for $\sum_i m_i C_{p,i}$ by (1.4).

When steady state is reached, $Q_0 + Q_{in} = Q_{ext}$. Substituting (1.2) and (1.3), and rearranging for η gives the photothermal conversion efficiency equation

$$\eta = \frac{hA(T_{max} - T_{amb}) - Q_0}{I_0(1 - 10^{-A_\lambda})} \tag{1.9}$$

Despite the widespread determination of η for NCG heating evaluation and optimization, there are inconsistencies across literature as to how η is calculated [71]. In Chapter 5, these inconsistencies are described in detail and addressed using a novel, yet simplified method for η determination.

1.3 Objectives

The scope of this work is to develop gel biosolder formulations and assess their thermal suitability towards effective and safe LTW. In alignment with this scope, the specific objectives of this thesis are as follows:

1. Synthesize GNRs with a longitudinal plasmon mode tuned to the NIR region
2. Develop a spreadable gel biosolder formulation which incorporates the synthesized gnr
3. Build a photothermal characterization setup that is suitable for gel analyses, is simple to use and can provide repeatable temperature measurements
4. Characterize the developed gel biosolders using the developed photothermal characterization setup
5. Devise a scheme for analyzing the clinical relevance of gel biosolders in terms of heat localization and safety, such that it can serve as a preliminary screening process of gel formulations for future administration to tissue models
6. Further apply the developed photothermal charaacterization setup to determine the photothermal conversion efficiency of developed gel biosolders

1.4 Statement of Contributions

Project conception, setup design and project directions were carried out by Prof. Michael Mayer and me. I developed the gold nanorod synthesis protocol with initial assistance from Kai Zhang and Dr. Shazia Tanvir. I developed the gel biosolder formulation containing hyaluronic acid, guar gum and gnr. Mishi Groh obtained the TEM image in Fig. 2.7. All other TEM images used for size distribution analyses were obtained by me. Rheological characterization was carried out by Dr. Charles Dal Castel and Dr. Faten Salim at the Chemical Engineering Analytical

Facilities. The method for determining thermal conductance was devised by Prof. Michael Mayer. I carried out all remaining experimental work, temperature data collection, and analyses. The laser system utilized in the photothermal characterization setup was developed by Jansen Zhou, and I integrated it with the microcontroller and RTD temperature sensor. All referenced Python scripts and CAD were created by me.

The following thesis sections contain content from a submitted manuscript, Huynh, M., Zhang, K., Tanvir, S., Mayer, M. "RTD-Based Approach for Evaluating the Thermal Aspect of Clinical Relevance of Nanocomposite Gels as Heat Localizers in Laser Tissue Welding": Section 1.1, Section 1.2.3, Section 2.2.4, Section 2.3.1, Section 2.3.2, Chapter 3, Chapter 4, Section 6.1, Section 6.2.1, and Section 6.2.2.

The following thesis sections contain content from a manuscript in preparation, Huynh, M., Mayer, M. "Robust Assessment Scheme for Photothermal Material Efficiency Using an RTD-Based Method": Section 1.2.5 and Chapter 5.

1.5 Summary

Laser tissue welding is a promising alternative technique that can potentially address the shortcomings of conventional wound closure methods. Biosolders can be administered prior to welding to assist with heat amplification and localization. Considerations for biosolder development include form factor, choice of gel matrix and photoabsorber, and biocompatibility. The definition of photothermal conversion efficiency was provided. Objectives for this thesis were also stated.

Chapter 2

Development of a Nanocomposite Gel Biosolder

This chapter provides details on the synthesis and characterization of GNRs, as well as their incorporation in a HA-guar gum matrix to produce NCG biosolders.

2.1 Summary of Seed-Mediated Growth

The seed-mediated growth method was developed by Nikoobakht and El-Sayed [50] and is the most widely used technique for preparing GNRs. The procedure involves the reduction of the salt, gold (III) chloride trihydrate ($HAuCl_4 \cdot 3H_2O$). Two solutions called the "seed solution" and "growth solution" are prepared in a cetyltrimethylammonium bromide (CTAB)-rich solution. The seed solution is prepared by the strong reduction of $HAuCl_4 \cdot 3H_2O$ (or Au^{3+}) into elemental gold "seeds" using sodium borohydride ($NaBH_4$). These seeds serve as nucleation sites to catalyze GNR growth. To successfully form the rod morphology, seed sizes 2 nm or smaller are generally required [72]. The growth solution is prepared via the weak reduction of the gold salt Au^{3+} into Au^{+}, using L-ascorbic acid (AA). Upon mixing the seed and growth solutions, the reduction of Au^{+} into elemental gold Au^{0} is catalyzed on the surface of the seeds. In the presence of silver nitrate ($AgNO_3$), CTAB preferentially binds to the $\{110\}$ and $\{100\}$ facets of the growing GNRs, which causes gold reduction to mainly occur on the ends (or $\{111\}$ facets). This leads to anisotropic growth in the longitudinal direction [73, 74, 51] and the formation of a nanorod. The precise role of the Ag^{+} ions in solution is still debated, though silver-bromide interactions may be at play, assisting with rod shaping [51].

2.2 Colloidal GNR Synthesis

This section describes a synthesis procedure modified from that described in [50] to produce colloidal GNRs in phosphate buffered saline (PBS). Reasoning for protocol deviations are provided. A post-processing procedure for size tuning and follow-up GNR characterizations are described as well. A detailed procedure for GNR synthesis is provided in the internal SOP "Protocol - GNR Synthesis - Version 3.1" included in Appendix Section F.1. For GNR stock concentration determination, the concentration curve in 2.8 should be used, as the concentration curve in the aforementioned SOP is outdated and does not include path length correction.

2.2.1 GNR Synthesis Procedure

The reagents required for GNR synthesis were gold (III) chloride trihydrate ($HAuCl_4 \cdot 3H_2O$, >99.99%), cetyltrimethylammonium bromide (CTAB, >98%), sodium borohydride ($NaBH_4$, >98.0%), silver nitrate (AgNO3, >99.0%), L-ascorbic acid (AA, 99%), and 1X phosphate buffered saline (PBS, pH 7.4, sterile). They were procured from MilliporeSigma®, Oakville, Canada.

Five stock solutions were prepared from the reagents. Table 2.1 summarizes the five stock solutions that were required for the synthesis of CTAB-capped GNRs dispersed in 1X PBS. The AA stock, $AgNO_3$ stock, and $HAuCl_4 \cdot 3H_2O$ stock were prepared by adding the necessary powder amounts to ultra-pure water and mixing them under ambient conditions. To prepare the CTAB stock, a combination of microwave heat and bath sonication were required for full dissolution of the powder in ultra-pure water. To prepare the $NaBH_4$ stock, the powder was added to ice-cold ultra-pure water in a chilled glass vial.

Table 2.1: Composition overview of reagent stock solutions and how often they are prepared.

Stock Solution	**Concentration** (M)	**Powder Required** (g)	**Ultra-pure Water Volume** (mL)	**Frequency of Preparation/ Shelf Life**
AA	0.0788	0.0139	1.00	Must be prepared fresh
$AgNO_3$	0.0040	0.0102	15.0	Can use the same batch for up to **10 months**
$HAuCl_4 \cdot 3H_2O$	0.0127	0.0200	4.00	Can use the same batch for up to **10 months**
CTAB	0.2000	1.4578	20.0	Must be prepared fresh
$NaBH_4$	0.0300	0.0045	4.00	Must be prepared fresh

Fig. 2.1 shows an overview of the GNR synthesis procedure. A modified protocol, adapted from Nikoobakht's method [50], was carried out. Further descriptions and justifications for protocol deviations are provided in Section 2.2.2.

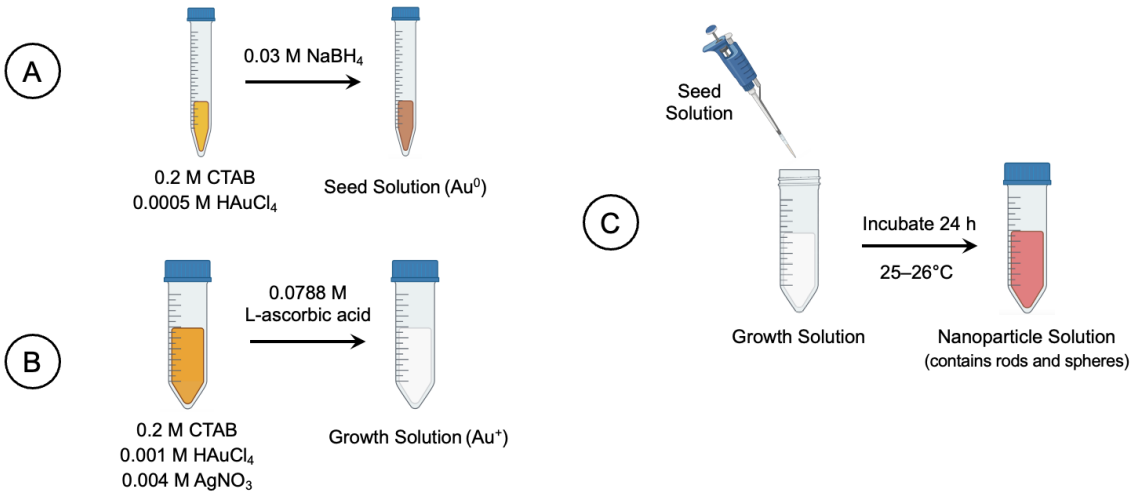


Figure 2.1: Overview of modified seed-mediated growth method for the generation of GNRs, adapted from Nikoobakht and El-Sayed's method [50]. (a) Preparation of seed solution, (b) Preparation of growth solution, (c) Addition of seed solution to growth solution and incubation. Graphics produced with BioRender.

The required stock solution volumes that were used to prepare 5 mL of seed solution and 30 mL of growth solution are provided in Table 2.2. The seed solution was prepared by first gently mixing the CTAB stock, ultra-pure water, and $HAuCl_4 \cdot 3H_2O$ stock until the solution turned a golden orange colour. Following this, the ice-cold $NaBH_4$ stock was added, and the solution was vortex-mixed for 2 min. Successful seed solutions had a characteristic reddish-brown colour. The growth solution was prepared by first gently mixing the CTAB stock, ultra-pure water, $HAuCl_4 \cdot 3H_2O$ stock, and $AgNO_3$ stock until the solution turned a golden orange colour. Following this, AA stock was added and gently mixed until the solution turned colourless and transparent. Finally, 35 µL of seed solution was added to the growth solution. The combined seed and growth solution was incubated in a sealed vial at 25°C–26°C for 24 h. The resulting solution is a crude mixture containing GNRs and larger spherical gold nanoparticles. Further purification and GNR size selection was carried out, as described in Section 2.2.3.

Table 2.2: Required stock solution volumes to prepare 5 mL seed solution and 30 mL total GNR growth solution.

Solution	Ultra-pure Water (mL)	0.0127 M $HAuCl_4 \cdot 3H_2O$ (mL)	0.0040 M $AgNO_3$ (mL)	0.2000 M CTAB (mL)	0.0788 M AA (mL)	0.0300 M $NaBH_4$ (mL)	Seed Solution (mL)
Seed (5 mL)	2.266	0.0929	-	2.358	-	0.283	-
Growth (30 mL)	13.440	1.149	0.584	14.589	0.209	-	0.035

2.2.2 Synthesis Procedure Deviations and Justifications

The following modifications were applied to the GNR synthesis method originally reported by Nikoobakht and El-Sayed in order to repeatably obtain the desired GNR population (AR ≈ 4):

1. The concentration of $NaBH_4$ stock was increased to 0.030 M, from the original 0.010 M.
2. Additional AA was added to the growth solution prior to adding the seed solution.
3. Incubation was carried out at 25°C–26°C for 24 hours, instead of at 27°C–30°C due to equipment limitations.

To successfully and repeatably generate Au seeds, it was necessary to triple the $NaBH_4$ concentration. The originally reported concentration of 0.010 M $NaBH_4$ resulted in a colourless solution (Fig. 2.2a), indicating only the partial reduction of Au^{3+} to Au^{+}. Using a higher $NaBH_4$ concentration of 0.030 M resulted in a reddish-brown solution (Fig. 2.2b), which is characteristic of elemental Au seeds. To further confirm the presence of Au seeds, UV-vis spectroscopy was performed (Fig. 2.3). The broad absorption band in the UV region is characteristic of gold nanoparticles with <2 nm diameter [75], therefore confirming the presence of Au seeds suitable for GNR generation. Fig. 2.2c shows a GNR solution successfully prepared using a seed solution containing the tripled $NaBH_4$ concentration (0.030 M).

The second procedure deviation was the addition of excess AA to the growth solution prior to injecting the seed solution. As described in Section 2.1, AA is a weak reducing agent that only partially reduces Au^{3+} to Au^{+}. The chemical equilibrium between the Au oxidation states is described by

$$Au^{3+} + 2\,Au^{0} \rightleftharpoons 3\,Au^{+} \tag{2.1}$$

The forward reaction, referred to as comproportionation involves the combining of two oxidation states to form another. The reverse reaction is referred to as disproportionation [76]. In (2.1),

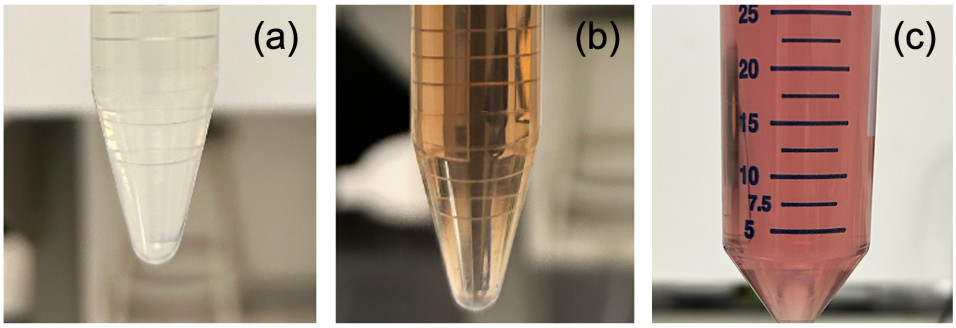


Figure 2.2: Comparison of seed solutions prepared with (a) 0.01 M $NaBH_4$ per the original protocol [50] and (b) 0.03 M $NaBH_4$. (c) The resulting GNR solution using the seed solution in (b).

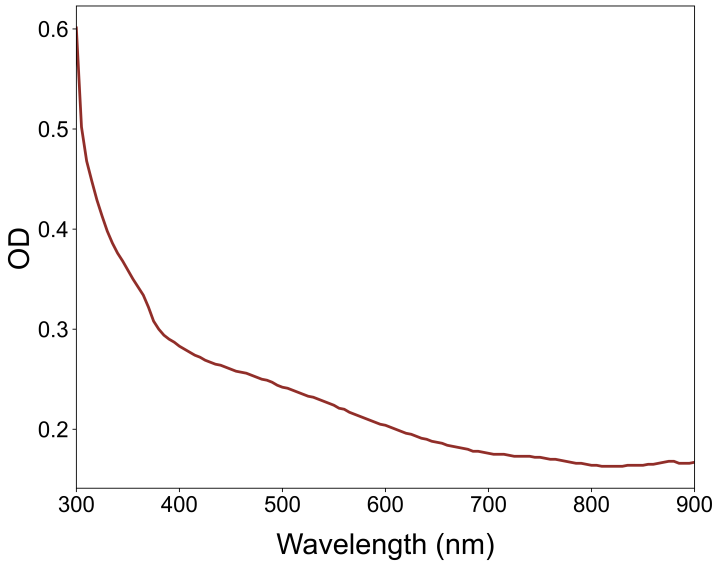


Figure 2.3: Absorbance spectrum for seed solution prepared with 0.03 M $NaBH_4$ (obtained with the Biotek Epoch microplate reader, path length $\approx$ 5.26 mm). Optical density (OD) is synonymous with absorbance.

comproportionation is more favourable due to the stability of the Au^{+} species. It is therefore necessary that the growth solution contains a saturation of Au^{+} in order to prevent the comproportionation, or loss, of Au^{0} seeds when they are injected into the growth solution [51]. The presence of Au^{+} is visually confirmed when the growth solution turns colourless. However, it was occasionally observed that the originally reported AA volume did not yield a fully colourless growth solution. This ultimately led to no GNR generation due to the premature destruction of Au seeds. This work's introduction of excess AA (i.e., an additional 5 µL AA per 30 mL of total solution) prior to seed solution addition produced a fully clear growth solution and, as a result, the repeatable generation of GNRs.

2.2.3 Post-Processing Procedure

The purpose of post-processing is to (1) Remove the spherical nanoparticle population, and (2) Isolate the GNR population with an average AR of approximately 4. The product of the synthesis procedure described in Section 2.2.1 is a heterogeneous solution of AuNPs with various morphologies. To separate AuNP populations, centrifugation is commonly used. The procedures used for GNR purification and size selection are summarized in Fig. 2.4.

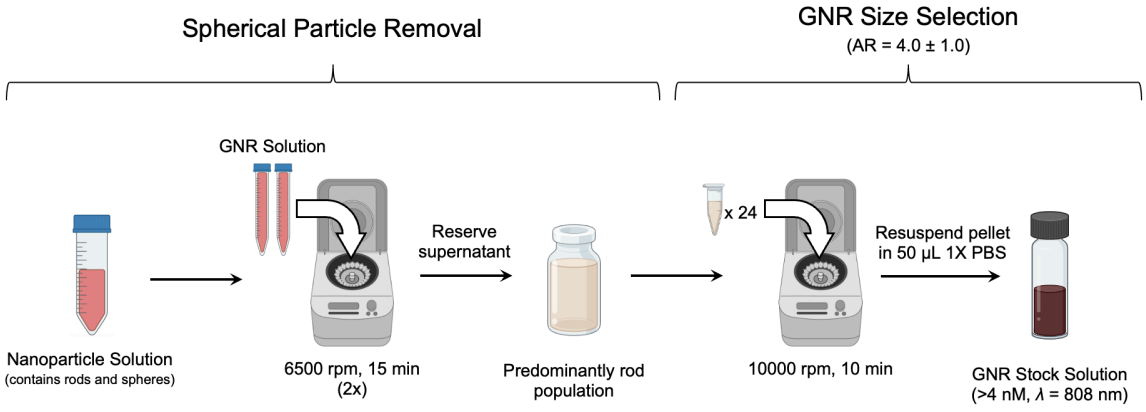


Figure 2.4: GNR purification and size selection procedures. Graphics produced with BioRender.

The 30 mL nanoparticle solution obtained via the synthesis procedure was evenly divided into two 15 mL conical vials. These were centrifuged at 6500 rpm for 15 min. The pellet, which contained predominantly spherical nanoparticles, was discarded. The supernatant (remaining liquid following centrifugation) contained predominantly GNRs and was reserved and divided evenly among two new 15 mL conical vials. These were then subjected to a second cycle of

centrifugation at 6500 rpm for 15 min for further removal of spherical particles. Fig. 2.5a shows the absorbance spectra for the as-synthesized AuNP solution prior to any centrifugation, the pellet and supernatant following Cycle 1 of centrifugation, and the supernatant following Cycle 2 of centrifugation. The spectrum for the Cycle 1 pellet is characteristic of spherical AuNPs [48]. The dual plasmon bands that are characteristic of GNRs are most present in the supernatant following Cycle 1 and Cycle 2 of centrifugation. Cycle 2 possesses a lower magnitude transverse peak relative to the longitudinal peak, indicating higher yield [77].

Following this, the Cycle 2 supernatant was divided into 1 mL aliquots and centrifuged at 10000 rpm for 10 min. At similar centrifuge speeds, the extracted pellet contains a GNR population with a longitudinal LSPR peak at roughly 800 nm [78], or a rod AR of roughly 4 [50]. As confirmed in Fig. 2.5b, the third round of centrifugation resulted in a shift of the longitudinal band to be centred around 800 nm (blue dashdot data corresponds to 10000 rpm). The pellets were redispersed in 50 µL of 1X PBS, combined and stored in a sealed vial under ambient conditions. This GNR stock solution was stable under these conditions for up to 5 months.

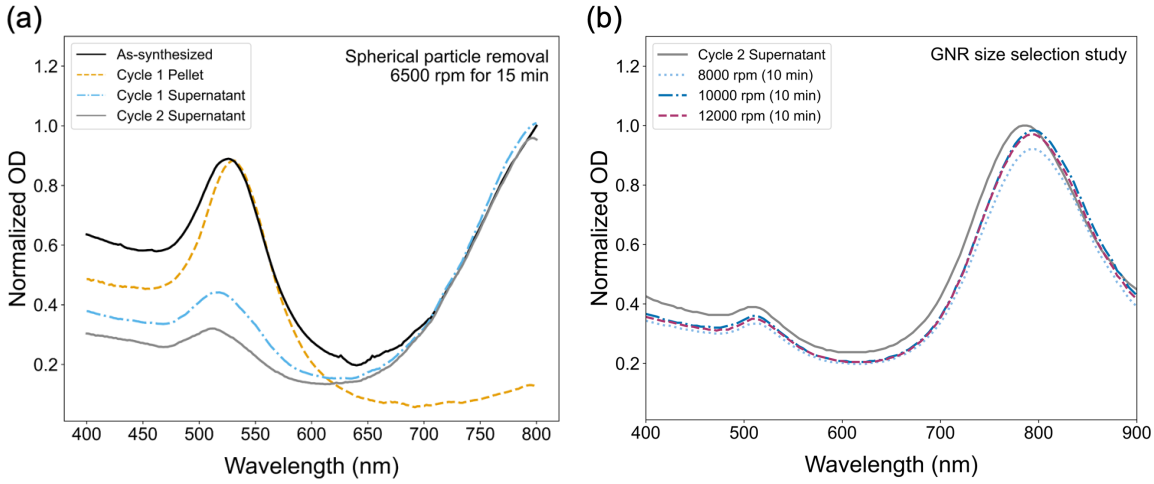


Figure 2.5: Absorbance spectra of GNR solutions following (a) the first and second rounds of centrifugation at 6500 rpm for 15 min (obtained with the HP 8452A Diode Array spectrophotometer), (b) the third round of centrifugation at various speeds (obtained with the Biotek Epoch microplate spectrophotometer).

Other centrifugation speeds (8000 rpm, 12000 rpm) were tested, as shown in Fig. 2.5b. The longitudinal peaks for GNRs centrifuged at 8000 rpm, 10000 rpm, and 12000 rpm were all positioned at $\lambda \approx 796$ nm. Therefore, these centrifugation speeds provide similar size isolation. However, the yield was highest at 10000 rpm. As such, 10000 rpm was selected as the speed for

the third centrifugation cycle. Only one round of size selection at 10000 rpm was performed as any further centrifugation of the GNR solution was found to result in aggregation, rendering the solution unusable. This is due to the removal of CTAB in the discarded supernatant. Successive centrifugation cycles continually deplete the CTAB concentration, therefore destabilizing the GNR dispersion.

2.2.4 GNR Characterization

The final GNR stock solution is shown in Fig. 2.6. Transmission electron microscopy (TEM) was performed on aqueous GNRs using the Hitachi HT7830 TEM at 30000× magnification and an accelerating voltage of 80 kV (Fig. 2.7a). The darkened ends of the GNRs in the TEM micrograph can potentially be attributed to diffraction contrast [79]. Diffraction can occur when the particle is appropriately oriented relative to the incident electron beam such that the Bragg condition is satisfied [79, 80]. The crystallographic arrangement of Au atoms at the GNR ends is distinct from that of the GNR sides [81]. Thus, it is expected that diffraction contrast can present differently at the GNR ends compared to the remaining body of the GNR.

The size distribution of aqueous GNR AR was determined using ImageJ analysis (where AR = rod length / rod diameter) on micrographs captured with the Philips CM10 TEM (Fig. 2.7b). The ImageJ analysis procedure is described in Appendix Section B. The average AR ± standard deviation was approximately 4.0 ± 1.0 (n = 144), which is commensurate with the measured plasmon band position at ≈800 nm, as previously related [50].



Figure 2.6: Photograph of ready-to-use GNR stock solution (≈4nM–5 nM) in 1X PBS.

To determine the concentration of purified and size-selected GNRs, a standard curve was generated and used. UV-vis-NIR absorbance spectra was obtained for commercial GNRs of a similar AR = 4.0 and a known concentration of 1.126 nM (Nanopartz, Colorado, USA). The

commercial GNR stock was serially diluted 2-fold and measured with UV-vis spectrophotometry to obtain the absorbance values of the commercial GNR dilutions at λ = 808 nm. These absorbance values were then used to generate a linear calibration curve according to the Beer-Lambert Law (Fig. 2.8). The regression equation shown in Fig. 2.8 was used to extrapolate the concentration of GNR stock solutions synthesized in-house. Two GNR stock solutions with different concentrations were used for this thesis. For data reported in Chapters 4 and 5, the GNR stock concentrations were determined to be 4.40 $\pm$ 0.09 nM and 5.97 $\pm$ 0.12 nM, respectively. The method for calculating the uncertainty in these stock concentration is presented in Appendix Section A.3.

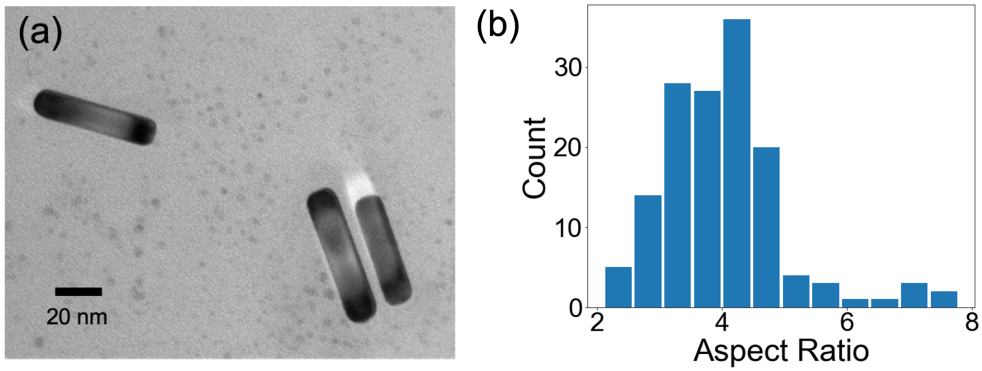


Figure 2.7: Size characterization of prepared GNRs in 1X PBS. (a) TEM micrograph, obtained by Mishi Groh, (b) GNR size distribution by aspect ratio based on collected TEM micrographs (n = 144).

2.3 Gel Biosolder Development

This section describes the composition, preparation and cost breakdown for developed HA-guar gum (GG) GNR gels. A detailed procedure for its preparation is provided in the internal SOP "Protocol - Hyaluronic Acid Guar Gum GNR Gel Preparation - Version 1.0" included in Appendix Section F.2.

2.3.1 Composition and Preparation

Large-molecular weight (MW) hyaluronic acid (HA) was selected as the matrix material owing to its biocompatibility and prior success in LTW literature [33], as well as its usefulness for wound

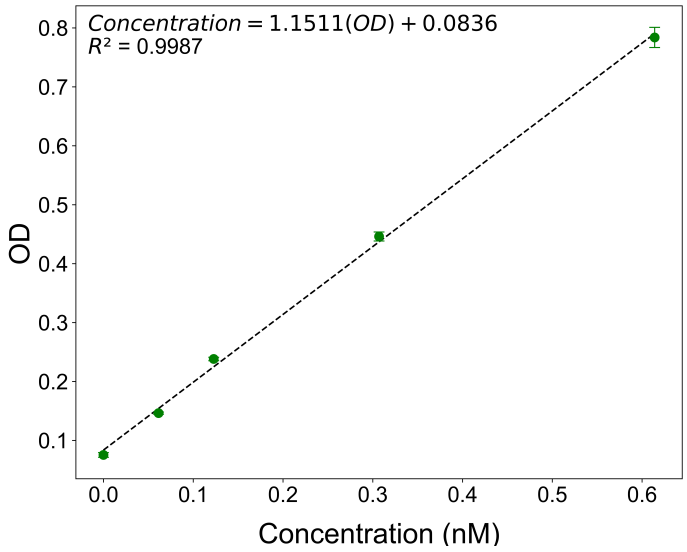


Figure 2.8: Standard curve of commercial GNRs (AR = 4.0, Nanopartz) for λ = 808 nm (n = 3). The OD values were obtained using the Biotek Epoch microplate reader.

healing as discussed in Section 1.2.2. Colloidal CTAB-capped GNRs (shown in Fig. 2.6) were incorporated as the photoabsorbing components responsible for amplified heat generation. GG (Fig. 2.9; MW range between 50,000 and 8,000,000 Da [82]) was added as a thickening agent to adjust viscosity, as well as to improve the stability, and therefore photothermal conversion, of the dispersed GNRs (as will be discussed in Section 4.1.2).

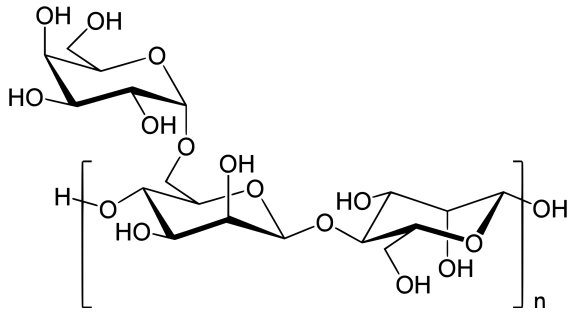


Figure 2.9: Chemical structure of guar gum. Obtained from Wikipedia (public domain image).

Nine formulations of biosolder were prepared (Fig. 2.10) with varying concentrations of GG (0.00, 0.10, 0.25% w/v) and GNRs (0.0, 0.7, 1.4 nM) in 1X PBS. HA sodium salt (from *Strep-*

tococcus equi, MW ≈ 1500–1800 kDa), 1X PBS (pH 7.4, liquid), and GG were procured from MilliporeSigma®, Oakville, Canada. Gel preparation involved three simple steps, as visualized

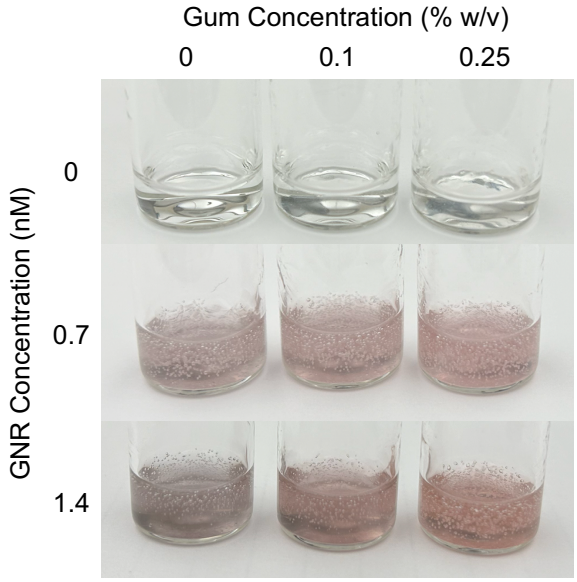


Figure 2.10: Photographs of all nine gel formulations with varied GG and GNR concentrations

in Fig. 2.11: (1) Pre-mixing of liquid materials (GG stock solution, GNR stock solution, and 1X PBS to a final volume of 1 mL), (2) Addition of pre-mixed liquid materials to solid HA pellets, and (3) Sonication and manual mixing until homogeneity is achieved. Further descriptions of these steps is provided in what follows.

Solid HA pellets were added to a glass vial. In a separate vial, a GG stock solution of 0.4% w/v was prepared by dissolving and vortex-mixing 40 mg of solid GG powder in 10 mL of 1X phosphate buffered saline (PBS). In a new microcentrifuge vial, the GG stock solution (0.4% w/v), GNR stock solution (4.40 nM or 5.97 nM), and 1X PBS were added for a total volume of 1 mL with the desired GG and GNR concentration provided in Table 2.3. This is referred to as the ”pre-mixing” step. Note that the volumes listed in Table 2.3 pertain to the usage of the 4.40 nM GNR stock solution. The liquid contents of the microcentrifuge vial were then vortex-mixed for 10 s, or until fully combined, and then transferred to the vial of HA pellets. The solution was vigorously mixed with a micro-stainless-steel scoopula until visible gelation occurred. The gel vial was then bath-sonicated for 10–15 min and then mixed manually with a micro-stainless-steel scoopula. This cycle of sonication and manual mixing was repeated until the gel was visually homogeneous—typically after a total of 40–60 min. Gel samples were left in a sealed vial at

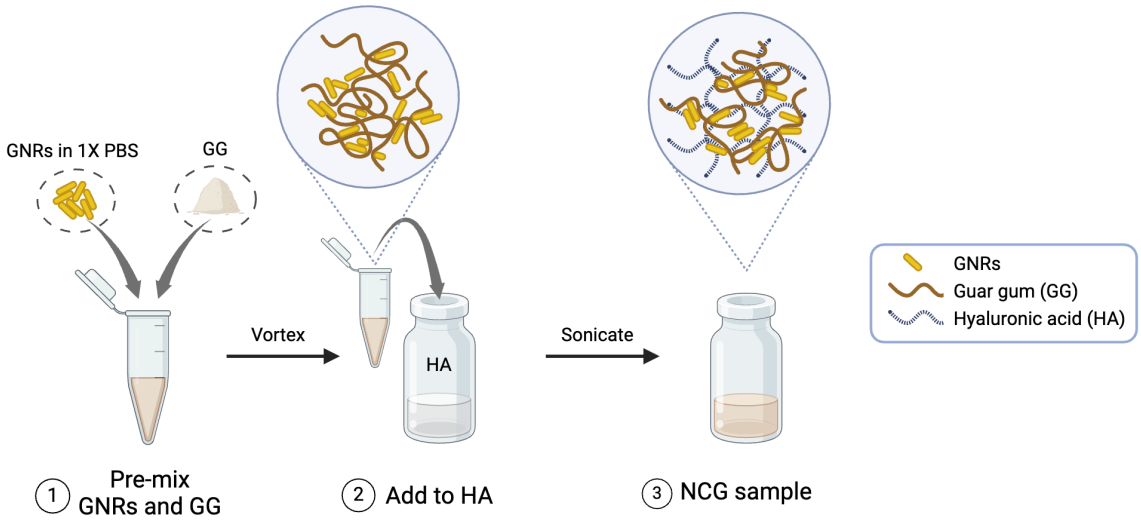


Figure 2.11: Overview of biosolder gel preparation with constituent material interactions highlighted. The final gel is comprised of an interpenetrating network of GG and HA chains. Graphics produced with BioRender.

ambient temperature overnight to allow further GNR diffusion and bubble removal. The step of pre-mixing GG with the GNRs is crucial, as it was found to aid in the stabilization of the GNRs in the gel matrix. Fig. 2.12 shows that the omission of this pre-mixing step results in GNR aggregation.

For the two GNR stock solutions used (4.40 nM and 5.97 nM), the corresponding GNR dilution concentrations used for gel preparation were (0.7 ± 0.01 nM, 1.4 ± 0.03 nM) and (0.7 ± 0.02 nM, 1.4 ± 0.04 nM), respectively. The uncertainties in the GNR dilution concentrations were calculated by standard uncertainty propagation methods, as described in Appendix Section A.3. Optical micrographs of control and GNR-containing gels are shown in Fig. 2.13. A decrease in gel transparency is evident for the sample containing GNRs, due to the hue of aqueous GNRs. As illustrated in Fig. 2.11, the final gel containing HA, GG and GNRs is comprised of an interpenetrating network of GG and HA polymer chains with GNRs dispersed throughout. Gels were stored at room temperature in a sealed vial and tested within 1-3 days of preparation.

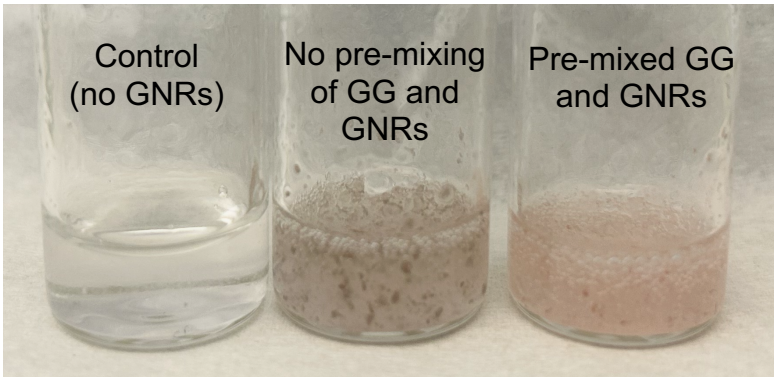


Figure 2.12: The importance of pre-mixing GG and GNRs prior to addition to HA. There is visibly more aggregation (i.e., a greyish purple hue) in the gel where pre-mixing was omitted. The pre-mixed gel retained the pale pink colour of the GNR solution indicating dispersion stability. Middle and right gels contain 0.4 nM GNRs, 0.25% w/v GG.

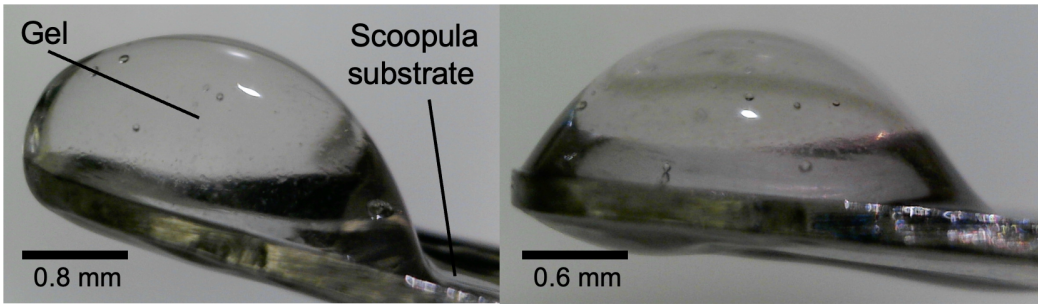


Figure 2.13: Optical microscopy of gel specimens on stainless steel substrate without GNRs (left) and with 1.4 nM GNRs (right).

Table 2.3: Composition overview of all nine biosolder formulations with varying GG and GNR concentrations. The provided amounts produce 1 mL of each formulation and are based on a GNR stock concentration of 4.40 nM.

GNR Concentration (nM)	**GG Amount** (% w/v)	**HA to add,** m_{HA} (mg)	**GG stock to add,** $V_{stock,GG}$ (µL)	**GNR stock to add,** $V_{stock,GNR}$ (µL)*	**1X PBS to add,** V_{PBS} (µL)*
0.0	0.00	30.0	0	0	1000
	0.10	29.0	250	0	750
	0.25	27.5	625	0	375
0.7	0.00	30.0	0	159	841
	0.10	29.0	250	159	591
	0.25	27.5	625	159	216
1.4	0.00	30.0	0	318	682
	0.10	29.0	250	318	432
	0.25	27.5	625	318	57

* The volumes in these columns are subject to change when different GNR stock solution concentrations are used. The pertinent calculations are described in detail in the Gel Preparation SOP, provided in Appendix Section F.2.

2.3.2 Rheological Characterization

Rheological testing was performed using the TA Instruments Discovery HR 20 rheometer with a 25 mm parallel plate geometry, with the methods described by [83]. To determine the viscoelastic behaviour and dynamic viscosity of control gels (0 nM GNRs) and NCGs (1.4 nM GNRs) containing 0.25% w/v GG. Pertinent viscoelastic parameters are determined via oscillatory shear tests. The oscillatory or sinusoidal stresses applied induce a lag or phase shift between the stress and resulting strain [84]. This behaviour can thus be defined using complex variables in what follows [84]. The complex modulus G^* is defined as

$$G^* = G' + iG'' \tag{2.2}$$

where G' is the storage modulus (an indicator of elastic behaviour), G'' is the loss modulus (an indicator of viscous behaviour), and i is the imaginary number $\sqrt{-1}$. The loss factor is defined as

$$\tan(\delta) = \frac{G''}{G'} \tag{2.3}$$

For $\tan(\delta) \ll 1$, a material is considered more solid-like, whereas for $\tan(\delta) \gg 1$, a material is considered more liquid-like [84]. The complex viscosity and its magnitude are respectively defined as

$$\eta^* = \frac{G^*}{\omega} \tag{2.4}$$

and

$$|\eta^*| = \frac{|G^*|}{\omega} = \frac{\sqrt{(G')^2 + (G'')^2}}{\omega} \tag{2.5}$$

where ω is the angular frequency (rad/s).

First, an amplitude sweep was performed to determine the maximum allowable strain such that the material remains within its linear viscoelastic region [85]. All rheological characterization must be performed within this region to ensure that measured viscoelastic parameters are strain-independent [85]. Fig. 2.14a shows the storage and loss moduli over angular frequency for the control gels and NCGs, Fig. 2.14b shows the complex viscosity and loss factor over angular frequency, and Fig. 2.14c shows the dynamic viscosity over shear rate.

The 1.4 nM GNR gel exhibited predominantly elastic behaviour ($G' > G''$ in Fig. 2.14a) for the frequency range of 0.4 to 100 rad/s, respectively. This, coupled with a decreasing loss factor with increasing angular frequency (Fig. 2.14b), indicates overall stability of the GNR-containing gel matrix [86]. This retention of elastic behaviour can be advantageous for LTW as it ensures there is minimal liquid-like outflow of the gel material after it has been spread across a tissue surface. In Fig. 2.14c, the dynamic viscosity of control gels (0 nM GNRs, 0.25% w/v GG) was found to decrease from 35398 mPa·s to 4619 mPa·s over a shear rate range of 10 to 100 s^{-1}, respectively. For NCG samples (1.4 nM GNRs, 0.25% w/v GG), the viscosity decreased from 84537 mPa·s to 3258.9 mPa·s over a shear rate range of 10 to 100 s^{-1}, respectively. The decrease in NCG viscosity with increasing shear rate (i.e., shear-thinning behaviour) highlights the "workability" of the gel for clinical application. That is, they can be easily spread over a tissue surface with a scoopula tool. These findings align with a previous study which reported on the rheological properties of hydrogels embedded with either gold nanorods or gold nanospheres [86]. They reported that the addition of GNRs with various surface modifications, at concentrations from 1.0 to 6.0 nM, increased the low-shear rate viscosities when compared to control [86]. This effect was also observed in Fig. 2.14c for the developed HA-GG gels reported here.

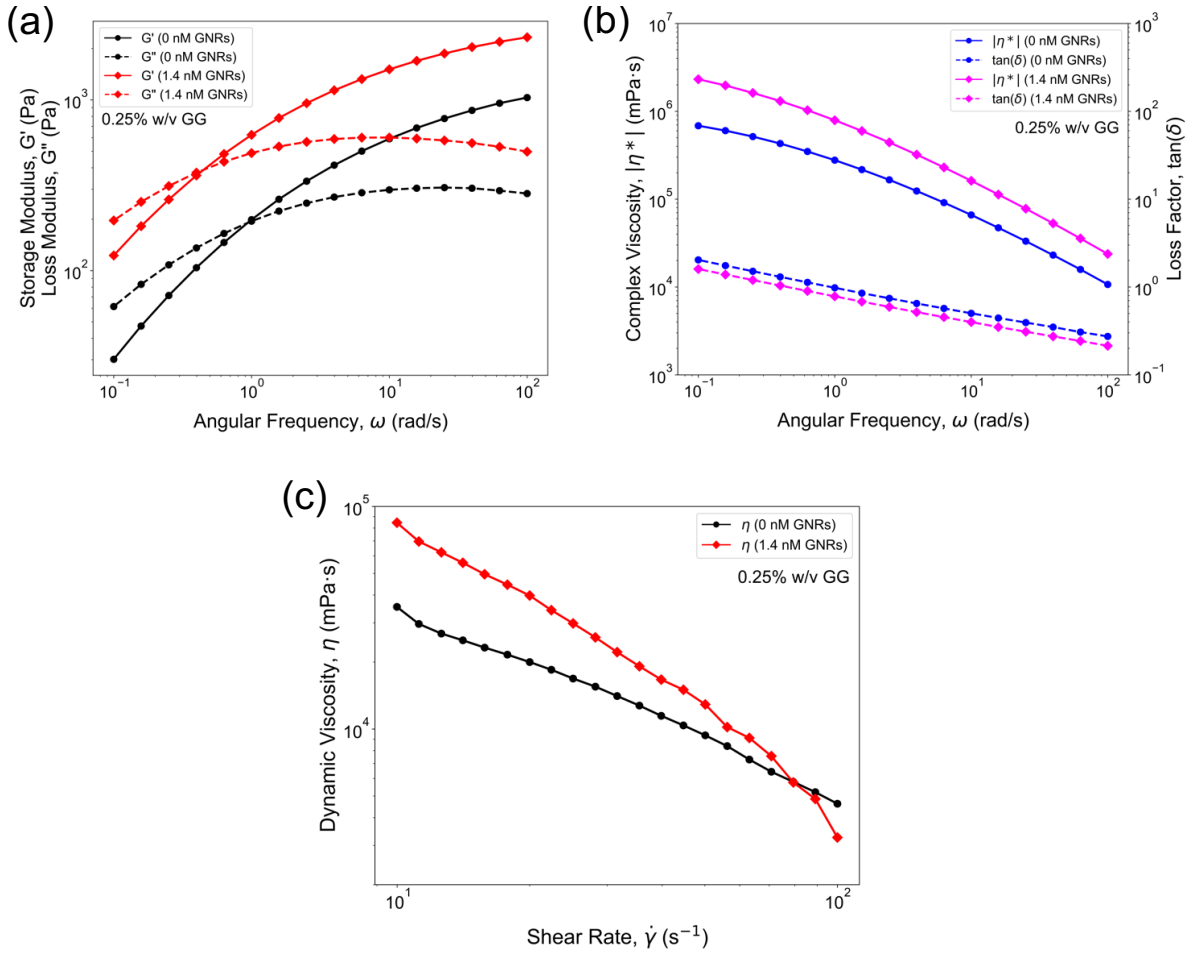


Figure 2.14: Rheological characterization of control gel (0 nM GNRs) and NCG (1.4 nM GNRs) containing 0.25% w/v GG. (a) Storage modulus (G') and loss modulus (G''), measured at a constant shear strain of 1%. (b) Complex viscosity ($|\eta^*|$) and loss factor ($\tan(\delta)$), measured at a constant shear strain of 1%. (c) Dynamic viscosity over shear rate. All rheology curves were obtained by Dr. Charles Dal Castel and Dr. Faten Salim at the UW Department of Chemical Engineering's Analytical Facilities.

2.3.3 Cost Breakdown for Developed Biosolder

Table 2.3.3 shows an example cost breakdown for 1 mL of a gel biosolder. As an example case, the cost of biosolder can be compared to that of sutures for a 5 cm incision in tissue. From experience, 0.5 mL of biosolder is sufficient to coat a 5 cm incision. The cost for 0.5 mL of

biosolder is $1.80. For suturing, the general rule is to achieve a suture length-to-wound length ratio (SL:WL) of ≥ 4, especially for abdominal closures to reduce the risk of incisional hernias [87]. The price of e.g., 4-0 Ethilon sutures is approximately $0.14/cm. Therefore, for a 5 cm incision (20 cm of suture), the cost of suture material is $2.79. This is a strictly materials cost comparison. Additional suture kit and labour costs are incurred [88]. As well, for LTW, there is the added cost of the laser system. The custom laser system used for the presented work (described in Chapter 3) had an estimated cost of ≈$996 (see Section 3.5 for breakdown).

Table 2.4: Cost breakdown for 1 mL of gel biosolder (1.4 nM GNRs, 0.25% w/v GG).

Component	**Cost/mL of gel** ($)
AA	0.003
$AgNO_3$	<0.001
$HAuCl_4 \cdot 3H_2O$	0.276
CTAB	0.257
$NaBH_4$	<0.001
HA	2.998
GG	0.001
1X PBS	0.069
Total	3.60

2.4 Summary

Gold nanorods were synthesized and tuned using a repeatable method adapted from literature. The GNRs possessed an aspect ratio of approximately 4.0 and a longitudinal plasmon mode at $\lambda \approx 800$ nm, thus enabling their utility for heat localization in NIR-based LTW procedures. The GNRs were then incorporated into gels containing various concentrations of hyaluronic acid and guar gum to produce nanocomposite biosolders. The viscosity of the biosolders were tuned such that they remained stable and workable, and could be easily spread over metal, glass and tissue surfaces using a scoopula tool.

Chapter 3

RTD-Based Photothermal Characterization Scheme

This chapter discusses of a resistive temperature detector (RTD)-based method employing a custom laser-temperature sensor apparatus. The developed system addresses the shortcomings of existing methods for the photothermal characterization of NCGs. The development of the custom apparatus is also described. The content of this chapter overlaps with that of my co-authored manuscript submission named in Section 1.4.

3.1 Motivation and Current Methods

Successful LTW with NCGs can be predicted if they exhibit sufficient heat amplification and localization shown using a thorough characterization scheme. To assess the readiness of an NCG formulation for future administration to tissue models, it is important and resource-effective to first characterize their heating behaviour in isolation. Several schemes exist for measuring the temperature of irradiated gold nanoparticles in aqueous solution [89, 63, 90, 91]. However, these methods can be costly, highly involved, or possess little suitability for gel analyses.

For the temperature measurement of laser-irradiated gels, the most popular sensors employed are infrared cameras, fiber Bragg grating (FBG)-based sensors and thermocouples. The monitoring of NCGs in isolation via infrared (IR) thermometry has been previously reported as secondary analyses within larger LTW studies [9, 13]. However, IR cameras come with an inherent level of uncertainty due to emissivity effects and require calibration with e.g., a blackbody source. Moreover, quantifying the heating localization is not usually reported.

FBG-based methods reported for the photothermal characterization of NCGs and tissue-mimicking gel models provide the advantages of multiplexing and accuracy [92, 93]. However, FBG sensors require complex fabrication if custom-made. Furthermore, commercial models like that used in [94] with its highly involved procedures can be more complicated to use than an RTD.

Thermocouple-based approaches reported the submersion of a thermocouple into a quartz cuvette containing the gel sample [70, 95, 69]. Due to the standardized size of the cuvette, this setup possesses an inherent laser path length of 1 cm, which is unrepresentative of the typically micron-scale layer of NCG that would be administered during the LTW procedure.

To address these shortcomings, an RTD-based photothermal characterization method for NCGs is proposed. It aims to be faster, simpler, more repeatable, more economical, and overall, more suitable for gel samples. The thin film RTDs used are more economical than FBG sensors and are unsusceptible to the emissivity effects inherent to IR thermometry. Furthermore, they have lower mass and volume than wire-based RTDs and therefore possess a comparatively fast response rate. A photothermal characterization scheme is proposed whereby the heating performance of biosolder formulations can be reliably assessed in isolation prior to administration to tissue models.

3.2 Laser-Temperature Sensor System Design

The Pt100 RTD sensor (Fig. 3.1 left) was used for the photothermal characterization setup owing to its high-temperature stability and repeatability. Its sensing area consists of a resistive Pt serpentine (Fig. 3.1 right). Pt100 RTDs exhibit a near-linear relationship between temperature and resistance, as described by the polynomial

$$R_{RTD}(T) = R_0(1 + AT + BT^2) \qquad [\Omega] \quad (3.1)$$

where $R_0 = 100\ \Omega$, $A = 3.9083 \times 10^{-3}\ ^\circ\mathrm{C}^{-1}$ and $B = -5.775 \times 10^{-7}\ ^\circ\mathrm{C}^{-2}$ [96]. A detailed schematic of the laser-temperature sensor system connectivity is shown in Fig. 3.2. A Raspberry Pi 2 Model B (RPi 2B) served as the microcontroller. The RPi operating system, a derivative of Debian Unix, was loaded onto the RPi via a 32 GB micro-SD card. The RPi 2B was configured to have Wi-Fi connectivity using the TP-Link AC600 Nano Size Wi-Fi dongle, enabling remote control of the system from any other desktop, laptop or mobile device, and seamless data file transfer via Teamviewer. The Pt100 RTD was interfaced with the RPi through the MAX31865 RTD Temperature Sensor Amplifier (Adafruit, New York, USA) using the four-wire configuration. This configuration was employed to eliminate the effect of wire or connector resistances

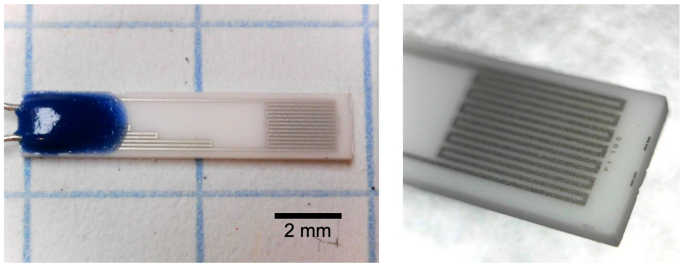


Figure 3.1: Photographs of commercial thin film Pt100 RTD. From submitted manuscript.

and thus improve accuracy. The amplifier board outputs a small measuring current ($\leq$5.75 mA) across one pair of Pt100 wires and measures the voltage drop across the other pair in order to determine the RTD resistance. Using the available Adafruit MAX31865 Python library, this resistance value was converted to temperature by solving the established polynomial relationship in (3.1). Temperature sampling was carried out at 0.14 s intervals. The custom laser system can be programmed to output optical power between 0.25 W and 3.78 W. It employs a fiber-coupled 808 nm 5 W diode laser (Box Optronics, China) under continuous wave (CW) operation. The diode laser is driven by a high-power laser driver (Lasertack, Germany) with integrated temperature monitoring and cooling by a negative temperature coefficient (NTC) thermistor and a thermoelectric cooler (TEC), respectively.

To vary the laser diode output power, a modulation voltage can be applied to the laser driver across the MOD+ and MOD- terminals (see Fig. 3.2). This was done using the pulse width modulation (PWM) functionality off the RPi 2B microcontroller. Briefly, PWM is a technique for varying output voltage in digital circuits or for emulating analog outputs via digital outputs. In digital circuits, only two states exist: ON or OFF (e.g., 5 V output or 0 V output from the RPi 2B). To achieve intermediate output voltages, one can vary the ratio of time ON versus time OFF for successive square pulses such that the average perceived output is lower than 5 V (see Fig. 3.3a for operating principle). The percentage of time ON within a cycle is referred to as the duty cycle. A general-purpose input/output (GPIO) pin on the RPi 2B was connected to the MOD+ terminal on the laser driver and configured for PWM output using a Python script (Listing D.2, Appendix). The `duty_cycle` variable in the PWM script can be modified to set a constant output voltage, and therefore, constant laser power. To determine the appropriate duty cycling for a given laser power, a calibration curve (Fig. 3.3b) was generated with power measurements obtained via a commercial power meter (Laser Pointer Store, China). The equation for the calibration curve is provided in Fig. 3.3b. When approaching 0% or 100% duty cycling (Fig. 3.3c and 3.3d, respectively), the relationship exhibited stepwise behaviour, thus limiting the linear region between 0.25 W to 3.78 W laser output.

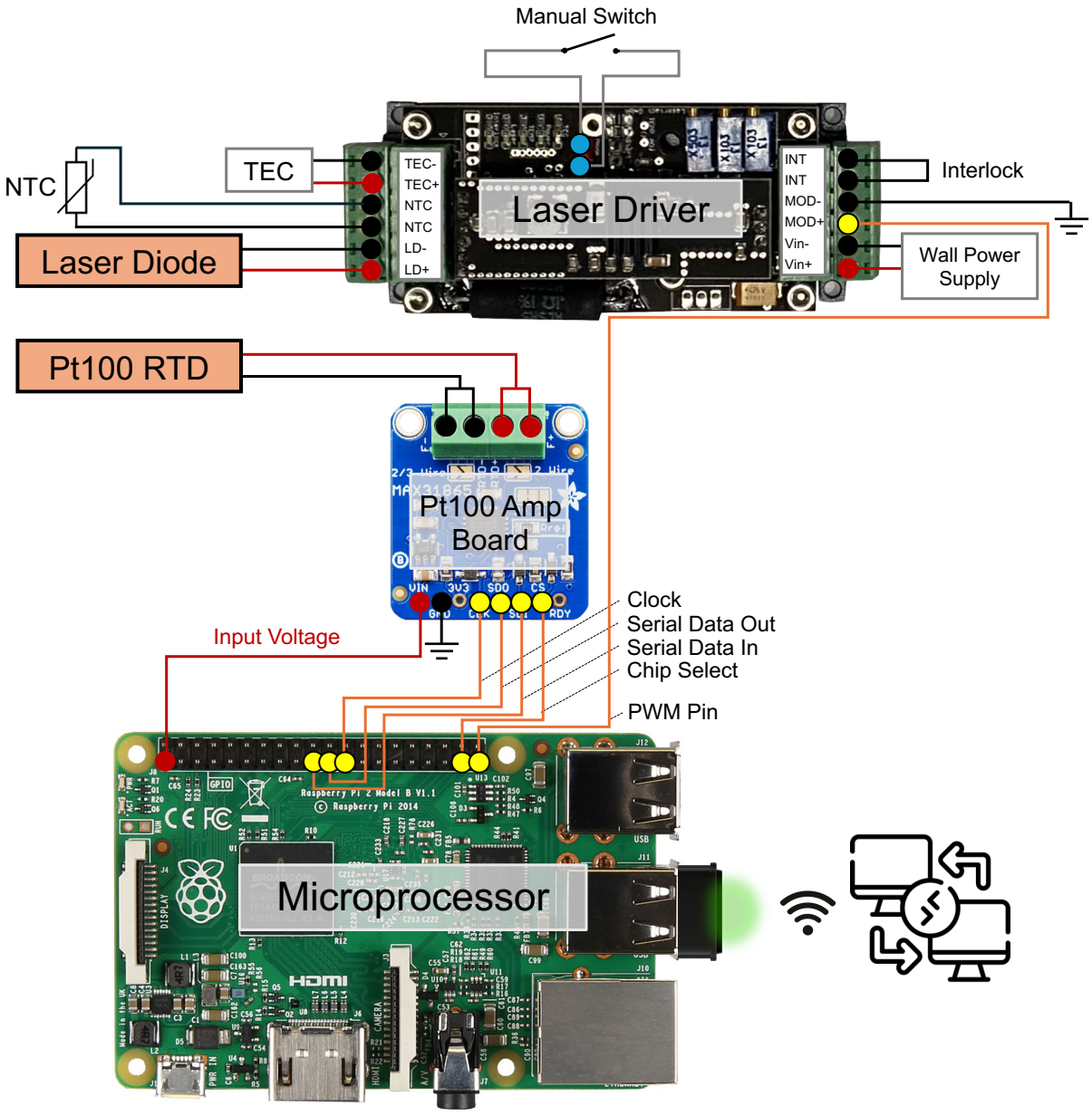


Figure 3.2: Schematic for all connections of the integrated laser-temperature sensor system.

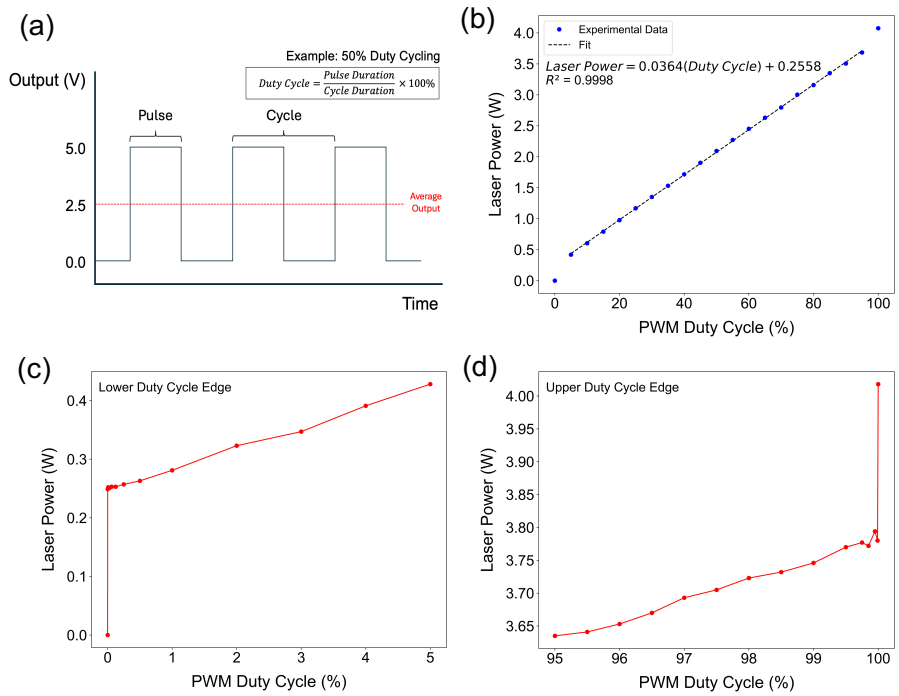


Figure 3.3: Characterization of laser output control by PWM: (a) Operating principle of PWM with an example of 50% duty cycling, (b) Full RPi duty cycle range with the linear region limited to between 0.25 W to 3.78 W laser output, (c-d) Lower and upper edges of duty cycle-laser power relationship exhibit stepwise behaviour.

An overview of the major components in the photothermal characterization system is shown in Fig. 3.4a. The process zone of the gel-sample holder system based on a sandwich of glass slides and wire spacers is illustrated in Fig. 3.4b. A photograph of the full benchtop photothermal characterization setup is shown in Fig. 3.5. The end of the laser-coupled fiber was mounted to a lens tube with internal threading (SM05L20C, Thorlabs, USA). An aspheric collimator lens (CM110TMD, Thorlabs, USA) was mounted 1.1 mm from the fiber end via a threaded lens cell adapter (S05TM09, Thorlabs, USA). The lens tube was clamped in place using a custom 3D-printed stand (Fig. 3.4b) at a working distance (WD) of 66.25 mm overhead the Pt100 RTD. CAD drawings of the lens tube clamp are provided in Appendix Section C.1. The selected WD allows for comfortable loading of samples on the stage and ample heat generation upon laser irradiation. The resulting laser spot has a fixed diameter of 2.72 $\pm$ 0.070 mm and a covered area similar in size to that of the Pt100 resistor serpentine. The method for estimating the laser spot size is provided in Appendix Section E. The Pt100 is affixed onto a lower glass slide on a

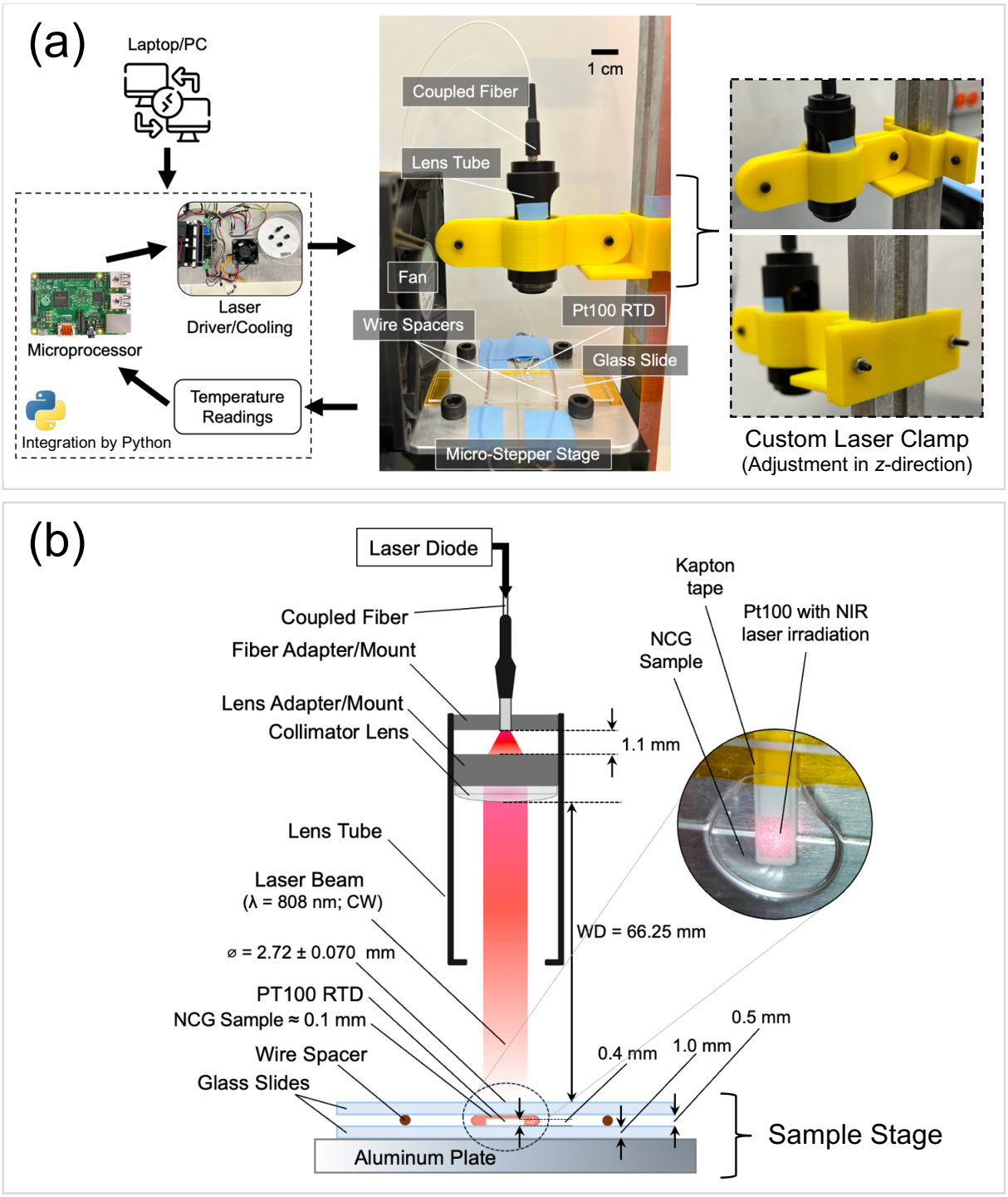


Figure 3.4: Photothermal characterization setup: (a) Overview of photothermal characterization system. Integrated laser control and temperature sensing is enabled by the RPi microprocessor using Python. Custom 3D-printed laser clamp allows for vertical height adjustment of the laser. (b) Detailed illustration of process zone of setup.

micro-stepper stage using Kapton tape. Two wires of the same gauge are secured on either side of the Pt100 sensor. A chassis fan was affixed adjacent to the work surface to provide continuous air circulation and promote steady-state conditions. The laser spot (Fig. 3.4b inset) is observed

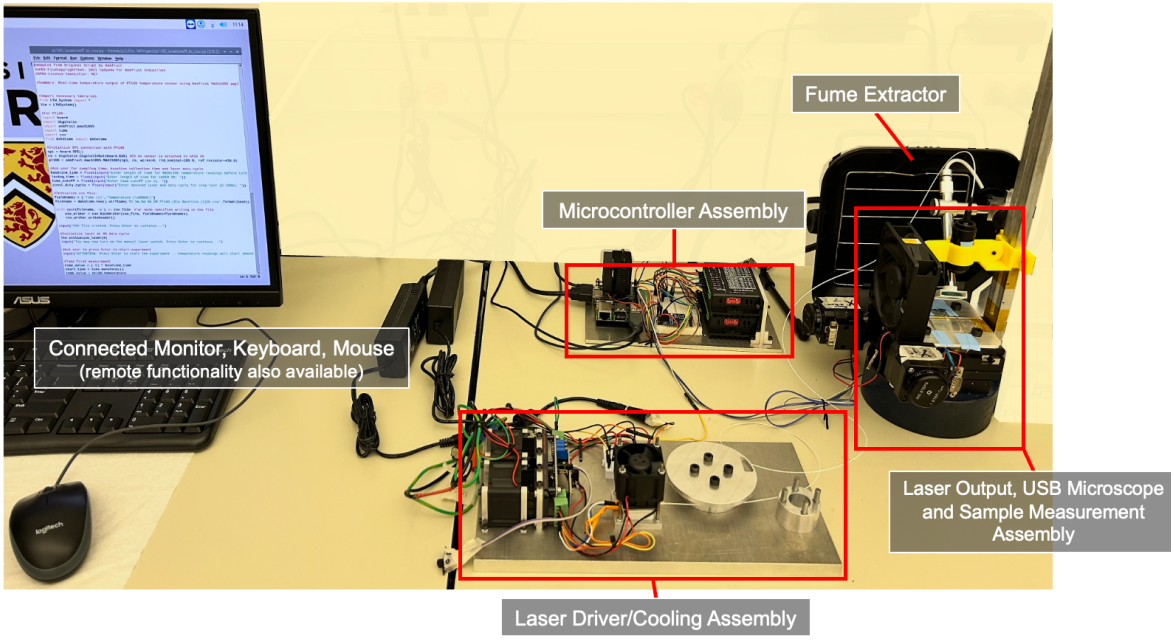


Figure 3.5: Photograph of the full benchtop photothermal characterization setup with microscope and attached glass filters for observing laser spot.

using a NIR sensitive USB microscope combined with stacked antireflection-coated coloured glass filters (Thorlabs, USA), which provide $\approx 1\%$ transmission of 800 nm light. The glass filters were positioned directly against the head of the microscope using a custom 3D-printed attachment (Fig. 3.6). The CAD schematic for the glass filter attachment is provided in Fig. C.4 (Appendix). For the laser alignment procedure, a live microscope feed on a nearby laptop is used in tandem with the PWM code (Listing D.2, Appendix). The `duty_cycle` variable in the PWM code is set to a low value (e.g., 12%) for a clear visual of the laser spot in the microscope feed. Usage of higher laser duty cycles is avoided as it can cause image overexposure. Precise alignment of the Pt100 RTD beneath the laser beam is achieved using micron-sized manual adjustments enabled by the stage.

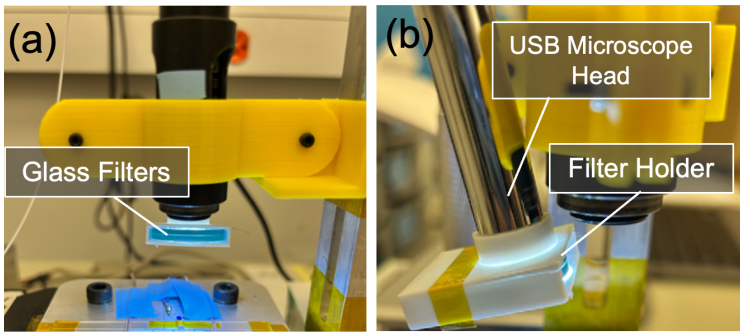


Figure 3.6: Photothermal characterization setup with microscope and attached glass filters for observing laser spot: (a) Front view of glass filter attachment on microscope head positioned overhead the Pt100 (b) Side view.

3.3 Achieving Measurement Repeatability and Stability by Defined Geometric Arrangements

The photothermal characterization method involves first applying a small amount (≈ 15 µL) of gel specimen to the Pt100 RTD surface. The gel was then compressed to a fixed thickness defined by the distance from the top of the Pt100 RTD to the bottom of the top glass slide. The placement of two weights (≈15 g each) on the top glass slide above the wire positions encourages even compression and gel thickness uniformity. The top glass slide further acts as a heatsink to draw excess heat from the lased sample and therefore can provide an assessment of heating behaviour that is minimally affected by the insulating nature of air. The transmission of soda lime glass substrates at 800 nm has been reported to be roughly 90% for a thickness of 1 mm [97] (i.e., the same glass thickness used in the presented setup). Therefore, it is expected to reduce the amount of irradiation that reaches the sample. As well, the gel sample itself actively absorbs and dissipates heat within the setup (Fig. 3.7).

The usage of wire spacers allows for repeatable and controlled laser-induced heating of the gel specimens. The standard error of the mean of ΔT for an example set of ten sample measurements was 0.123°C, highlighting the repeatability of the reported method. To select a suitable gel thickness for future temperature testing, a preliminary study involved implementing different wire diameters, resulting in different gel thicknesses (0.1, 0.4, 0.6, 1.1 mm), under 2.4 W laser irradiation. Fig.s 3.8a-d show the temperature curves obtained for control gels and gels containing 0.4 nM GNRs for each gel thickness ($n = 3$). It was found that heating performance (ΔT) did not increase as the gel thickness increased, despite the increase in material volume (Fig. 3.8e). More-

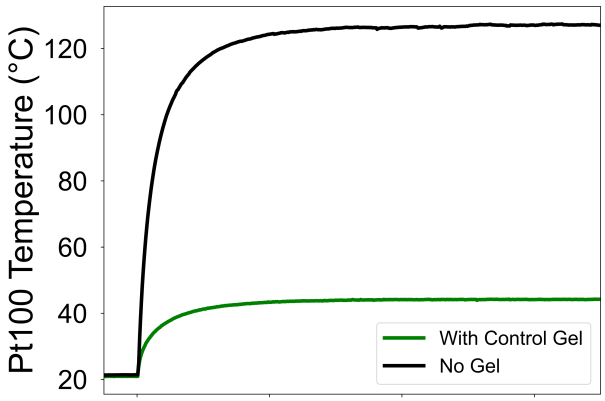


Figure 3.7: Comparison of temperature curves when a gel sample (0 nM GNRs, 0% w/v GG) is absent versus present under 2.4 W (41.3 W/cm^2) laser irradiation. The gel plays an active role in dissipating heat from the setup. Curves were obtained using the dual glass slide setup depicted in Fig. 3.4.

over, for LTW, NCGs are typically applied as thin coatings. Therefore, a nominal gel thickness of 0.1 mm was selected as a relevant use case. It should be noted that in this preliminary study, the distance between the collimator lens mount and fiber end was 0 mm, resulting in a smaller laser spot size ($<$1 mm) and therefore much larger power density ($>$305 W/cm^2) than what was reported in Section 3.2. Under these conditions, carbonization, or the full thermal degradation, of gel samples was observed in certain gel thicknesses as charring or blackening. The onset of carbonization is reflected in the abrupt changes in heating dynamics visible in 3.8c-d.

To eliminate the occurrence of carbonization, the distance between the collimator lens mount and fiber end was increased to the final distance of 1.1 mm (as depicted in Fig. 3.4b), giving a laser spot size of 2.72 $\pm$ 0.070 mm, as reported in Section 3.2. With this setup configuration, stable temperature readings were repeatably obtained under continuous lasing of up to 150 s, without gel carbonization (Fig. 3.9).

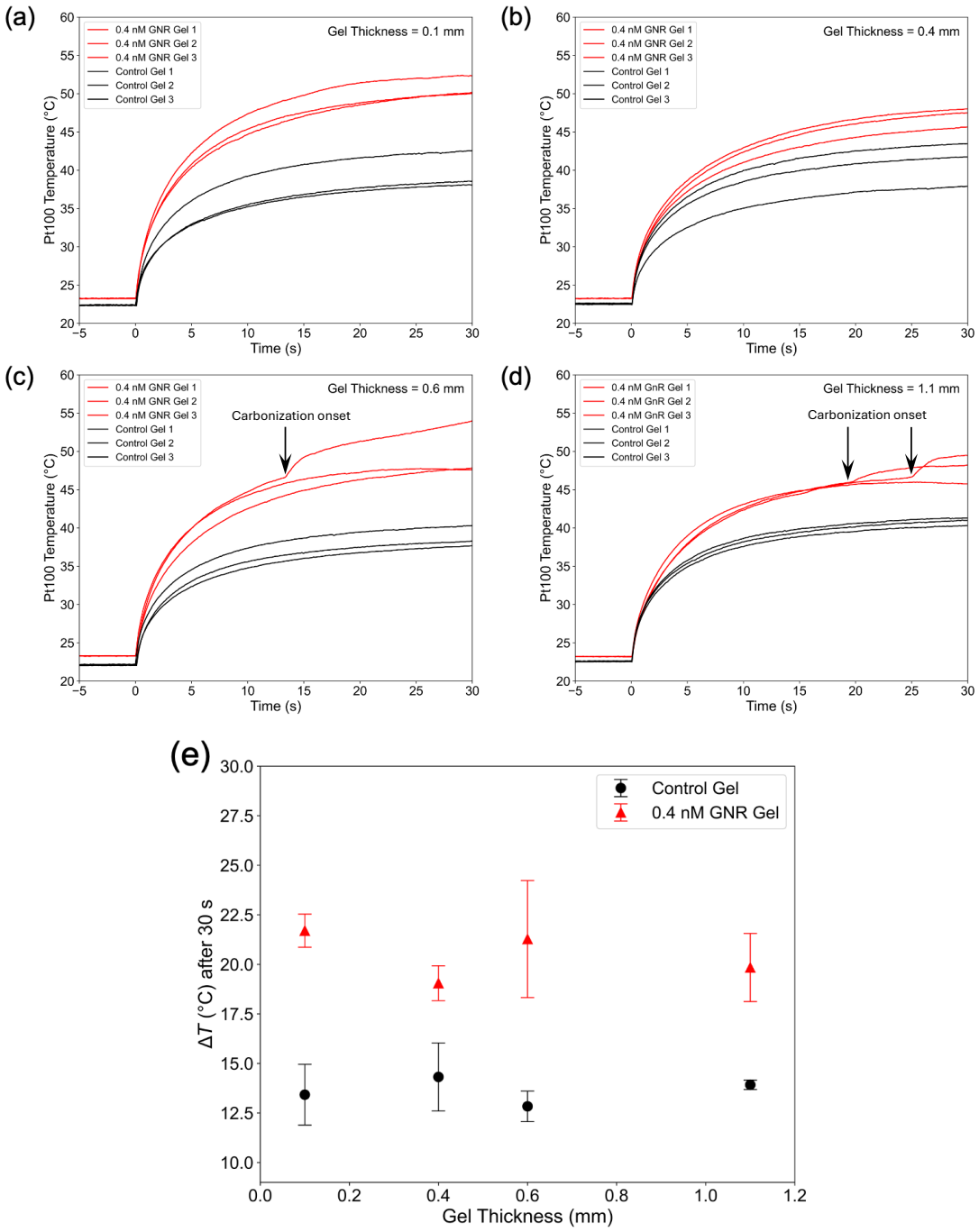


Figure 3.8: Comparison of temperature curves recorded with laser irradiation commencing at t = 0 s for various nominal gel thicknesses (a) 0.1 mm, (b) 0.4 mm, (c) 0.6 mm, (d) 1.1 mm. (e) Summarized. All curves were obtained using the dual glass slide setup in Fig. 3.4, except the distance between the collimator lens mount and fiber end is 0 mm, instead of 1.1 mm.

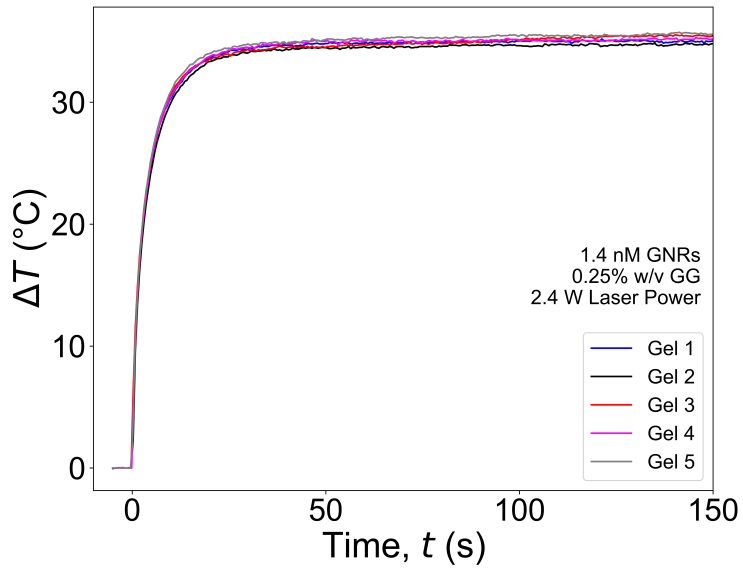


Figure 3.9: Long-term measurement stability for 150 s of continuous lasing. There were no observations of carbonization.

3.4 Temperature Collection Scheme

With the finalized photothermal characterization setup (Fig. 3.4), the following laser-RTD workflow was used to measure the temperature of gel specimens over time:

1. Baseline ambient temperature collection for 5 s
2. CW laser irradiation at a constant power of 0.98, 1.7, or 2.4 W (power densities of 16.9, 29.3, or 41.3 W/cm^2, respectively) with temperature collection for 30 s
3. Laser off and cooling temperature measurements for 30 s

A Python script (Listing D.3, Appendix) was written for semi-automation of this workflow. Example heating curves obtained with this setup for a typical NCG specimen and a control specimen without GNRs are shown in Fig. 3.10a. Example heating curves for specimens containing different GG concentrations are shown in Fig. 3.10b. The value ΔT was extracted from these curves as the difference between the average baseline temperature over 5 s (T_{amb}) and the final temperature prior to laser shut-off at t = 30 s ($T_{t=30\,s}$) and is used as a characteristic value of heating performance.

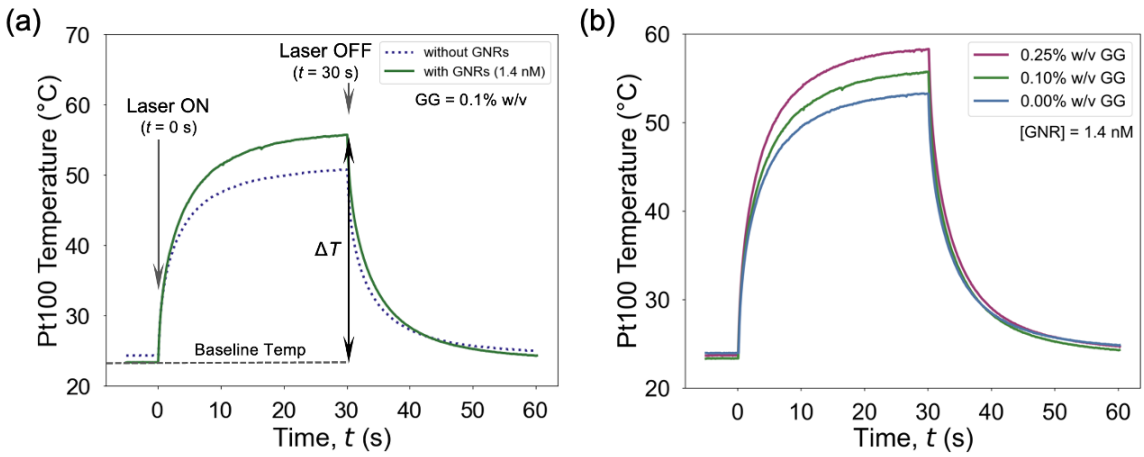


Figure 3.10: Example curves characterizing the heating behaviour of gel samples using the custom setup: (a) Gel specimens with 1.4 nM GNRs and without GNRs, (b) Gel specimens with increasing GG concentration. Laser power was 2.4 W (41.3 W/cm^2). Duration of irradiation was 30 s.

An irradiation dwell time of 30 s at maximum 2.4 W was selected as it was rationalized that this time frame is narrow enough to allow for rapid and convenient operation, but still wide enough to accommodate procedure flexibility and safety. A visual summary of the full RTD measurement scheme is provided in Fig. 3.11. This measurement scheme can be applied to control and GNR-containing gels to determine their ΔT values. As will be discussed in later chapters, these ΔT values can be further used to evaluate clinical relevance via the plasmonic heat amplification factor, ξ (Chapter 4) and photothermal conversion efficiency, η (Chapter 5) of NCGs. The photothermal characterization scheme is visualized in Fig. 3.12.

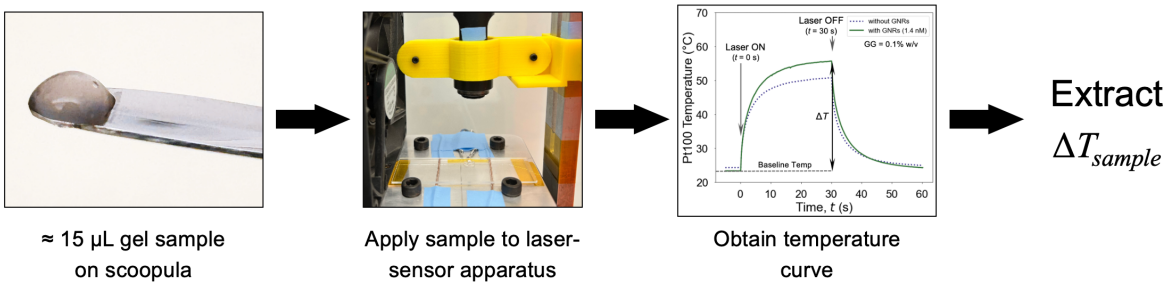


Figure 3.11: Overview of RTD measurement scheme for a gel sample.

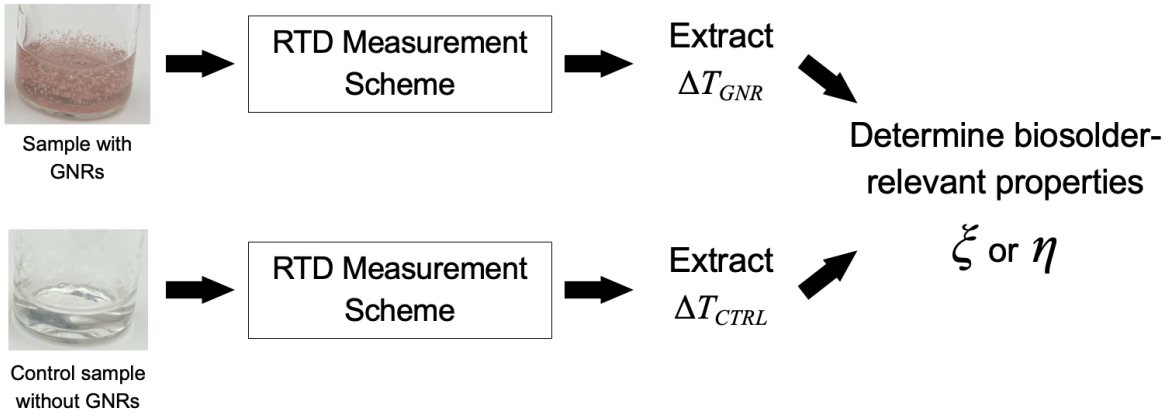


Figure 3.12: Overview of photothermal characterization scheme for control and GNR-containing NCG biosolders. From this, biosolder-relevant properties can be determined, such as the plasmonic heat amplification factor, ξ, and the photothermal conversion efficiency, η.

3.5 Cost Estimation for Characterization System

Table 3.1 shows the estimated cost breakdown for the photothermal characterization setup from Fig. 3.4. The majority of the cost is for the laser components. Given the repeatability and usefulness of this custom system for NCG evaluation, the price point is reasonable. In a clinical setting, only the laser components and microcontroller will be implemented; in that case, the expected price point is $\approx$ $996.

Table 3.1: Cost breakdown for photothermal characterization system.

System Aspect	**Included components**	**Total Cost** ($)
Laser	laser diode, laser driver, fans, heat sinks, TEC, NTC, lens tube, collimator lens, lens adapter,fiber, end adapter	942.64
Temperature Sensing	Pt100, Pt100 amplifier board	20.26
System Integration	RPi 2 Model B, RPi fan, wi-fi dongle	110.88
Sample Stage	Repurposed XY stage, glass slides, spacer wires, USB microscope, glass filters, stand for laser clamp	323.31
3D-Printed Parts	laser clamp, glass filter holder	0.60
Total		1397.69

3.6 Summary

A photothermal characterization system with integrated laser power control and continuous temperature measurement via a Pt100 RTD, was developed. The setup enables repeatable and stable measurements of ΔT for gel biosolder samples over time (see Fig. 3.13). The proposed characterization method can be used to determine biosolder NCG properties, such as the plasmonic heat amplification factor, ξ, and the photothermal conversion efficiency, η.

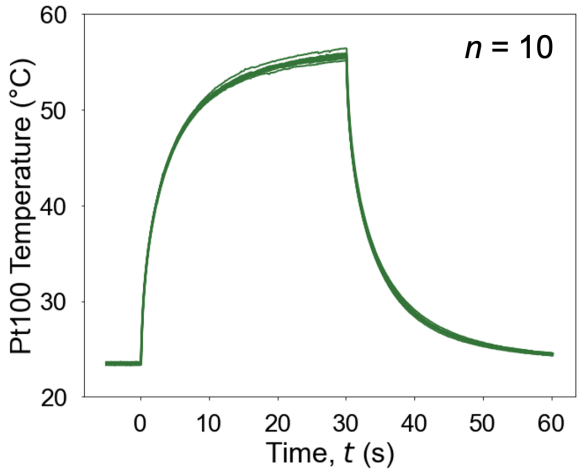


Figure 3.13: Example data set for 10 gel samples prepared from the same batch (1.4 nM GNRs, 0.1% w/v).

Chapter 4

Assessing the Clinical Relevance of Developed Biosolders

This chapter reports the main effects on NCG heating performance using a 3×3×3 design of experiments (DOE) and ANOVA. As well, a plasmonic heat amplification factor is proposed as a design metric to assess the thermal suitability of developed NCG biosolder formulations for LTW. The content of this chapter overlaps with that of my co-authored manuscript submission named in Section 1.4.

4.1 Main Factors for LTW with Biosolders: Quantifying Effects on Heating Performance (ΔT) using DOE/ANOVA

4.1.1 Design Space Selection and DOE/ANOVA Methods

The three main factors influencing ΔT that were considered are laser power, GNR concentration, and GG concentration. There is an established linearity between input laser power and the resulting temperature change [63]. It is also well-known that GNRs exhibit plasmon decay under laser irradiation, which can provide enhanced temperature increases when they are incorporated into a given matrix material [9, 10, 33, 98, 99, 100, 101]. It is proposed that the presence of guar gum in the developed NCG enhances GNR stability, particularly when the GNR concentration is increased. Poor GNR stability notoriously results in aggregate formation and a resultant loss of

their desirable photothermal property due to the change in average particle size. Two proposed mechanisms for the gum stabilization effect are physical interference following gum adsorption on particle surfaces, and decreased GNR diffusion due to increased viscosity. These mechanisms were reported for iron micro- and nanoparticles [102] but have since been inferred to extend to gold nanoparticles [55].

The design space was selected through initial probing of the three factors: GNR concentration, GG concentration, and laser power. Laser exposure time is a fourth main factor that was kept at 30 s and not varied. NCGs were prepared with GNR concentrations (0.7 nM and 1.4 nM) similar to that successfully used in [33, 17] to control nanomaterial exposure to potential patients. Following this, a range of GG concentrations (0.00% w/v–0.75% w/v) were probed for the selected GNR concentrations. The GG concentrations 0.1% w/v and 0.25% w/v were selected since they provided distinct differences in GNR stabilization in NCG specimens, as evidenced by their differences in colour (Fig. 2.10). Furthermore, at these GG concentrations, the gels remained "workable" (i.e., they could be easily spread across a surface). GG concentrations higher than 0.25% w/v made the gel too solid without further GNR stabilization. Specimens without GG were prepared as negative control. Finally, a range of laser power levels (0.6 W–2.8 W) were used to irradiate NCG samples and 2.4 W with the presented laser configuration in Fig. 3.4 was sufficient to achieve the target temperature of around 60°C. A summary of the design space for the 3×3×3 DOE is shown in Fig. 4.1. All 27 conditions were randomized, each repeated 10 times, and the setup reported in Fig. 3.4 was used with the temperature collection scheme described in Section 3.4 to obtain ΔT at the end of laser irradiation. A three-way Type I ANOVA was carried out to evaluate the extent to which GNR concentration, GG concentration, laser power, and two-way interactions thereof influence ΔT. This was followed by Tukey's HSD post-hoc test [103] to determine which groups are statistically different from their corresponding control group (0% w/v GG, same GNR level).

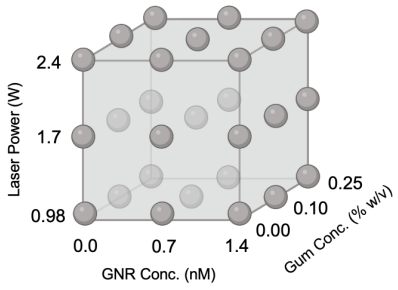


Figure 4.1: Design space containing DOE factors and levels. The nine unique gel formulations with varied GNR concentration and GG concentration correspond to those photographed in Fig. 2.10. Graphic produced with BioRender.

4.1.2 DOE/ANOVA: Results and Discussion

For each of the 27 conditions summarized in the design space, the mean ΔT and standard deviation for each sample set (n = 10) were calculated using standard methods. These results are visualized in Fig. 4.2 alongside box and whisker plots of ΔT under all 27 conditions. The ANOVA results are reported in Table 4.1.

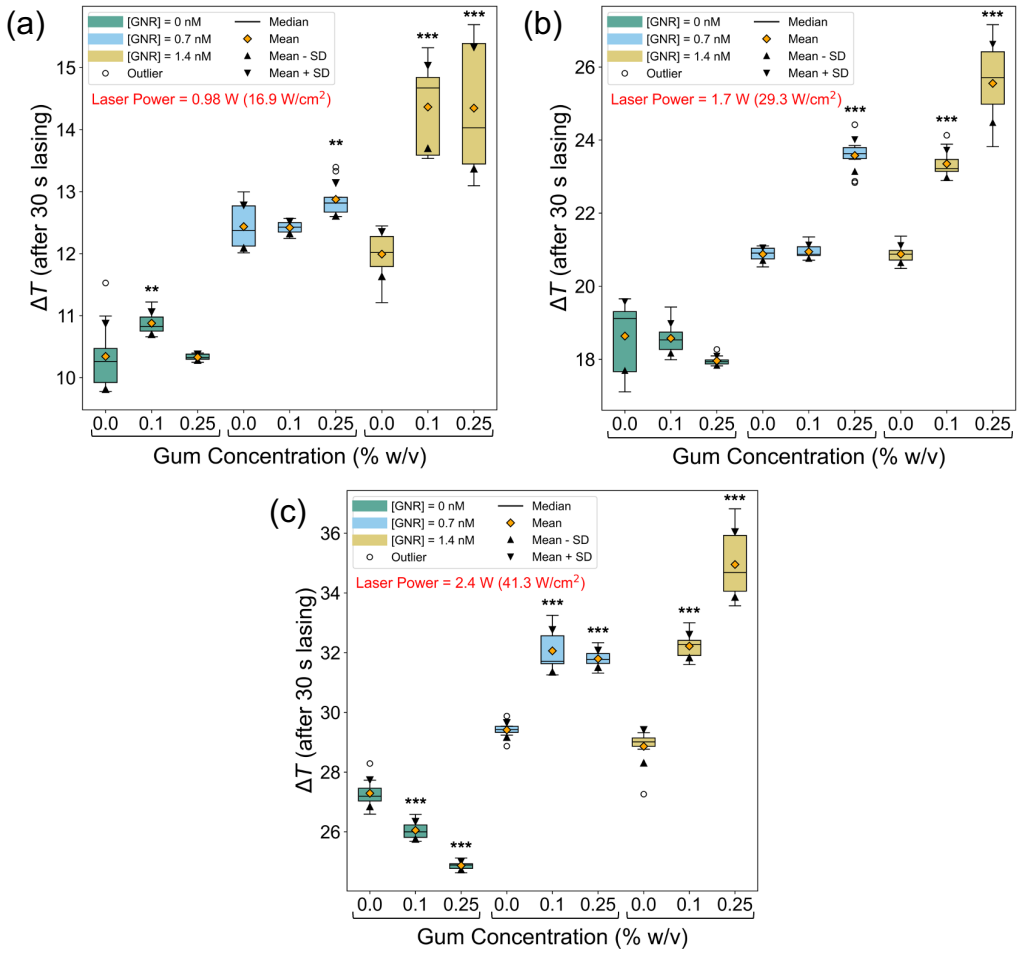


Figure 4.2: Box and whisker plots of average ΔT of gel specimens irradiated under (a) 0.98 W, (b) 1.7 W, and (c) 2.4 W laser power, n = 10. Baseline temperatures ranged from 22.2°C –24.8°C. The asterisks indicate statistically significant differences from the corresponding control group (0% w/v GG, same GNR level) based on Tukey's HSD test; $p \leq 0.05$ (*),$p \leq 0.01$ (**), $p \leq 0.001$ (***).

Table 4.1: Three-way ANOVA to evaluate the effect of GNR concentration, GG concentration, laser power, and two-way interactions thereof on ΔT of NCG samples irradiated for 30 s.

Factor	**Df**	**Sum Sq**	**Mean Sq**	F	p
GNR	2	104.50	52.25	57.33	1.81×10^{-5}
GG	2	13.81	6.90	7.57	0.014
Laser Power	2	1378.93	689.46	756.52	7.65×10^{-10}
GNR:GG	4	22.28	5.57	6.11	0.015
GNR:Laser Power	4	8.82	2.21	2.42	0.13
GG:Laser Power	4	2.40	0.60	0.66	0.64
Residual	8	7.29	0.91	—	—

At a laser power of 0.98 W, the incorporation of 1.4 nM GNRs increased ΔT by almost 50% when compared to negative control samples. Similarly, the addition of 1.4 nM GNRs resulted in an increase in ΔT of $\approx 44\%$ under 1.7 W laser irradiation and $\approx 36\%$ under 2.4 W laser irradiation at a constant GG concentration of 0.25 % w/v. The ANOVA results confirms that GNR concentration has a significant effect on the ΔT of gel specimens ($p < 2 \times 10^{-5}$), however the direct effect of laser power is more substantial ($p < 1 \times 10^{-9}$).

The role of GG as a GNR stabilizer is herein confirmed by the significant increase in average ΔT as GG concentration is increased for NCG samples containing 0.7 nM and 1.4 nM GNRs (Fig. 5b and Fig. 7). Increasing the GG concentration from 0 % to 0.10 % w/v increased the average ΔT by roughly 6.089 °C in samples containing 1.4 nM GNRs under 2.4 W laser irradiation for 30 s. As well, for samples containing 0.7 nM GNRs under 2.4 W laser irradiation, a saturation in ΔT was observed for formulations with only 0.10% w/v GG, indicating that under these conditions, a lower GG concentration is sufficient for GNR stabilization. Furthermore, visual confirmation of gum stabilization is provided by Fig. 2.10, in which the characteristic purplish-grey hue of aggregated gold nanoparticles is only visible in gel samples without GG. From the ANOVA results (Table 4.1), GG concentration ($p = 0.014$) is proved to be significant in influencing NCG heating performance. Moreover, multiple linear regression analysis was performed with and without an interaction term between GNR and GG concentrations. When the GNR:GG interaction is considered in the regression model, the adjusted R^2 value increases from 0.963 to 0.978, indicating the importance of GNR:GG interaction as a predictor of heating performance.

4.1.3 Comparison of New Laser-NCG Configurations to Prior Literature

Due to the positive correlations established between the three DOE factors and heating performance, the largest average ΔT = 34.953°C was obtained for specimens under maximum level conditions (1.4 nM GNRs, 0.25 % w/v, under 2.4 W laser power), a value sufficiently high for LTW. LTW relies on heat generation of NCG materials to at least 60°C, or ΔT = 23°C, assuming ambient body temperature is 37°C. In the present study, moderate heating to a maximum temperature of approximately 60°C was attained in under 30 s of irradiation at 2.4 W power and a fixed spot size of 2.72 $\pm$ 0.070 mm (41.3 W/cm^2). This temperature was achieved using a low GNR concentration of 1.4 nM (which is relatively low compared to those reported [9, 10, 13]) and a setup with a relatively low thermal resistance of <55°C/W. Details for the determination of thermal resistance are provided in Section 5.4. Previous work in the field of LTW reported the heating of a collagen-based NCG up to 60°C over a similar timeframe, however this was achieved with a lower laser power density of 1.50 W/cm^2–1.83 W/cm^2 and a GNR concentration of 5 wt%, or roughly 569 nM, which is two to three orders of magnitude larger than our GNR concentrations [9]. Gum-stabilized GNR dispersions have also been reported to achieve temperatures of 40°C–60°C under laser irradiation over a longer dwell time of 300 s and a lower laser power density of 0.5 W/cm^2–1 W/cm^2 [53]. In general, administration of a low laser power density necessitates longer irradiation times due to lessened photothermal activation of GNRs. Furthermore, reducing the laser power density restricts the maximum ΔT that can be attained, due to the linearity between input power and the resulting temperature change [63].

4.2 The Plasmonic Heat Amplification Factor (ξ) as a Design Metric

4.2.1 Thermal Damage Considerations for LTW

Fig. 4.3 summarizes the thermal damage effects expected in skin tissue for surface temperatures over time. The boundary defining regions of no thermal effect and hyperthermia (threshold function 1) were determined experimentally by Williamson and Scholtz in 1949 [104]. The boundaries defining the occurrence of partial thickness and full thickness burns (threshold functions 2 and 3) were both determined by Moritz and Henriques [105] and Sevitt [106] in the 1940s, and consolidated by Bull some decades later [107]. Similar regimes have been reported by [108, 109, 110]. In the hyperthermia region, the surface of the tissue can present with reversible reddening or raised lesions called papules [104]. As the temperature and duration of heat exposure increases, partial thickness burns (also called second-degree burns) manifest. Beyond this

point, the process of coagulation necrosis takes place [109], in which cell death and protein denaturation occurs. The severity of partial thickness burns and the need for enhanced treatment increases with the depth of damage [111]. Full thickness burns (also called third-degree burns) are the most severe cases in which damage extends through the entirety of the epidermis and underlying dermis of skin.

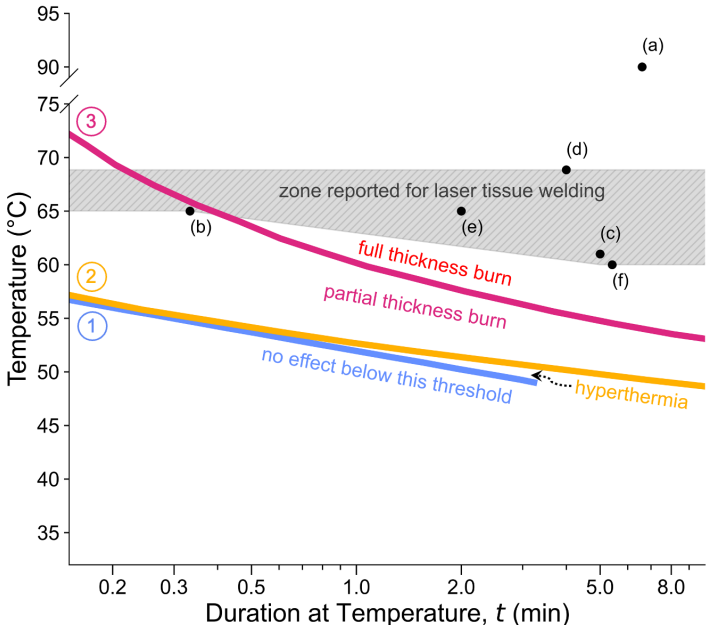


Figure 4.3: Thermal effects expected to occur in skin tissue based on temperature and exposure. Threshold functions 1, 2, and 3 define the minimum conditions for which hyperthermia, partial thickness burn, and full thickness burn occur, respectively. (a–f) LTW process parameters from literature ([14], [15], [10], [9], [13], [16], respectively).

In order to maximize the benefits of LTW as a wound closure procedure, it is important to confine the thermal damage, as much as possible, to the site of joining. Such heat localization also accelerates wound healing by keeping the temperature of the tissue surrounding the site of joining predominantly within the no-effect region of Fig. 4.3. Also shown in Fig. 4.3 are typical reports of successful LTW in *ex vivo* and *in vivo* models (points a–f) currently which fall mostly within the domain of full thickness burns.

4.2.2 Predicting Clinical Relevance of Developed Biosolders for LTW

To assess the heat localization capability, and therefore, clinical relevance of an NCG biosolder formulation, the plasmonic heat amplification factor (ξ) is proposed. It is defined as the ratio of the temperature-increase in a given NCG with GNRs divided by that in its control gel:

$$\xi = \frac{\Delta T_{GNR}}{\Delta T_{CTRL}} \tag{4.1}$$

where ΔT_{GNR} is the average $T_{max} - T_{amb}$ measured for NCG samples and T_{max} is the maximum or steady-state temperature. ΔT_{CTRL} is the average $T_{max} - T_{amb}$ for the corresponding control gels. Assuming the thermal conductance is the same in both the NCG and its control gel, ξ appropriately quantifies the heat amplification solely due to the addition of GNRs. In the context of LTW, ΔT_{GNR} clinically approximates the temperature increase available for the welding process, and ΔT_{CTRL} is the increase experienced in surrounding irradiated tissue where the GNR is absent, assuming equal tissue heating with and without control NCG.

The desired amplification factor, ξ_{min}, represents the minimum amplification factor for which sufficient tissue welding is expected at an incision site with no thermal damage sustained in the surrounding tissue. It is the proposed design metric for LTW and is defined as

$$\xi_{min} = \frac{\Delta T_{weld}}{\Delta T_{safe}} = \frac{T_{weld} - T_{start}}{T_{safe}(t_{expose}) - T_{start}} \tag{4.2}$$

where T_{weld} is the typical required temperature for tissue welding (60°C) [9], T_{start} is the initial temperature (e.g., skin temperature at 32°C), and $T_{safe}(t_{expose})$ is the maximum tissue temperature, for a given heat exposure duration, t_{expose}, at which no negative thermal effects take place. The value of $T_{safe}(t_{expose})$ is estimated using threshold function 1 (blue) in Fig. 4.3. If an NCG achieves $\xi > \xi_{min}$ while reaching a sufficiently high T_{weld} and maintaining its surroundings at a safe temperature within the no-effect zone, then it is considered clinically relevant and safe. Essentially, it has the potential to provide reliable tissue welds in a confined manner, such that peripheral and underlying tissue, where the gel is absent, do not experience undesirable thermal effects. Since the maximum temperature or ΔT experienced by tissue is the determining factor for thermal damage regardless of heating dynamics, the proposed metric, ξ, is assumed suitable for the thermal safety aspect of a NCG formulation. Factors describing temperature increase have been previously reported in the context of photothermal cancer therapy (PTT) (e.g., [112]). However, these metrics only pay focus to the temperature required for cell necrosis and tissue death. Conversely, the proposed safety benchmark, ξ_{min}, is specific to LTW and considers both the required target temperature for positive procedure outcome and the maximum allowable temperature to mitigate unnecessary thermal damage.

Applying the proposed methodology for 30 s of laser irradiation, $T_{safe}(t_{expose} = 30\text{ s})$ is approximately 53.7°C. Assuming an initial temperature T_{start} of 32°C and a weld temperature T_{weld} of 60°C, the value of $\xi_{min}(t_{expose} = 30\text{ s}) \approx 1.29$.

Experimental values for ξ were determined for each of the six GNR-containing NCG gels as shown in Fig. 4.4 (n = 5). The sample size was reduced compared to the DOE since it was found that sample sizes of 5 and 10 possessed similar maximum standard deviation values for ΔT (0.988°C and 1.047°C, respectively). Under laser irradiation at 2.4 W, three out of the six tested formulations met the $\xi > \xi_{min}$ criterion (i.e., 0.7 nM GNRs with 0.25% w/v GG, 1.4 nM GNRs with 0.1% w/v GG, and 1.4 nM GNRs with 0.25% w/v). For a GNR concentration of 0.7 nM, the addition of GG at a concentration of 0.25% w/v provided a clinically relevant formulation for LTW. Similarly, so does a GNR concentration of 1.4 nM, with a GG concentration between 0.065% w/v and 0.25% w/v.

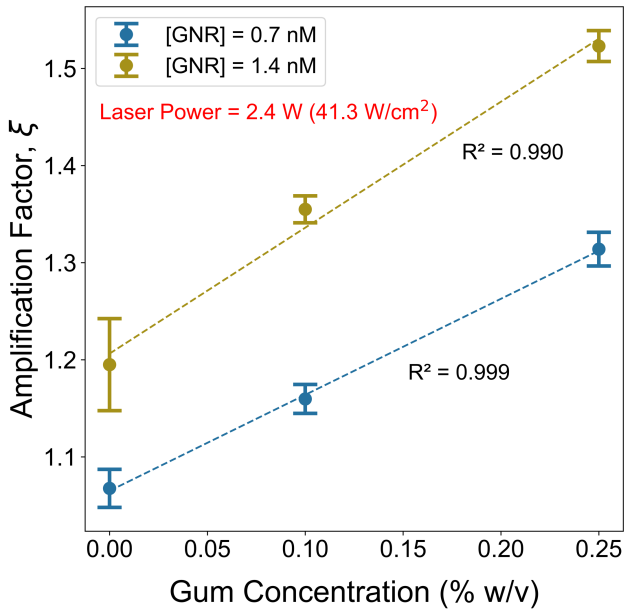


Figure 4.4: Effect of guar gum on plasmonic heat amplification factors for GNR-containing NCGs (n = 5).

Additional work is suggested to fully predict clinical success of LTW for wound closure, including correlating these findings to what is observed in *ex vivo* and *in vivo* models, as well as studies of biocompatibility, cooling by blood perfusion, or radii of thermal events (such as hyperthermia, partial and full thickness burns). While NCGs reported here are predicted to fulfill the $\xi > \xi_{min}$ criterion for safe LTW, the following are suggestions for additional performance improvements:

1. Increase GG concentration to determine if concentrations above 0.25% w/v continue to increase ξ linearly.
2. Decrease exposure time as it increases the no-effect threshold.
3. Reduce the start temperature.

4.3 Summary

Positive correlation between ΔT and three main factors (GNR concentration, GG concentration, and laser power) were confirmed. The interaction between GNR concentration and GG concentration was found to be a significant contributor to gel heating performance. This is, to my knowledge, the first report on the direct influence of additive gums on the heating performance of highly viscous photothermal GNR-containing gels. The incorporation of GG in the tested gel biosolders improved the stability of the dispersed GNRs, therefore enhancing their plasmonic heating under laser irradiation.

With the proposed methodology, it was possible to confirm the sufficiency of plasmonic heating to allow for potentially safe LTW. As well, a metric to determine clinical relevance and safety is now available for that purpose (i.e., a plasmonic heat amplification factor). A subset of the developed NCG biosolder formulations was found to be clinically relevant. The work presented here is a useful framework to assess the readiness of biosolder formulation for future administration to tissue models and can improve precision and speed for testing of biosolder materials toward their intended application.

Chapter 5

Alternative Method for Determining Photothermal Conversion Efficiency (η) of NCGs

This chapter proposes an alternative method for determining η to address the inconsistencies in η determination methodologies reported in literature. η is determined for the six GNR-containing gel biosolder formulations developed and reported in Section 2.3.

5.1 Motivation and Current η Determination Methodologies

As briefly mentioned in Section 1.2.5, there are inconsistencies across current η estimation methodologies. Specifically, there is no consensus as to how key variables, such as the time constant and mass, are calculated [71]. In response, [71] proposed a standardized method for determining η which involves the use of a thermal camera to monitor the temperature of a suspended droplet of aqueous gold nanoparticles under laser irradiation and humidity-controlled conditions [71]. Their method is quick, eliminates the need for mass correction and avoids discrepancies in the placement of point temperature probes (e.g., thermocouples). However, such a setup still requires close attention to laser alignment on the droplet. As well, this method is restricted to a temperature change, ΔT, of no more than 10°C to minimize evaporation, which limits the relevant applications for which it can used. For example, a ΔT of 10°C is sufficient for photothermal cancer therapy, but for LTW, a ΔT of about 23°C is required. Furthermore, the suspended-droplet method was not used for gel materials that may not form into the desired droplet shape necessary for repeatable laser heating.

The presented work describes an alternative and simple method for determining η of highly viscous NCGs. The method bypasses the determination of time constants and mass, reducing the need for assumptions and standardization. To achieve this, the same RTD-based photothermal characterization setup described in Section 3.2 was used. This further underscores the relevance and usefulness of the reported setup as it finds utility for both the evaluation of clinical relevance and the determination of η for gel biosolders.

5.2 Steady-State Simplification of η Definition

The heating regime solution for θ of a laser-irradiated photothermal material was provided in Section 1.2.5, Equation (1.8). To reiterate,

$$\theta_{GNR} = \frac{Q_{in} + Q_0}{hA(T_{max} - T_{amb})} \left[1 - \exp\left(-\frac{-t_h}{\tau_{s,h}}\right)\right]$$

where t_h is the time after which the laser has been turned on. For a control gel, where GNRs are absent, Q_{in} = 0 and the above equation reduces to

$$\theta_{CTRL} = \frac{Q_0}{hA(T_{max} - T_{amb})} \left[1 - \exp\left(-\frac{-t_h}{\tau_{s,h}}\right)\right] \tag{5.1}$$

When $t = \infty$, or steady state is reached, $T = T_{max}$ and the input power and external heat flux are in equilibrium. Thus, for control gels at steady state, $Q_0 = Q_{ext}(t = \infty)$. With (1.3), this gives

$$Q_0 = hA \times \Delta T_{CTRL} \tag{5.2}$$

where $\Delta T_{CTRL} = T_{max} - T_{amb}$ for a control sample. Substituting (5.2) into (5.1) at $t = \infty$ gives $\theta_{CTRL} = \theta_{max} = 1$, which is commensurate with inputting $T(\infty) = T_{max}$ into (1.4) to give θ = 1. Similarly, for GNR-containing NCGs at steady state, $Q_{in} + Q_0 = Q_{ext}(t = \infty)$. With (1.3), this gives

$$Q_{in} + Q_0 = hA \times \Delta T_{GNR} \tag{5.3}$$

where $\Delta T_{GNR} = T_{max} - T_{amb}$ for a NCG sample. Substituting (5.3) into (1.8) at $t = \infty$ gives $\theta_{GNR} = \theta_{max} = 1$, which is again commensurate with inputting $T(\infty) = T_{max}$ into (1.4) to give θ

= 1. Combining (1.2), (5.2) and (5.3) provides a new formula to determine η,

$$\eta = \frac{hA(\Delta T_{GNR} - \Delta T_{CTRL})}{I_0(1 - 10^{-A_\lambda})} \tag{5.4}$$

Therefore, the quantities $\tau_{s,h}$, $\tau_{s,c}$, and $\sum_i m_i C_{p,i}$ are not necessary to determine η.

5.3 Experimental Determination of hA to Bypass the Usage of $\sum_i m_i C_{p,i}$ and Fitted Parameter τ_s

The mass of materials used to estimate $\sum_i m_i C_{p,i}$ have been reported with varying assumptions or limited transparency [71]. Some studies have overestimated the value of $\sum_i m_i C_{p,i}$ by considering the total mass of supporting materials (e.g., quartz or glass vessel, solution media) [63, 70], when only a percentage of their total masses may be involved in heat transfer. Moreover, the boundary conditions for heat transfer to the surroundings remain uncertain. Rearranging (1.5) for hA and substituting this into (5.4) shows that η is proportional to $\sum_i m_i C_{p,i}$. Therefore, overestimation of $\sum_i m_i C_{p,i}$ directly inflates the calculated value for η. Wang *et al.* combatted this with the use of a resistive heater to estimate the "effective mass" of the supporting quartz material that participates in thermal transfer [113]. In contrast, other studies have omitted the mass of the supporting glass or quartz when calculating $\sum_i m_i C_{p,i}$ [64, 65, 66, 67]. These discrepancies make it difficult to directly compare the η values obtained across these studies [71].

In addition to this, there exists the risk of systematically underfitting temperature data when using a non-linear model such as (1.8) to determine τ_s, due to the reality of imperfect experimental conditions. This can lead to inaccurate estimations of τ_s, Q_0, or η itself, depending on which variables are included in the fitting scheme. Moreover, it has been proposed that τ_s can be fitted using either heating regime data [69, 113] or cooling regime data [64, 65, 66, 67, 70]. However, the heating rate and cooling rate of a system are not always equal which introduces ambiguity as to which time constant is more appropriate to use [71].

To circumvent the need for $\sum_i m_i C_{p,i}$ or τ_s for the calculation of η, a direct determination of hA is proposed.

5.4 Determination of hA using RTD-Self Heating Method

The thermal conductance, hA, was estimated experimentally by determining the thermal resistance of the system, R_{th}, which is the inverse of hA. Briefly, various voltages (1.00, 2.00, 3.00,

4.00 V) were applied to the Pt100 sensor in the setup reported in Section 3.2, as shown in Fig. 5.1. A benchtop power supply was used as the voltage source. The resultant currents through the sensor were measured when steady state was reached after approximately 30 s of self-heating. These are are plotted in Fig. 5.2a. Corresponding powers were calculated by the $P = IV$ relation, and corresponding resistances were calculated by Ohm's law and subsequently converted to temperatures using an established conversion table (Intech Instruments Ltd., New Zealand). Temperature was plotted as a function of power and fitted using linear regression, as shown in Fig. 5.2b. The slope of the linear fit is equal to R_{th}. Assuming that all electrical power is converted to heat and that R_{th} is mainly the same for laser heating and RTD self-heating, hA was then calculated by

$$hA = \frac{1}{R_{th}} = \frac{\Delta(V \times I)}{\Delta T} \qquad [\mathrm{W}/^{\circ}\mathrm{C}] \quad (5.5)$$

where V is the applied voltage, I is the measured current, and T is the temperature.

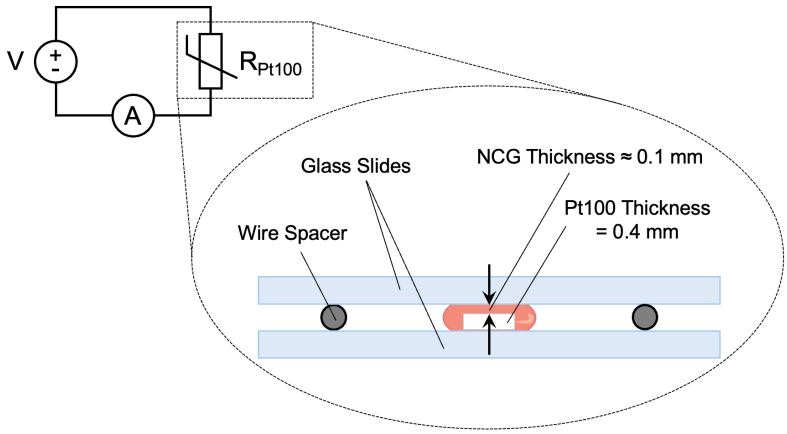


Figure 5.1: Schematic of experimental setup and measurement circuit for determining thermal resistance, R_{th}.

The hA of the reported gel system was obtained experimentally by (5.5) and found to be 0.0198 ± 0.0014 W/°C. This method removes the effects of laser irradiation and plasmon decay and thus quantifies the intrinsic thermal conductance of the system.

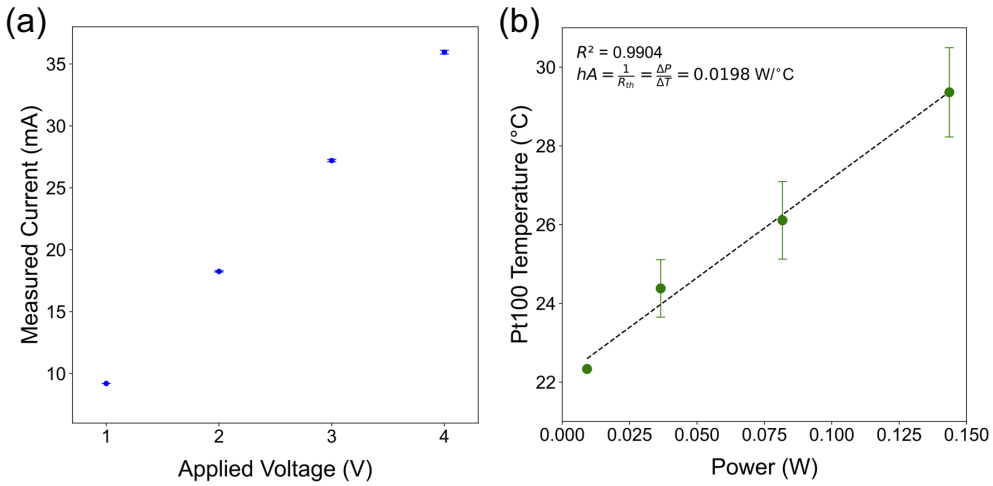


Figure 5.2: Determination of thermal conductance, hA, which is the inverse of thermal resistance, Rth. (a) Measured current as a function of voltage applied to Pt100. Measurements were taken after 30 s of self-heating. (b) The inverse of the slope of the Pt100 power-temperature relationship gives hA (n = 4, reported as mean ± SD).

5.5 Power Contribution of Gel Media and Glass (Q_0)

Table 5.1 reports the Q_0 values unique to each control group, which were calculated using (5.2) and the previously obtained value for hA. Reports of Q_0 for GNR solutions range from 0.05 mW–31.04 mW [63, 64, 65, 70]. Q_0 values for the proposed method (ranging from 0.457 W–0.467 W) are notably larger than those previously reported. Since Q_0 is entirely dependent on the setup geometry, materials, laser power, and control gel formulation, it is expected to differ across studies.

Table 5.1: Estimated Q_0 values using developed control gel biosolders.

GNR Concentration (nM)	**GG Concentration** (% w/v)	$\boldsymbol{Q_0}$ (W) $n = 5$ Mean ± SD
0.0	0.00	0.462 ± 0.033
	0.10	0.467 ± 0.033
	0.25	0.457 ± 0.032

In previous literature, the method for calculating Q_0 involved non-linear fitting of temperature data using a variant of (5.1) [69], though typically, vague or absent descriptions for the estimation method of Q_0 are given [63, 64, 65, 70]. Some have even omitted Q_0 as a power contributor entirely [66, 67, 113]. By examining the definition of η in (5.4), with the Q_0 term in (5.2) re-introduced, it is clear that a larger Q_0 value decreases the calculated value of η. Since Q_0 has been shown to be non-negligible here and by several others, it is therefore imperative that its contribution is considered to prevent the overestimation of η.

For the reported setup, Q_0 was fairly consistent irrespective of the HA:GG ratio (Table 5.1), suggesting that, for insulating polymers such as HA and GG, it is the total polymer content that dictates the heat dissipation of the gel medium, rather than the relative amounts of constituent polymers.

5.6 Determination of η for Developed Biosolders

The photothermal conversion efficiency, η, was used as a metric to directly compare the heating ability of the six GNR-containing gel formulations. Gels with GNR concentrations of 0.7 nM and 1.4 nM with GG concentrations of 0% w/v, 0.10% w/v, and 0.25% w/v were analyzed. Three remaining control gels formulations (GG concentrations of 0% w/v, 0.10% w/v, and 0.25% w/v) were used for Q_0 determination. To determine η for each formulation, the following variable quantities were inputted into (5.4): hA = 0.0198 W/°C, I_0 = 2.4 W, and $A_{\lambda=808\text{ nm}}$ = 0.083, 0.890, or 1.700 for 0 nM, 0.7 nM, and 1.4 nM GNR solutions in 1X PBS, respectively. The corresponding uncertainties in these A_λ values are 0.0142, 0.0175, and 0.0315, respectively, as determined by (A.9) in Appendix Section A.3. The values for ΔT_{GNR} and ΔT_{CTRL} were obtained from steady-state temperature curves (examples were the stability curves presented in Section 3.3).

Fig. 5.3 shows the determined values of η for the tested GNR and GG combinations. The uncertainty of η was estimated by standard uncertainty propagation methods. GG concentration and η correlate strongly for 0.7 nM and 1.4 nM GNR concentration groups (R^2 = 0.9997 and R^2 = 0.985, respectively). For samples containing 0.7 nM GNRs, increasing the GG concentration from 0.0 to 0.25% w/v increased η by $\approx$ 5.28%. Similarly, for samples containing 1.4 nM GNRs, a $\approx$ 6.23% increase in η was observed for the same addition of GG. This positive correlation further confirms the existence of a gum stabilization effect on dispersed GNRs, resulting in improved light-to-heat transduction. Doubling the GNR concentration to 1.4 nM was also found

to improve η. As such, NCG samples with 1.4 nM GNRs and 0.25% w/v GG were found to possess the highest photothermal conversion efficiency (10.01% $\pm$ 0.75%), among those tested.

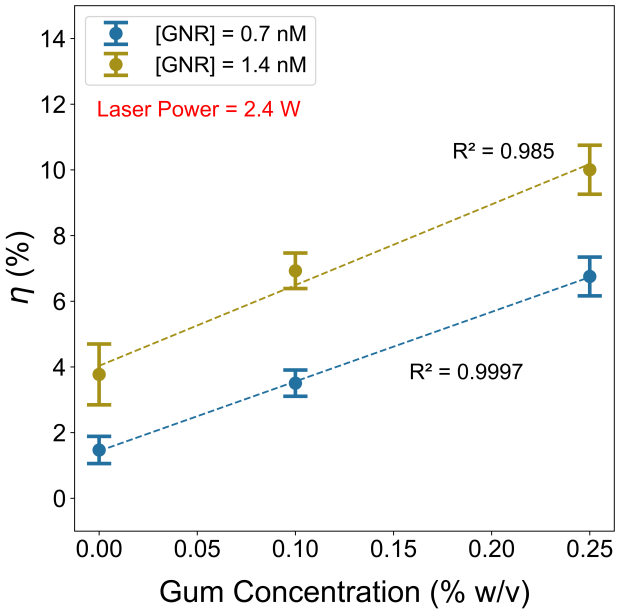


Figure 5.3: Photothermal conversion efficiencies for all GNR-containing NCG groups (n = 5).

Supposing that a photothermal conversion efficiency of roughly 7% is desired for formulation optimization, there are two of the six tested NCG formulations that meet this criterion (see Fig. 2). The formulations containing (0.7 nM GNRs, 0.25% w/v GG) and (1.4 nM GNRs, 0.10% w/v) possess η values of 6.76% $\pm$ 0.59% and 6.93 $\pm$ 0.54%, respectively. It is clear that by simply increasing the GG concentration by 0.15% w/v, half the GNR concentration can be used to achieve a similar level of heating. These findings have implications for reduced nanomaterial exposure to a patient, as well as reduced cost of GNR precursor materials. Depending on the intended application of the NCG, this method can be reiterated with intermediate GNR concentrations to determine the most suitable formulation that minimizes GNR concentration while maintaining a desired η or level of heating.

A caveat to the proposed η determination method is that it is valid only when T_{max} is extracted at true steady state. In the present study, steady state was achieved in $<$30 s. However, for slow-response NCGs, an extensive amount of time—in some cases $>$15 min [66, 67, 69]—may be required, so it is important that T_{max} is not extracted prematurely in these cases. Furthermore,

η is strictly a metric for optimizing NCG formulations where the objective is to minimize GNR concentration for a given level of heating. To evaluate if an NCG can successfully perform its intended application, η on its own is not sufficient and additional testing with *in vitro*, *ex vivo*, or *in vivo* models should be carried out.

The advantage of the proposed method is that it does not require the use of non-linear fittings, time constant calculations or assumptions about effective mass. Only the quantities for thermal conductance, temperature, laser power and absorbance are needed, which can all be determined using the simple methods presently described. Despite its merits, the reported method assumes that resistive heating and laser heating are similar within this system. Future work to validate this assumption is therefore needed.

5.7 Summary

Compared to previous accounts, the proposed alternative method for the determination of η is simple, yet robust. This is the first attempt to standardize the determination of η for viscous photothermal materials, such as NCGs, and it is also the first reported method of calculating η through direct determination of thermal conductance, hA.

Chapter 6

Conclusions and Future Work

6.1 Conclusions

The custom characterization system presented here was, to my knowledge, the first system designed specifically for evaluating the photothermal performance of highly viscous NCGs at micron-scale thicknesses. The described photothermal characterization schemes are proposed as preliminary "screening" characterizations when designing photothermal NCGs. I.e., these schemes are meant to be a useful framework to assess the readiness of a biosolder formulation for future administration to tissue models. This can improve precision and speed for the testing of biosolder materials. As well, the reported method is not exclusive to NCGs containing metallic nanoparticles, as it can be extended to other photothermal materials, such as semisolids containing organic chromophores, semiconductors, carbon materials or hybrid materials thereof. Moreover, it may be suitable for testing certain liquid formulations given that they possess a viscosity high enough to discourage sample outflow and/or appropriate surface modification of the glass contacts is performed to encourage sample wettability.

It is important to acknowledge the limitations of the presented work. To start, the determination of η with the reported characterization system relied on the assumption that laser heating and RTD self-heating are similar. This assumption was not validated here and it is recommended to do so in future work. As well, the laser alignment overhead the Pt100 is currently adjusted manually and semi-frequently between sample loadings. As the Pt100 temperature is directly affected by laser positioning, this step may be subject to operator variability. Furthermore and most significantly, the presented work is only capable of evaluating the thermal aspect of clinical relevance of NCGs in isolation. It is therefore necessary to evaluate the biologically relevant aspects of clinical readiness with tissue models and biocompatibility testing for a complete picture.

6.2 Future Work

More work is needed to show clinical success for improved wound closure and healing using laser tissue welding with the presented biosolder materials.

6.2.1 *Ex vivo* or *in vivo* Validation of the Design Metric, ξ

To corroborate the results reported in Section 4.2.2, additional studies in *in vivo* (living) and *ex vivo* (excised, non-living) tissue models can be performed involving *in situ* temperature measurements and the visual monitoring of thermal damage events during and immediately after the LTW procedure. In clinical settings, the upper glass contact in the reported characterization setup would be absent, resulting in higher temperatures for a given laser power. Additional investigations can be carried out to recommend a reduced laser power during practical application. It is further important to appreciate the differences between *in vivo* joining and *ex vivo* joining. A living model possesses the active biological machinery for wound healing after the LTW process has terminated, therefore providing improved bond strength of the closed wound.

6.2.2 *Ex vivo* or *in vivo* Welding with Developed Biosolders

The ultimate goal is to create successful welds in tissue models using the developed biosolder. *Ex vivo* or *in vivo* tissue models can be used to create welds, followed by tensile testing or burst pressure testing of the welded tissues. Histological experiments can also be performed on welded tissues to gauge extent of thermal damage. These are all suggested to quantify biosolder formulation efficacy, as described by [9, 10, 33].

6.2.3 Gel Shelf-Life Testing

Currently, the biosolder gels are stored at ambient temperatures and tested within 1-3 days. As the gel is a proposed medical product, its long-term storage and stability should be assessed. This can involve a simple test of heating performance (ΔT), repeated daily or similar, using the photothermal characterization setup described in Chapter 3. It is expected that ΔT degrades over time for a given gel batch. The rate at which heating performance degrades can be modeled and samples can be deemed "unusable" after a threshold decline in ΔT is met. During such a study, other storage solutions (e.g., refrigeration) can be assessed concurrently.

6.2.4 Cytotoxicity Testing

To further strengthen the case for clinical relevance, the developed biosolder samples can be tested for cytotoxicity as an indicator for potential biocompatibility. To achieve this, an MTT assay can be performed on human (or other) fibroblast cells—the cells responsible for secretion of the non-rigid ECM in connective tissue [114]. The MTT (3-[4,5-dimethylthiazol-2-yl]-2,5 diphenyl tetrazolium bromide) assay is a colourimetric assay that is popularly used for evaluating the cytotoxicity of a substance [115]. Living cells are able to convert MTT into formazan crystals by mitochondrial metabolic pathways; the concentration of this product can be measured by UV-vis spectroscopy to determine cell viability [115].

6.2.5 Laser Heating and RTD-Self Heating

As previously mentioned, the method for determining η assumed equality between laser heating and RTD self-heating. Further comparisons between the setup thermal resistance under these differing conditions can be carried out to validate this assumption.

6.2.6 Handheld Laser Design

The presented photothermal characterization setup is a fixed benchtop apparatus. To better emulate clinical usage, the next generation of this characterization system can replace the fixed laser (which only possesses freedom in the z-direction) with a handheld laser, much like a pen. Preliminary work has commenced towards this (Fig. 6.1). To aid in LTW, the handheld device can include built-in forceps or tweezers to appose wound edges during lasing.

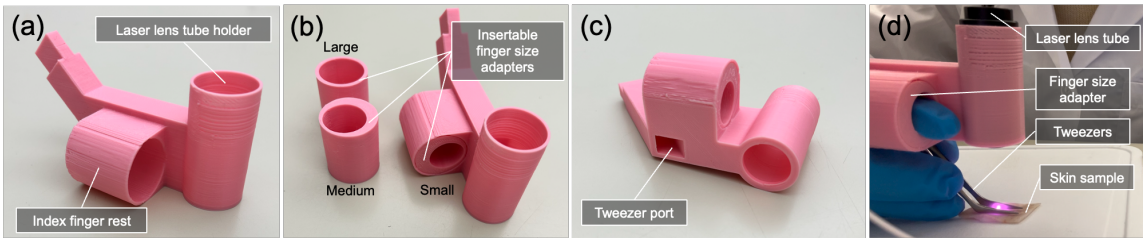


Figure 6.1: First prototype of a handheld laser case with built-in tweezers. (a) Photograph of the case, (b) Different-sized finger adapters for small, medium and large hands, (c) Location for inserting tweezers at bottom of case; the tweezers snap in place, (d) Device application to a porcine skin sample.

Copyright Permission

ELSEVIER LICENSE
TERMS AND CONDITIONS

Feb 26, 2025

This Agreement between Michelle Dieu Thao Huynh ("You") and Elsevier ("Elsevier") consists of your license details and the terms and conditions provided by Elsevier and Copyright Clearance Center.

License Number	5976800870030
License date	Feb 26, 2025
Licensed Content Publisher	Elsevier
Licensed Content Publication	NeuroImage
Licensed Content Title	A review on continuous wave functional near-infrared spectroscopy and imaging instrumentation and methodology
Licensed Content Author	Felix Scholkmann,Stefan Kleiser,Andreas Jaakko Metz,Raphael Zimmermann,Juan Mata Pavia,Ursula Wolf,Martin Wolf
Licensed Content Date	Jan 15, 2014
Licensed Content Volume	85
Licensed Content Issue	n/a
Licensed Content Pages	22
Start Page	6
End Page	27

Type of Use	reuse in a thesis/dissertation
Portion	figures/tables/illustrations
Number of figures/tables/illustrations	1
Format	both print and electronic
Are you the author of this Elsevier article?	No
Will you be translating?	No
Title of new work	A Characterization Scheme to Assess the Heating Performance of Developed Biological Solders for Laser Tissue Welding
Institution name	University of Waterloo
Expected presentation date	Apr 2025
Portions	Figure 2
The Requesting Person / Organization to Appear on the License	Michelle Dieu Thao Huynh
Requestor Location	Michelle Huynh 330 Phillip Street Waterloo, ON N2L 3W9 Canada
Publisher Tax ID	GB 494 6272 12
Total	0.00 CAD
Terms and Conditions	

INTRODUCTION

1. The publisher for this copyrighted material is Elsevier. By clicking "accept" in connection with completing this licensing transaction, you agree that the following terms and conditions apply to this transaction (along with the Billing and Payment terms and conditions established by Copyright Clearance Center, Inc. ("CCC"), at the time that you opened your RightsLink account and that are available at any time at https://myaccount.copyright.com).

GENERAL TERMS

2. Elsevier hereby grants you permission to reproduce the aforementioned material subject to the terms and conditions indicated.

3. Acknowledgement: If any part of the material to be used (for example, figures) has appeared in our publication with credit or acknowledgement to another source, permission must also be sought from that source. If such permission is not obtained then that material may not be included in your publication/copies. Suitable acknowledgement to the source must be made, either as a footnote or in a reference list at the end of your publication, as follows:

"Reprinted from Publication title, Vol /edition number, Author(s), Title of article / title of chapter, Pages No., Copyright (Year), with permission from Elsevier [OR APPLICABLE SOCIETY COPYRIGHT OWNER]." Also Lancet special credit - "Reprinted from The Lancet, Vol. number, Author(s), Title of article, Pages No., Copyright (Year), with permission from Elsevier."

4. Reproduction of this material is confined to the purpose and/or media for which permission is hereby given. The material may not be reproduced or used in any other way, including use in combination with an artificial intelligence tool (including to train an algorithm, test, process, analyse, generate output and/or develop any form of artificial intelligence tool), or to create any derivative work and/or service (including resulting from the use of artificial intelligence tools).

5. Altering/Modifying Material: Not Permitted. However figures and illustrations may be altered/adapted minimally to serve your work. Any other abbreviations, additions, deletions and/or any other alterations shall be made only with prior written authorization of Elsevier Ltd. (Please contact Elsevier's permissions helpdesk here). No modifications can be made to any Lancet figures/tables and they must be reproduced in full.

6. If the permission fee for the requested use of our material is waived in this instance, please be advised that your future requests for Elsevier materials may attract a fee.

7. Reservation of Rights: Publisher reserves all rights not specifically granted in the combination of (i) the license details provided by you and accepted in the course of this licensing transaction, (ii) these terms and conditions and (iii) CCC's Billing and Payment terms and conditions.

8. License Contingent Upon Payment: While you may exercise the rights licensed immediately upon issuance of the license at the end of the licensing process for the transaction, provided that you have disclosed complete and accurate details of your proposed use, no license is finally effective unless and until full payment is received from you (either by publisher or by CCC) as provided in CCC's Billing and Payment terms and conditions. If full payment is not received on a timely basis, then any license

preliminarily granted shall be deemed automatically revoked and shall be void as if never granted. Further, in the event that you breach any of these terms and conditions or any of CCC's Billing and Payment terms and conditions, the license is automatically revoked and shall be void as if never granted. Use of materials as described in a revoked license, as well as any use of the materials beyond the scope of an unrevoked license, may constitute copyright infringement and publisher reserves the right to take any and all action to protect its copyright in the materials.

9. Warranties: Publisher makes no representations or warranties with respect to the licensed material.

10. Indemnity: You hereby indemnify and agree to hold harmless publisher and CCC, and their respective officers, directors, employees and agents, from and against any and all claims arising out of your use of the licensed material other than as specifically authorized pursuant to this license.

11. No Transfer of License: This license is personal to you and may not be sublicensed, assigned, or transferred by you to any other person without publisher's written permission.

12. No Amendment Except in Writing: This license may not be amended except in a writing signed by both parties (or, in the case of publisher, by CCC on publisher's behalf).

13. Objection to Contrary Terms: Publisher hereby objects to any terms contained in any purchase order, acknowledgment, check endorsement or other writing prepared by you, which terms are inconsistent with these terms and conditions or CCC's Billing and Payment terms and conditions. These terms and conditions, together with CCC's Billing and Payment terms and conditions (which are incorporated herein), comprise the entire agreement between you and publisher (and CCC) concerning this licensing transaction. In the event of any conflict between your obligations established by these terms and conditions and those established by CCC's Billing and Payment terms and conditions, these terms and conditions shall control.

14. Revocation: Elsevier or Copyright Clearance Center may deny the permissions described in this License at their sole discretion, for any reason or no reason, with a full refund payable to you. Notice of such denial will be made using the contact information provided by you. Failure to receive such notice will not alter or invalidate the denial. In no event will Elsevier or Copyright Clearance Center be responsible or liable for any costs, expenses or damage incurred by you as a result of a denial of your permission request, other than a refund of the amount(s) paid by you to Elsevier and/or Copyright Clearance Center for denied permissions.

LIMITED LICENSE

The following terms and conditions apply only to specific license types:

15. **Translation**: This permission is granted for non-exclusive world **English** rights only unless your license was granted for translation rights. If you licensed translation rights you may only translate this content into the languages you requested. A professional translator must perform all translations and reproduce the content word for word preserving the integrity of the article.

16. **Posting licensed content on any Website**: The following terms and conditions apply as follows: Licensing material from an Elsevier journal: All content posted to the web site must maintain the copyright information line on the bottom of each image; A hyper-text must be included to the Homepage of the journal from which you are licensing at

http://www.sciencedirect.com/science/journal/xxxxx or the Elsevier homepage for books at http://www.elsevier.com; Central Storage: This license does not include permission for a scanned version of the material to be stored in a central repository such as that provided by Heron/XanEdu.

Licensing material from an Elsevier book: A hyper-text link must be included to the Elsevier homepage at http://www.elsevier.com . All content posted to the web site must maintain the copyright information line on the bottom of each image.

Posting licensed content on Electronic reserve: In addition to the above the following clauses are applicable: The web site must be password-protected and made available only to bona fide students registered on a relevant course. This permission is granted for 1 year only. You may obtain a new license for future website posting.

17. **For journal authors:** the following clauses are applicable in addition to the above:

Preprints:

A preprint is an author's own write-up of research results and analysis, it has not been peer-reviewed, nor has it had any other value added to it by a publisher (such as formatting, copyright, technical enhancement etc.).

Authors can share their preprints anywhere at any time. Preprints should not be added to or enhanced in any way in order to appear more like, or to substitute for, the final versions of articles however authors can update their preprints on arXiv or RePEc with their Accepted Author Manuscript (see below).

If accepted for publication, we encourage authors to link from the preprint to their formal publication via its DOI. Millions of researchers have access to the formal publications on ScienceDirect, and so links will help users to find, access, cite and use the best available version. Please note that Cell Press, The Lancet and some society-owned have different preprint policies. Information on these policies is available on the journal homepage.

Accepted Author Manuscripts: An accepted author manuscript is the manuscript of an article that has been accepted for publication and which typically includes author-incorporated changes suggested during submission, peer review and editor-author communications.

Authors can share their accepted author manuscript:

- immediately
  - via their non-commercial person homepage or blog
  - by updating a preprint in arXiv or RePEc with the accepted manuscript
  - via their research institute or institutional repository for internal institutional uses or as part of an invitation-only research collaboration work-group
  - directly by providing copies to their students or to research collaborators for their personal use
  - for private scholarly sharing as part of an invitation-only work group on commercial sites with which Elsevier has an agreement
- After the embargo period
  - via non-commercial hosting platforms such as their institutional repository
  - via commercial sites with which Elsevier has an agreement

In all cases accepted manuscripts should:

- link to the formal publication via its DOI
- bear a CC-BY-NC-ND license - this is easy to do
- if aggregated with other manuscripts, for example in a repository or other site, be shared in alignment with our hosting policy not be added to or enhanced in any way to appear more like, or to substitute for, the published journal article.

Published journal article (JPA): A published journal article (PJA) is the definitive final record of published research that appears or will appear in the journal and embodies all value-adding publishing activities including peer review co-ordination, copy-editing, formatting, (if relevant) pagination and online enrichment.

Policies for sharing publishing journal articles differ for subscription and gold open access articles:

Subscription Articles: If you are an author, please share a link to your article rather than the full-text. Millions of researchers have access to the formal publications on ScienceDirect, and so links will help your users to find, access, cite, and use the best available version.

Theses and dissertations which contain embedded PJAs as part of the formal submission can be posted publicly by the awarding institution with DOI links back to the formal publications on ScienceDirect.

If you are affiliated with a library that subscribes to ScienceDirect you have additional private sharing rights for others' research accessed under that agreement. This includes use for classroom teaching and internal training at the institution (including use in course packs and courseware programs), and inclusion of the article for grant funding purposes.

Gold Open Access Articles: May be shared according to the author-selected end-user license and should contain a CrossMark logo, the end user license, and a DOI link to the formal publication on ScienceDirect.

Please refer to Elsevier's posting policy for further information.

18. **For book authors** the following clauses are applicable in addition to the above: Authors are permitted to place a brief summary of their work online only. You are not allowed to download and post the published electronic version of your chapter, nor may you scan the printed edition to create an electronic version. **Posting to a repository:** Authors are permitted to post a summary of their chapter only in their institution's repository.

19. **Thesis/Dissertation**: If your license is for use in a thesis/dissertation your thesis may be submitted to your institution in either print or electronic form. Should your thesis be published commercially, please reapply for permission. These requirements include permission for the Library and Archives of Canada to supply single copies, on demand, of the complete thesis and include permission for Proquest/UMI to supply single copies, on demand, of the complete thesis. Should your thesis be published commercially, please reapply for permission. Theses and dissertations which contain embedded PJAs as part of the formal submission can be posted publicly by the awarding institution with DOI links back to the formal publications on ScienceDirect.

Elsevier Open Access Terms and Conditions

You can publish open access with Elsevier in hundreds of open access journals or in nearly 2000 established subscription journals that support open access publishing. Permitted third party re-use of these open access articles is defined by the author's choice of Creative Commons user license. See our open access license policy for more information.

Terms & Conditions applicable to all Open Access articles published with Elsevier:

Any reuse of the article must not represent the author as endorsing the adaptation of the article nor should the article be modified in such a way as to damage the author's honour or reputation. If any changes have been made, such changes must be clearly indicated.

The author(s) must be appropriately credited and we ask that you include the end user license and a DOI link to the formal publication on ScienceDirect.

If any part of the material to be used (for example, figures) has appeared in our publication with credit or acknowledgement to another source it is the responsibility of the user to ensure their reuse complies with the terms and conditions determined by the rights holder.

Additional Terms & Conditions applicable to each Creative Commons user license:

CC BY: The CC-BY license allows users to copy, to create extracts, abstracts and new works from the Article, to alter and revise the Article and to make commercial use of the Article (including reuse and/or resale of the Article by commercial entities), provided the user gives appropriate credit (with a link to the formal publication through the relevant DOI), provides a link to the license, indicates if changes were made and the licensor is not represented as endorsing the use made of the work. The full details of the license are available at http://creativecommons.org/licenses/by/4.0.

CC BY NC SA: The CC BY-NC-SA license allows users to copy, to create extracts, abstracts and new works from the Article, to alter and revise the Article, provided this is not done for commercial purposes, and that the user gives appropriate credit (with a link to the formal publication through the relevant DOI), provides a link to the license, indicates if changes were made and the licensor is not represented as endorsing the use made of the work. Further, any new works must be made available on the same conditions. The full details of the license are available at http://creativecommons.org/licenses/by-nc-sa/4.0.

CC BY NC ND: The CC BY-NC-ND license allows users to copy and distribute the Article, provided this is not done for commercial purposes and further does not permit distribution of the Article if it is changed or edited in any way, and provided the user gives appropriate credit (with a link to the formal publication through the relevant DOI), provides a link to the license, and that the licensor is not represented as endorsing the use made of the work. The full details of the license are available at http://creativecommons.org/licenses/by-nc-nd/4.0. Any commercial reuse of Open Access articles published with a CC BY NC SA or CC BY NC ND license requires permission from Elsevier and will be subject to a fee.

Commercial reuse includes:

- Associating advertising with the full text of the Article
- Charging fees for document delivery or access
- Article aggregation
- Systematic distribution via e-mail lists or share buttons

Posting or linking by commercial companies for use by customers of those companies.

20. **Other Conditions**:

v1.10

Questions? customercare@copyright.com.

References

[1] K. Mastud, Y. Lamture, T. Nagtode, and V. Rewale, "A comparative study between conventional sutures, staples, and adhesive glue for clean elective surgical skin closure."

[2] A. Q. Amini, N. A. Khan, J. Ahmad, and A. S. Memon, "Management of abdominal wound dehiscence: still a challenge."

[3] R. L. Smith, J. K. Bohl, S. T. McElearney, C. M. Friel, M. M. Barclay, R. G. Sawyer, and E. F. Foley, "Wound infection after elective colorectal resection," vol. 239, no. 5, pp. 599–607. [Online]. Available: https://www.ncbi.nlm.nih.gov/pmc/articles/PMC1356267/

[4] E. Maurer, A. Reuss, K. Maschuw, B. Aminossadati, T. Neubert, C. Schade-Brittinger, and D. K. Bartsch, "Superficial surgical site infection following the use of intracutaneous sutures versus staples," vol. 116, no. 21, pp. 365–371. [Online]. Available: https://www.ncbi.nlm.nih.gov/pmc/articles/PMC6647811/

[5] U. K. Ercan, F. İbiş, C. Dikyol, N. Horzum, O. Karaman, Yıldırım, E. Çukur, and E. A. Demirci, "Prevention of bacterial colonization on non-thermal atmospheric plasma treated surgical sutures for control and prevention of surgical site infections," vol. 13, no. 9, p. e0202703. [Online]. Available: https://www.ncbi.nlm.nih.gov/pmc/articles/PMC6124751/

[6] B. S. Bleier, N. M. Cohen, J. D. Bloom, J. N. Palmer, and N. A. Cohen, "Laser tissue welding in lung and tracheobronchial repair: an animal model," vol. 138, no. 2, pp. 345–349.

[7] R. T. Poon, "Current techniques of liver transection," vol. 9, no. 3, pp. 166–173. [Online]. Available: https://linkinghub.elsevier.com/retrieve/pii/S1365182X15310406

[8] K. K. Jain and W. Gorisch, "Repair of small blood vessels with the neodymium-YAG laser: a preliminary report," vol. 85, no. 6, pp. 684–688.

[9] R. Urie, S. Quraishi, M. Jaffe, and K. Rege, "Gold nanorod-collagen nanocomposites as photothermal nanosolders for laser welding of ruptured porcine intestines," vol. 1, no. 9, pp. 805–815. [Online]. Available: https://pubs.acs.org/doi/10.1021/acsbiomaterials.5b00174

[10] H.-C. Huang, C. R. Walker, A. Nanda, and K. Rege, "Laser welding of ruptured intestinal tissue using plasmonic polypeptide nanocomposite solders," vol. 7, no. 4, pp. 2988–2998. [Online]. Available: https://pubs.acs.org/doi/10.1021/nn303202k

[11] Y. Mistry, S. Natarajan, and S. Ahuja, "Evaluation of laser tissue welding and laser-tissue soldering for mucosal and vascular repair," vol. 8, no. 1, p. 35. [Online]. Available: https://journals.lww.com/10.4103/ams.ams_147_17

[12] M. Schiavon, G. Marulli, A. Zuin, F. Lunardi, P. Villoresi, S. Bonora, F. Calabrese, and F. Rea, "Experimental evaluation of a new system for laser tissue welding applied on damaged lungs," vol. 16, no. 5, pp. 577–582. [Online]. Available: https://academic.oup.com/icvts/article-lookup/doi/10.1093/icvts/ivt029

[13] R. Urie, C. Guo, D. Ghosh, M. Thelakkaden, V. Wong, J. K. Lee, J. Kilbourne, J. Yarger, and K. Rege, "Rapid soft tissue approximation and repair using laser-activated silk nanosealants," vol. 28, no. 42, p. 1802874, _eprint: https://onlinelibrary.wiley.com/doi/pdf/10.1002/adfm.201802874. [Online]. Available: https://onlinelibrary.wiley.com/doi/abs/10.1002/adfm.201802874

[14] I. Çilesiz, T. Springer, S. Thomsen, and A. Welch, "Controlled temperature tissue fusion: Argon laser welding of canine intestine in vitro," vol. 18, no. 4, pp. 325–334, _eprint: https://onlinelibrary.wiley.com/doi/pdf/10.1002/%28SICI%291096-9101%281996%2918%3A4%3C325%3A%3AAID-LSM1%3E3.0.CO%3B2-U. [Online]. Available: https://onlinelibrary.wiley.com/doi/abs/10.1002/%28SICI%291096-9101%281996%2918%3A4%3C325%3A%3AAID-LSM1%3E3.0.CO%3B2-U

[15] D. P. Poppas, R. B. Stewart, J. M. Massicotte, A. E. Wolga, R. T. Kung, A. B. Retik, and M. R. Freeman, "Temperature-controlled laser photocoagulation of soft tissue: In vivo evaluation using a tissue welding model," vol. 18, no. 4, pp. 335–344, _eprint: https://onlinelibrary.wiley.com/doi/pdf/10.1002/%28SICI%291096-9101%281996%2918%3A4%3C335%3A%3AAID-LSM2%3E3.0.CO%3B2-T. [Online]. Available: https://onlinelibrary.wiley.com/doi/abs/10.1002/%28SICI%291096-9101%281996%2918%3A4%3C335%3A%3AAID-LSM2%3E3.0.CO%3B2-T

[16] G. Esposito, F. Rossi, A. Puca, A. Albanese, G. Sabatino, P. Matteini, G. Lofrese, G. Maira, and R. Pini, "An experimental study on minimally occlusive laser-assisted vascular anastomosis in bypass surgery: the importance of temperature monitoring during laser welding procedures," vol. 24, no. 3, pp. 307–315.

[17] G. Esposito, F. Rossi, P. Matteini, F. Ratto, G. Sabatino, A. Puca, A. Albanese, G. Rossi, E. Marchese, G. Maira, and R. Pini, "Nanotechnology and vascular neurosurgery: An in vivo experimental study on microvessels repair using laser photoactivation of a nanostructured hyaluronan solder," vol. 26, no. 3.

[18] M. Watford and G. Wu, "Protein," vol. 9, no. 5, pp. 651–653. [Online]. Available: https://www.ncbi.nlm.nih.gov/pmc/articles/PMC6140426/

[19] D. Kishore, S. Kundu, and A. M. Kayastha, "Thermal, chemical and pH induced denaturation of a multimeric -galactosidase reveals multiple unfolding pathways," vol. 7, no. 11, p. e50380. [Online]. Available: https://www.ncbi.nlm.nih.gov/pmc/articles/PMC3503960/

[20] L. J. Lapidus, "Protein unfolding mechanisms and their effects on folding experiments," vol. 6, p. 1723. [Online]. Available: https://f1000research.com/articles/6-1723/v1

[21] E. M. Culav, C. H. Clark, and M. J. Merrilees, "Connective tissues: Matrix composition and its relevance to physical therapy," vol. 79, no. 3, pp. 308–319. [Online]. Available: https://doi.org/10.1093/ptj/79.3.308

[22] M. Shenoy, N. S. Abdul, Z. Qamar, B. M. A. Bahri, K. Z. K. Al Ghalayini, and A. Kakti, "Collagen structure, synthesis, and its applications: A systematic review," vol. 14, no. 5, p. e24856. [Online]. Available: https://www.ncbi.nlm.nih.gov/pmc/articles/PMC9177216/

[23] M. D. Shoulders and R. T. Raines, "Collagen structure and stability," vol. 78, pp. 929–958. [Online]. Available: https://www.ncbi.nlm.nih.gov/pmc/articles/PMC2846778/

[24] L. Leo, M. G. Bridelli, and E. Polverini, "Insight on collagen self-assembly mechanisms by coupling molecular dynamics and UV spectroscopy techniques," vol. 253, p. 106224. [Online]. Available: https://linkinghub.elsevier.com/retrieve/pii/S0301462219302911

[25] P. N. Lewis, C. Pinali, R. D. Young, K. M. Meek, A. J. Quantock, and C. Knupp, "Structural interactions between collagen and proteoglycans are elucidated by three-dimensional electron tomography of bovine cornea," vol. 18, no. 2, pp. 239–245. [Online]. Available: https://linkinghub.elsevier.com/retrieve/pii/S0969212609004791

[26] Q. T. Smith, "Collagen metabolism in wound healing," in *Trauma: Clinical and Biological Aspects*, S. B. Day, Ed. Springer US, pp. 31–45. [Online]. Available: https://doi.org/10.1007/978-1-4684-2145-3_3

[27] B. Gerdin and R. Hällgren, "Dynamic role of hyaluronan (HYA) in connective tissue activation and inflammation," vol. 242, no. 1, pp. 49–55. [Online]. Available: https://onlinelibrary.wiley.com/doi/10.1046/j.1365-2796.1997.00173.x

[28] J. S. Frenkel, "The role of hyaluronan in wound healing," vol. 11, no. 2, pp. 159–163. [Online]. Available: https://onlinelibrary.wiley.com/doi/10.1111/j.1742-481X.2012.01057.x

[29] F. Ratto, P. Matteini, F. Rossi, L. Menabuoni, N. Tiwari, S. K. Kulkarni, and R. Pini, "Photothermal effects in connective tissues mediated by laser-activated gold nanorods," vol. 5, no. 2, pp. 143–151. [Online]. Available: https://linkinghub.elsevier.com/retrieve/pii/S1549963408001822

[30] I. Ashbell, N. Agam, A. Katzir, S. Basov, M. Platkov, I. Avital, I. Nisky, and U. Netz, "Laser tissue soldering of the gastrointestinal tract: A systematic review," vol. 9, no. 5, p. e16018. [Online]. Available: https://linkinghub.elsevier.com/retrieve/pii/S2405844023032255

[31] T. Velnar, T. Bailey, and V. Smrkolj, "The wound healing process: An overview of the cellular and molecular mechanisms," vol. 37, no. 5, pp. 1528–1542. [Online]. Available: http://journals.sagepub.com/doi/10.1177/147323000903700531

[32] R. K. Manivannan, N. Sharma, V. Kumar, I. Jayaraj, S. Vimal, and M. Umesh, "A comprehensive review on natural macromolecular biopolymers for biomedical applications: Recent advancements, current challenges, and future outlooks," vol. 8, p. 100536. [Online]. Available: https://linkinghub.elsevier.com/retrieve/pii/S2666893924001166

[33] P. Matteini, F. Ratto, F. Rossi, G. Rossi, G. Esposito, A. Puca, A. Albanese, G. Maira, and R. Pini, "In vivo carotid artery closure by laser activation of hyaluronan-embedded gold nanorods," vol. 15, no. 4, p. 041508. [Online]. Available: http://biomedicaloptics.spiedigitallibrary.org/article.aspx?doi=10.1117/1.3449574

[34] K. T. Zhang, "Laser welding of porcine skeletal muscle tissue using near infrared irradiation with gold nanorod biosolders."

[35] I. P. Schwartz, D. D. Suh, D. A. Canning, H. M. Snyder, S. A. Zderic, and A. J. Kirsch, "Optimal solder and power density for diode laser tissue soldering (LTS)."

[36] K. M. McNally, B. S. Sorg, A. J. Welch, J. M. Dawes, and E. R. Owen, "Photothermal effects of laser tissue soldering," vol. 44, no. 4, pp. 983–1002. [Online]. Available: https://iopscience.iop.org/article/10.1088/0031-9155/44/4/013

[37] P. Matteini, F. Ratto, F. Rossi, S. Centi, L. Dei, and R. Pini, "Chitosan films doped with gold nanorods as laser-activatable hybrid bioadhesives," vol. 22, no. 38, pp. 4313–4316, _eprint: https://onlinelibrary.wiley.com/doi/pdf/10.1002/adma.201002228. [Online]. Available: https://onlinelibrary.wiley.com/doi/abs/10.1002/adma.201002228

[38] H. W. Lim, *Clinical Photomedicine*. Routledge.

[39] R. Richards-Kortum and E. Sevick-Muraca, "Quantitative optical spectroscopy for tissue diagnosis," vol. 47, no. 1, pp. 555–606. [Online]. Available: https://www.annualreviews.org/doi/10.1146/annurev.physchem.47.1.555

[40] M. A. Ansari and E. Mohajerani, "Mechanisms of laser-tissue interaction: I. optical properties of tissue," vol. 2, no. 3, p. 8.

[41] F. Scholkmann, S. Kleiser, A. J. Metz, R. Zimmermann, J. Mata Pavia, U. Wolf, and M. Wolf, "A review on continuous wave functional near-infrared spectroscopy and imaging instrumentation and methodology," vol. 85, pp. 6–27. [Online]. Available: https://linkinghub.elsevier.com/retrieve/pii/S1053811913004941

[42] X. Li, G. L. Ferrel, M. C. Guerra, T. Hode, J. A. Lunn, O. Adalsteinsson, R. E. Nordquist, H. Liu, and W. R. Chen, "Preliminary safety and efficacy results of laser immunotherapy for the treatment of metastatic breast cancer patients," vol. 10, no. 5, pp. 817–821. [Online]. Available: https://link.springer.com/10.1039/c0pp00306a

[43] M. C. Oz, J. P. Johnson, S. Parangi, R. S. Chuck, C. C. Marboe, L. S. Bass, R. Nowygrod, and M. R. Treat, "Tissue soldering by use of indocyanine green dye-enhanced fibrinogen with the near infrared diode laser," vol. 11, no. 5, pp. 718–725, publisher: Elsevier. [Online]. Available: https://www.jvascsurg.org/article/0741-5214(90)90219-Z/fulltext

[44] J. Zheng, X. Cheng, H. Zhang, X. Bai, R. Ai, L. Shao, and J. Wang, "Gold nanorods: The most versatile plasmonic nanoparticles," vol. 121, no. 21, pp. 13 342–13 453. [Online]. Available: https://pubs.acs.org/doi/10.1021/acs.chemrev.1c00422

[45] P. K. Jain, X. Huang, I. H. El-Sayed, and M. A. El-Sayed, "Noble metals on the nanoscale: Optical and photothermal properties and some applications in imaging, sensing, biology, and medicine," vol. 41, no. 12, pp. 1578–1586. [Online]. Available: https://pubs.acs.org/doi/10.1021/ar7002804

[46] X. Kang, X. Guo, X. Niu, W. An, S. Li, Z. Liu, Y. Yang, N. Wang, Q. Jiang, C. Yan, H. Wang, and Q. Zhang, "Photothermal therapeutic application of gold nanorods-porphyrin-trastuzumab complexes in HER2-positive breast cancer," vol. 7, no. 1, p. 42069. [Online]. Available: http://www.nature.com/articles/srep42069

[47] F. Meng and A. I. Alayash, "Determination of extinction coefficients of human hemoglobin in various redox states," vol. 521, pp. 11–19. [Online]. Available: https://europepmc.org/articles/PMC5303181

[48] A. Woźniak, A. Malankowska, G. Nowaczyk, B. F. Grześkowiak, K. Tuśnio, R. Słomski, A. Zaleska-Medynska, and S. Jurga, "Size and shape-dependent cytotoxicity profile of gold nanoparticles for biomedical applications," vol. 28, no. 6, p. 92. [Online]. Available: http://link.springer.com/10.1007/s10856-017-5902-y

[49] S. Link, M. B. Mohamed, and M. A. El-Sayed, "Simulation of the optical absorption spectra of gold nanorods as a function of their aspect ratio and the effect of the medium dielectric constant," vol. 103, no. 16, pp. 3073–3077. [Online]. Available: https://pubs.acs.org/doi/10.1021/jp990183f

[50] B. Nikoobakht and M. A. El-Sayed, "Preparation and growth mechanism of gold nanorods (NRs) using seed-mediated growth method," vol. 15, no. 10, pp. 1957–1962. [Online]. Available: https://pubs.acs.org/doi/10.1021/cm0207321

[51] L. Scarabelli, A. Sánchez-Iglesias, J. Pérez-Juste, and L. M. Liz-Marzán, "A "tips and tricks" practical guide to the synthesis of gold nanorods," vol. 6, no. 21, pp. 4270–4279, publisher: American Chemical Society. [Online]. Available: https://doi.org/10.1021/acs.jpclett.5b02123

[52] Z. Zhang and M. Lin, "Fast loading of PEG–SH on CTAB-protected gold nanorods," vol. 4, no. 34, p. 17760. [Online]. Available: http://xlink.rsc.org/?DOI=c3ra48061e

[53] Y. Zengin, D. Kelle, and B. Iyisan, "Design of biopolymer-coated gold nanorods as biorelevant photothermal agents," p. 2400497. [Online]. Available: https://onlinelibrary.wiley.com/doi/10.1002/marc.202400497

[54] J. P. Gonçalves, A. F. Da Cruz, M. Nunes, M. R. Meneghetti, H. R. De Barros, B. S. Borges, L. C. De Medeiros, M. J. Soares, M. P. Dos Santos, M. T. Grassi, G. R. Rossi, D. L. Bellan, S. M. Biscaia, A. M. Cristal, J. L. Buzzo, Y. C. Ribeiro, A. Acco, M. B. Cardoso, F. F. Simas, E. S. Trindade, I. C. Riegel-Vidotti, and C. C. De Oliveira, "Biocompatible gum arabic-gold nanorod composite as an effective therapy for mistreated melanomas," vol. 185, pp. 551–561. [Online]. Available: https://linkinghub.elsevier.com/retrieve/pii/S014181302101401X

[55] D. Pooja, S. Panyaram, H. Kulhari, S. S. Rachamalla, and R. Sistla, "Xanthan gum stabilized gold nanoparticles: Characterization, biocompatibility, stability and cytotoxicity," vol. 110, pp. 1–9. [Online]. Available: https://www.sciencedirect.com/science/article/pii/S0144861714002732

[56] S. Vieira, S. Vial, F. R. Maia, M. Carvalho, R. L. Reis, P. L. Granja, and J. M. Oliveira, "Gellan gum-coated gold nanorods: an intracellular nanosystem for bone tissue engineering," vol. 5, no. 95, pp. 77 996–78 005. [Online]. Available: https://xlink.rsc.org/?DOI=C5RA13556G

[57] D. Verma and S. K. Sharma, "Recent advances in guar gum based drug delivery systems and their administrative routes," vol. 181, pp. 653–671. [Online]. Available: https://linkinghub.elsevier.com/retrieve/pii/S014181302100605X

[58] B. B. Karakocak, J. Liang, P. Biswas, and N. Ravi, "Hyaluronate coating enhances the delivery and biocompatibility of gold nanoparticles," vol. 186, pp. 243–251. [Online]. Available: https://linkinghub.elsevier.com/retrieve/pii/S014486171830064X

[59] E. F. Hansen, S. N. Lee, and H. Sobel, "The effects of relative humidity on some physical properties of modern vellum," vol. 31, no. 3, pp. 325–242. [Online]. Available: https://cool.culturalheritage.org/jaic/articles/jaic31-03-005.html

[60] P. Matteini, R. Cicchi, F. Ratto, D. Kapsokalyvas, F. Rossi, M. de Angelis, F. Pavone, and R. Pini, "Thermal transitions of fibrillar collagen unveiled by second-harmonic generation microscopy of corneal stroma," vol. 103, no. 6, pp. 1179–1187. [Online]. Available: https://linkinghub.elsevier.com/retrieve/pii/S0006349512009228

[61] V. S. Meli, A. T. Rowley, P. K. Veerasubramanian, S. E. Heedy, W. F. Liu, and S.-W. Wang, "Modulation of stiffness-dependent macrophage inflammatory responses by collagen deposition," vol. 10, no. 4, pp. 2212–2223. [Online]. Available: https://pubs.acs.org/doi/10.1021/acsbiomaterials.3c01892

[62] W. Ou, B. Zhou, J. Shen, C. Zhao, Y. Y. Li, and J. Lu, "Plasmonic metal nanostructures: concepts, challenges and opportunities in photo-mediated chemical transformations," vol. 24, no. 2, p. 101982. [Online]. Available: https://linkinghub.elsevier.com/retrieve/pii/S2589004220311792

[63] D. K. Roper, W. Ahn, and M. Hoepfner, "Microscale heat transfer transduced by surface plasmon resonant gold nanoparticles," vol. 111, no. 9, pp. 3636–3641. [Online]. Available: https://pubs.acs.org/doi/10.1021/jp064341w

[64] X. Liu, B. Li, F. Fu, K. Xu, R. Zou, Q. Wang, B. Zhang, Z. Chen, and J. Hu, "Facile synthesis of biocompatible cysteine-coated CuS nanoparticles with high photothermal conversion efficiency for cancer therapy," vol. 43, no. 30, pp. 11 709–11 715, publisher: The Royal Society of Chemistry. [Online]. Available: https://pubs.rsc.org/en/content/articlelanding/2014/dt/c4dt00424h

[65] Q. Tian, F. Jiang, R. Zou, Q. Liu, Z. Chen, M. Zhu, S. Yang, J. Wang, J. Wang, and J. Hu, "Hydrophilic cu_9 s_5 nanocrystals: A photothermal agent with a 25.7% heat conversion efficiency for photothermal ablation of cancer cells *in Vivo*," vol. 5, no. 12, pp. 9761–9771. [Online]. Available: https://pubs.acs.org/doi/10.1021/nn203293t

[66] K. Jiang, D. A. Smith, and A. Pinchuk, "Size-dependent photothermal conversion efficiencies of plasmonically heated gold nanoparticles," vol. 117, no. 51, pp. 27 073–27 080, publisher: American Chemical Society. [Online]. Available: https://doi.org/10.1021/jp409067h

[67] Vikas, R. Kumar, and S. Soni, "Concentration-dependent photothermal conversion efficiency of gold nanoparticles under near-infrared laser and broadband irradiation," vol. 14, pp. 205–217. [Online]. Available: https://www.ncbi.nlm.nih.gov/pmc/articles/PMC9924363/

[68] M. Yuan, Y. Wang, D. Hwang, and J. P. Longtin, "Thermocouple-tip-exposing temperature assessment technique for evaluating photothermal conversion efficiency of plasmonic nanoparticles at low laser power density," vol. 90, no. 9, p. 094902. [Online]. Available: https://doi.org/10.1063/1.5109117

[69] M. Almada, B. Leal-Martínez, N. Hassan, M. Kogan, M. Burboa, A. Topete, M. Valdez, and J. Juárez, "Photothermal conversion efficiency and cytotoxic effect of gold nanorods stabilized with chitosan, alginate and poly(vinyl alcohol)," vol. 77, pp. 583–593. [Online]. Available: https://linkinghub.elsevier.com/retrieve/pii/S0928493116321993

[70] S. Basaran, S. Dey, S. Bhusari, S. Sankaran, and T. Kraus, "Plasmonic stimulation of gold nanorods for the photothermal control of engineered living materials," vol. 147, p. 213332. [Online]. Available: https://linkinghub.elsevier.com/retrieve/pii/S2772950823000559

[71] A. Paściak, A. Pilch-Wróbel, Marciniak, P. J. Schuck, and A. Bednarkiewicz, "Standardization of methodology of light-to-heat conversion efficiency determination for colloidal nanoheaters," vol. 13, no. 37, pp. 44 556–44 567. [Online]. Available: https://pubs.acs.org/doi/10.1021/acsami.1c12409

[72] G. González-Rubio, P. Llombart, J. Zhou, H. Geiss, O. Peña-Rodríguez, H. Gai, B. Ni, R. Rosenberg, and H. Cölfen, "Revisiting the role of seed size for the synthesis of highly uniform sub-10 nm length gold nanorods," vol. 36, no. 4, pp. 1982–1997. [Online]. Available: https://pubs.acs.org/doi/10.1021/acs.chemmater.3c02866

[73] K. Park, L. F. Drummy, R. C. Wadams, H. Koerner, D. Nepal, L. Fabris, and R. A. Vaia, "Growth mechanism of gold nanorods," vol. 25, no. 4, pp. 555–563. [Online]. Available: https://pubs.acs.org/doi/10.1021/cm303659q

[74] J. Mosquera, D. Wang, S. Bals, and L. M. Liz-Marzán, "Surfactant layers on gold nanorods," vol. 56, no. 10, pp. 1204–1212. [Online]. Available: https://pubs.acs.org/doi/10.1021/acs.accounts.3c00101

[75] J. Watt, B. G. Hance, R. S. Anderson, and D. L. Huber, "Effect of seed age on gold nanorod formation: A microfluidic, real-time investigation," vol. 27, no. 18, pp. 6442–6449. [Online]. Available: https://pubs.acs.org/doi/10.1021/acs.chemmater.5b02675

[76] D. Shriver, M. Weller, T. Overton, J. Rourke, and F. Armstrong, *Inorganic Chemistry*, 6th ed. Oxford University Press.

[77] L. Roach, P. L. Coletta, K. Critchley, and S. D. Evans, "Controlling the optical properties of gold nanorods in one-pot syntheses," vol. 126, no. 6, pp. 3235–3243. [Online]. Available: https://pubs.acs.org/doi/10.1021/acs.jpcc.1c10447

[78] F. Scaletti, C. S. Kim, L. Messori, and V. M. Rotello, "Rapid purification of gold nanorods for biomedical applications," vol. 1, pp. 118–123. [Online]. Available: https://linkinghub.elsevier.com/retrieve/pii/S221501611420046X

[79] B. Fultz and J. M. Howe, *Transmission Electron Microscopy and Diffractometry of Materials*. Springer Berlin Heidelberg. [Online]. Available: http://link.springer.com/10.1007/978-3-662-04901-3

[80] T. Kogure, "Electron microscopy," in *Developments in Clay Science*. Elsevier, vol. 5, pp. 275–317. [Online]. Available: https://linkinghub.elsevier.com/retrieve/pii/B9780080982595000111

[81] H. Katz-Boon, C. J. Rossouw, M. Weyland, A. M. Funston, P. Mulvaney, and J. Etheridge, "Three-dimensional morphology and crystallography of gold nanorods," vol. 11, no. 1, pp. 273–278. [Online]. Available: https://pubs.acs.org/doi/10.1021/nl103726k

[82] X.-F. Wan, M. Liu, K. Lin, X.-S. Chai, G.-X. Chen, and X. Zhou, "Determination of average molecular weight of guar gum by a simple twice headspace extraction gas chromatographic technique," vol. 70, pp. 170–173. [Online]. Available: https://www.sciencedirect.com/science/article/pii/S0142941818304458

[83] G. Ramanathan, M. Hassan, and Y. Rochev, "Optimising the viscoelastic properties of hyaluronic acid hydrogels through colloidal particle interactions: A response surface methodology approach," vol. 703, p. 135320. [Online]. Available: https://linkinghub.elsevier.com/retrieve/pii/S0927775724021848

[84] R. G. Larson, *The Structure and Rheology of Complex Fluids*. Oxford University Press.

[85] K. Whitcomb, "Determining the linear viscoelastic region in oscillatory measurements."

[86] N. N. Mahmoud, R. Hamed, and E. A. Khalil, "Colloidal stability and rheological properties of gold nanoparticle–loaded polymeric hydrogels: impact of nanoparticle's shape, surface modification, and concentration," vol. 298, no. 8, pp. 989–999. [Online]. Available: https://doi.org/10.1007/s00396-020-04659-8

[87] Z. F. Williams, P. Tenzel, W. B. Hooks, and W. W. Hope, "Suture to wound length ratio in abdominal wall closure: how well are we doing?" vol. 21, no. 6, pp. 869–872. [Online]. Available: http://link.springer.com/10.1007/s10029-017-1667-y

[88] M. Orlinsky, R. M. Goldberg, L. Chan, A. Puertos, and H. L. Slajer, "Cost analysis of stapling versus suturing for skin closure," vol. 13, no. 1, pp. 77–81. [Online]. Available: https://www.sciencedirect.com/science/article/pii/0735675795902481

[89] S. C. Nguyen, Q. Zhang, K. Manthiram, X. Ye, J. P. Lomont, C. B. Harris, H. Weller, and A. P. Alivisatos, "Study of heat transfer dynamics from gold nanorods to the environment *via* time-resolved infrared spectroscopy," vol. 10, no. 2, pp. 2144–2151. [Online]. Available: https://pubs.acs.org/doi/10.1021/acsnano.5b06623

[90] A. Kyrsting, P. M. Bendix, D. G. Stamou, and L. B. Oddershede, "Heat profiling of three-dimensionally optically trapped gold nanoparticles using vesicle cargo release," vol. 11, no. 2, pp. 888–892. [Online]. Available: https://pubs.acs.org/doi/10.1021/nl104280c

[91] H. Ma, P. M. Bendix, and L. B. Oddershede, "Large-scale orientation dependent heating from a single irradiated gold nanorod," vol. 12, no. 8, pp. 3954–3960. [Online]. Available: https://pubs.acs.org/doi/10.1021/nl3010918

[92] L. Bianchi, R. Mooney, Y. Cornejo, C. Hyde, E. Schena, J. M. Berlin, K. Aboody, and P. Saccomandi, "Fiber bragg grating sensors-based thermometry of gold nanorod-enhanced photothermal therapy in tumor model," vol. 22, no. 12, pp. 11 297–11 306. [Online]. Available: https://ieeexplore.ieee.org/document/9435308/

[93] A. Bellone, E. Ullo, M. Olivero, G. Coppa, A. Vallan, and G. Perrone, "Preliminary analysis of the estimation of tissue thermal parameters for tumor laser ablation with minimally invasive techniques," in *2024 IEEE International Instrumentation and Measurement Technology Conference (I2MTC)*, pp. 1–6, ISSN: 2642-2077. [Online]. Available: https://ieeexplore.ieee.org/document/10561198/?arnumber=10561198&tag=1

[94] F. Morra, M. De Landro, S. Korganbayev, A. Wolf, A. Dostovalov, A. Cigada, and P. Saccomandi, "Spatially resolved thermometry during laser ablation in tissues: Distributed and quasi-distributed fiber optic-based sensing," vol. 58, p. 102295. [Online]. Available: https://linkinghub.elsevier.com/retrieve/pii/S1068520020302856

[95] Z. S. Mbalaha, D. J. S. Birch, and Y. Chen, "Photothermal effects of gold nanorods in aqueous solution and gel media: Influence of particle size and excitation wavelength," vol. 17, no. 2, pp. 103–111. [Online]. Available: https://ietresearch.onlinelibrary.wiley.com/doi/10.1049/nbt2.12110

[96] G. King and T. Fukushima, "RTD interfacing and linearization using an ADuC8xx MicroConverter®."

[97] M. Baum, "Laser consolidation of ITO nanoparticles for the generation of thin conductive layers on transparent substrates."

[98] W. I. Choi, J.-Y. Kim, C. Kang, C. C. Byeon, Y. H. Kim, and G. Tae, "Tumor regression *In Vivo* by photothermal therapy based on gold-nanorod-loaded, functional nanocarriers," vol. 5, no. 3, pp. 1995–2003. [Online]. Available: https://pubs.acs.org/doi/10.1021/nn103047r

[99] X. Huang, I. H. El-Sayed, W. Qian, and M. A. El-Sayed, "Cancer cell imaging and photothermal therapy in the near-infrared region by using gold nanorods," vol. 128, no. 6, pp. 2115–2120. [Online]. Available: https://pubs.acs.org/doi/10.1021/ja057254a

[100] Y. Xu, R. He, D. Lin, M. Ji, and J. Chen, "Laser beam controlled drug release from ce6–gold nanorod composites in living cells: a FLIM study," vol. 7, no. 6, pp. 2433–2441. [Online]. Available: https://xlink.rsc.org/?DOI=C4NR05574H

[101] K. C. Hribar, M. H. Lee, D. Lee, and J. A. Burdick, "Enhanced release of small molecules from near-infrared light responsive polymernanorod composites," vol. 5, no. 4, pp. 2948–2956. [Online]. Available: https://pubs.acs.org/doi/10.1021/nn103575a

[102] D. Xue and R. Sethi, "Viscoelastic gels of guar and xanthan gum mixtures provide long-term stabilization of iron micro- and nanoparticles," vol. 14, no. 11, p. 1239. [Online]. Available: https://doi.org/10.1007/s11051-012-1239-0

[103] H. Abdi and L. J. Williams, "Tukey's honestly significant difference (HSD) test," in *Encyclopedia of Research Design*. Sage.

[104] C. Williamson and J. R. Scholtz, "Time-temperature relationships in thermal blister formation," vol. 12, no. 1, pp. 41–47. [Online]. Available: https://linkinghub.elsevier.com/retrieve/pii/S0022202X15503473

[105] A. R. Moritz and F. C. Henriques, "Studies of thermal injury: II. the relative importance of time and surface temperature in the causation of cutaneous burns," vol. 23, no. 5, pp. 695–720.

[106] S. Sevitt, "Local blood-flow changes in experimental burns," vol. 61, no. 3, pp. 427–442, _eprint: https://onlinelibrary.wiley.com/doi/pdf/10.1002/path.1700610313. [Online]. Available: https://onlinelibrary.wiley.com/doi/abs/10.1002/path.1700610313

[107] J. Bull, "Burns," vol. 39, pp. 717–723.

[108] J. P. Abraham, B. Plourde, L. Vallez, J. Stark, and K. R. Diller, "Estimating the time and temperature relationship for causation of deep-partial thickness skin burns," vol. 41, no. 8, pp. 1741–1747. [Online]. Available: https://linkinghub.elsevier.com/retrieve/pii/S0305417915001746

[109] H.-W. Huang and T.-L. Horng, "Bioheat transfer and thermal heating for tumor treatment," in *Heat Transfer and Fluid Flow in Biological Processes*, pp. 1–42, journal Abbreviation: Heat Transfer and Fluid Flow in Biological Processes.

[110] J. Zhang, J. Hills, Y. Zhong, B. Shirinzadeh, J. Smith, and C. Gu, "Modeling of soft tissue thermal damage based on GPU acceleration," vol. 24, pp. 5–12. [Online]. Available: https://www.tandfonline.com/doi/full/10.1080/24699322.2018.1557891

[111] S.-C. Pan, "Burn blister fluids in the neovascularization stage of burn wound healing: A comparison between superficial and deep partial-thickness burn wounds," vol. 1, no. 1, pp. 2321–3868.113 332. [Online]. Available: https://doi.org/10.4103/2321-3868.113332

[112] M. A. Mackey, M. R. K. Ali, L. A. Austin, R. D. Near, and M. A. El-Sayed, "The most effective gold nanorod size for plasmonic photothermal therapy: Theory and in vitro experiments," vol. 118, no. 5, pp. 1319–1326, publisher: American Chemical Society. [Online]. Available: https://doi.org/10.1021/jp409298f

[113] X. Wang, G. Li, Y. Ding, and S. Sun, "Understanding the photothermal effect of gold nanostars and nanorods for biomedical applications," vol. 4, no. 57, pp. 30 375–30 383. [Online]. Available: https://xlink.rsc.org/?DOI=C4RA02978J

[114] B. Alberts, A. Johnson, J. Lewis, M. Raff, K. Roberts, and P. Walter, "Fibroblasts and their transformations: The connective-tissue cell family," in *Molecular Biology of the Cell. 4th edition*. Garland Science. [Online]. Available: https://www.ncbi.nlm.nih.gov/books/NBK26889/

[115] I. A. Cree, "Chapter 20 - cell sensitivity assays: The MTT assay," in *Cancer Cell Culture: Methods and Protocols*, ser. Methods in Molecular Biology. Humana Press, no. 731, pp. 237–245. [Online]. Available: https://link.springer.com/10.1007/978-1-61779-080-5

[116] Molar mass of gold - gold nanoparticles molecular weight. [Online]. Available: https://www.nanopartz.com/gold-nanoparticles-molecular-weight.asp?srsltid=AfmBOoo9H0kvoOfa4ksSHIyGaqlUNEB_RPaMKJCsonpTT5jsZLV5x_OB

[117] K. Haas. 2.5: Uncertainty in values determined from a calibration curve. [Online]. Available: https://chem.libretexts.org/Courses/Duke_University/CHEM_401L%3A_Analytical_Chemistry_Lab/CHEM_401L%3A_Analytical_Chemistry_Lab_Manual/02%3A_Calibration_and_Quantitative_Techniques/2.05%3A_Uncertainty_in_values_determined_from_a_Calibration_Curve

[118] J. R. Taylor, *An Introduction to Error Analysis: The Study of Uncertainties in Physical Instruments*, 2nd ed. University Science Books.

APPENDICES

Appendix A

Biosolder-Relevant Concentration Calculations

The literature examples in Table 1.1 reported different concentration units. For easier comparison, polymer and GNR concentrations were converted to common units of (% w/v) and (nM), respectively. As well, the calculation of the uncertainty of experimental GNR concentrations is provided.

A.1 Polymer Concentration Conversions for Literature Values

Polymer concentration unit conversions can be done in the following sequence:

$$\text{weight percent} \rightarrow \text{mass per volume} \rightarrow \text{percent weight per volume}$$

or

$$\text{wt\%} \rightarrow \text{g/mL} \rightarrow \text{\% w/v}$$

From Table 1.1, the concentration of silk protein from [13] is 6 wt%. As an example, this section converts this concentration in wt% to % w/v. First, to convert **wt% to g/mL**, the following calculation can be done (assuming the density of water is 1.00 g/mL):

$$6\ \text{wt\%} = \frac{6\ \text{g silk}}{100\ \text{g total solution}} \times 100\% = \frac{6\ \text{g silk}}{6\ \text{g silk} + 94\ \text{g water}} \times 100\%$$
$$\Rightarrow \frac{6\ \text{g}}{94\ \text{mL}} = 0.06383\ \text{g/mL}$$

The conversion from **g/mL to % w/v** is then simply 0.01 g/mL = 1% w/v. Therefore, 6 wt% = 6.383% w/v.

A.2 GNR Concentration Conversions for Literature Values

GNR concentration unit conversions can be done in the following sequence:

$$\text{weight percent} \rightarrow \text{mass per volume} \rightarrow \text{molarity}$$
$$\text{or}$$
$$\text{wt\%} \rightarrow \text{g/mL} \rightarrow \text{M}$$

The papers by Huang [10] and Urie [9, 13] in Table 1.1 reported GNR concentrations in units of wt%. The above sequence of conversions was used to approximate their concentrations in molarity (M = mol/L). The Urie GNR concentration (5 wt%) is used as an example calculation for the remainder of this section.

To convert wt% to g/mL, the following calculation can be done (assuming the density of water is 1.00 g/mL):

$$5\ \text{wt\%} = \frac{5\ \text{g GNRs}}{100\ \text{g total solution}} \times 100\% = \frac{5\ \text{g silk}}{5\ \text{g silk} + 95\ \text{g water}} \times 100\%$$
$$\Rightarrow \frac{5\ \text{g}}{95\ \text{mL}} = 0.0526\ \text{g/mL}$$

The conversion of GNR concentration from **g/mL to M** requires the average molecular weight (g/mol), which itself relies on an assumption of nanoparticle volume [54, 116]. To calculate the volume of a single GNR, the particle is assumed to consist of a cylinder that is capped by two hemispheres on either end:

$$Volume\ of\ one\ GNR = \pi r^2 (l - 2r) + \frac{4}{3}\pi r^3 \qquad [\text{nm}^3] \quad \text{(A.1)}$$

where r is the radius of the GNR, and l is the length of the GNR. Therefore, continuing with the Urie example, which reported an average GNR diameter and length of 15 nm and 50 nm, respectively:

$$\begin{aligned} Volume\,of\,one\,GNR &= \pi(7.5\text{ nm})^2(50\text{ nm} - 2(7.5\text{ nm})) + \frac{4}{3}\pi(7.5\text{ nm})^3 \\ &= 7952.16\text{ nm}^3\text{/particle} \end{aligned}$$

Next, the GNR molecular weight is calculated by

$$MW = Volume\,of\,one\,GNR \times \rho_{\text{Au}} \times N_A \qquad [\text{g/mol}] \quad (A.2)$$

where ρ_{Au} is the density of gold (19.32 g/cm^3) and N_A is Avogadro's number (6.022×10^{23} particles/mol). Therefore, continuing with the Urie example,

$$\begin{aligned} MW &= 7952.16\text{ nm}^3\text{/particle} \times 19.32\text{ g/cm}^3 \times (6.022 \times 10^{23}\text{ particles/mol}) \\ &= 9.2519 \times 10^7\text{g/mol} \end{aligned}$$

The concentration in molar (molarity) is then calculated by

$$C = C\text{ (g/mL)} \times \frac{1000\text{ mL}}{\text{L}} \div MW \qquad [\text{M}] \quad (A.3)$$

As such,

$$\begin{aligned} C\text{ (M)} &= 0.0526\text{ g/mL} \times \frac{1000\text{ mL}}{\text{L}} \div 9.2519 \times 10^7\text{g/mol} \\ &= 5.689 \times 10^{-7}\text{ M} \\ &= 568.9\text{ nM} \end{aligned}$$

Therefore, for the GNRs reported by Urie [9], a concentration of 5 wt% = 568.9 nM.

A.3 Uncertainty in Concentration Curve-Derived Values

The uncertainty in any value calculated from a linear concentration curve can be determined by the following formula [117]:

$$\sigma_C = \frac{\sigma_{A_\lambda}}{|m|}\sqrt{\frac{1}{k}+\frac{1}{N}+\frac{(A_\lambda - \overline{A_\lambda})^2}{m^2\sum_{i=1}^{N}(C_i-\overline{C})^2}} \tag{A.4}$$

where σ_{A_λ} is the standard deviation in absorbance (obtained from Excel LINEST function), m is the slope of the regression line, k is the number of replicates for the GNR sample, N is the total number of calibration points, A_λ is the measured absorbance of the GNR sample, $\overline{A_\lambda}$ is the average absorbance for all calibration points, and $\sum_{i=1}^{N}(C_i-\overline{C})^2$ is the sum of the squared deviations for the calibration curve concentrations (obtained from Excel LINEST function).

Synthesized GNR stock solution concentrations (4.40 nM and 5.97 nM for Chapters 4 and 5, respectively) were determined via a linear concentration curve and the Beer-Lambert Law, as described in Section 2.2.4. The uncertainty in the GNR stock concentration is therefore

$$\sigma_{C,stock} = \frac{\sigma_{A_\lambda}}{|m|}\sqrt{\frac{1}{k}+\frac{1}{N}+\frac{(A_{\lambda,stock} - \overline{A_\lambda})^2}{m^2\sum_{i=1}^{N}(C_i-\overline{C})^2}} \tag{A.5}$$

where $A_{\lambda,stock}$ is the absorbance of the GNR stock concentration used. For 4.40 nM GNRs, $A_{\lambda,stock}$ = 5.1464. For 5.97 nM GNRs, $A_{\lambda,stock}$ = 6.960. By (A.5), the calculated uncertainties for the GNR stock concentrations C_{stock} = 4.40 nM and 5.97 nM are 0.0890 nM and 0.1215 nM, respectively.

To prepare the reported dilutions of GNRs (0.7 nM and 1.4 nM), the dilution equation was used:

$$C_{stock}V_{stock} = C_{dil}V_{dil} \tag{A.6}$$

where C_{stock} is the concentration of the GNR stock, V_{stock} is the volume of the GNR stock, C_{dil} is the concentration of the GNR dilution, and V_{dil} is the volume of the GNR dilution. By standard uncertainty propagation methods [118] for multiplication and division relationships, the corresponding uncertainty for a diluted concentration is

$$\sigma_{C_{dil}} = C_{dil}\sqrt{\left(\frac{\sigma_{C_{stock}}}{C_{stock}}\right)^2+\left(\frac{\sigma_{V_{stock}}}{V_{stock}}\right)^2+\left(\frac{\sigma_{V_{dil}}}{V_{dil}}\right)^2} \tag{A.7}$$

where $\sigma_{V_{stock}}$ is the uncertainty in the volume of the GNR stock and $\sigma_{V_{dil}}$ is the uncertainty in the volume of the GNR dilution. It is assumed that the micropipettes used were calibrated and the uncertainties in the volumes ($\sigma_{V_{stock}}$ and $\sigma_{V_{dil}}$) are small compared to the uncertainty in the GNR stock concentration ($\sigma_{C_{stock}}$). Therefore, (A.7) reduces to

$$\sigma_{C_{dil}} = \frac{C_{dil}}{C_{stock}} \sigma_{C_{stock}} \tag{A.8}$$

By (A.8), the uncertainties in GNR dilution concentrations 0.7 nM and 1.4 nM are 0.0141 nM and 0.0282 nM, respectively, for Chapter 4 data. For Chapter 5 data, the uncertainties in GNR dilution concentrations 0.7 nM and 1.4 nM are 0.019 nM and 0.0387 nM, respectively.

For the determination of η, the uncertainty in calculated absorbance values A_λ was determined using a similar approach to (A.4), except using the reflected or flipped axes:

$$\sigma_{A_\lambda} = \frac{\sigma_C}{|m|} \sqrt{\frac{1}{k} + \frac{1}{N} + \frac{(C-\overline{C})^2}{m^2 \sum_{i=1}^{N} (A_{\lambda,i} - \overline{A_\lambda})^2}} \tag{A.9}$$

where C is the GNR concentration used in the study (0, 0.7, 1.4 nM). The corresponding values of σ_{A_λ} were (0.0142, 0.0175, 0.0315).

Appendix B

ImageJ Analysis Method for Calculating GNR Size Distribution

Obtained TEM micrographs of GNRs (example shown in Fig. B.1) were imported into the ImageJ software. The pixel-to-distance scale was set by using the scale bar provided at the bottom right of each micrograph. Following this, a line was drawn across either the length or the diameter of the GNR to measure these dimensions (see Fig. B.2). This was repeated for 144 randomly selected GNRs. The resulting aspect ratio was calculated by AR = average rod length/average rod diameter.



Figure B.1: Example of a raw TEM micrograph obtained using the Philips CM10 TEM.

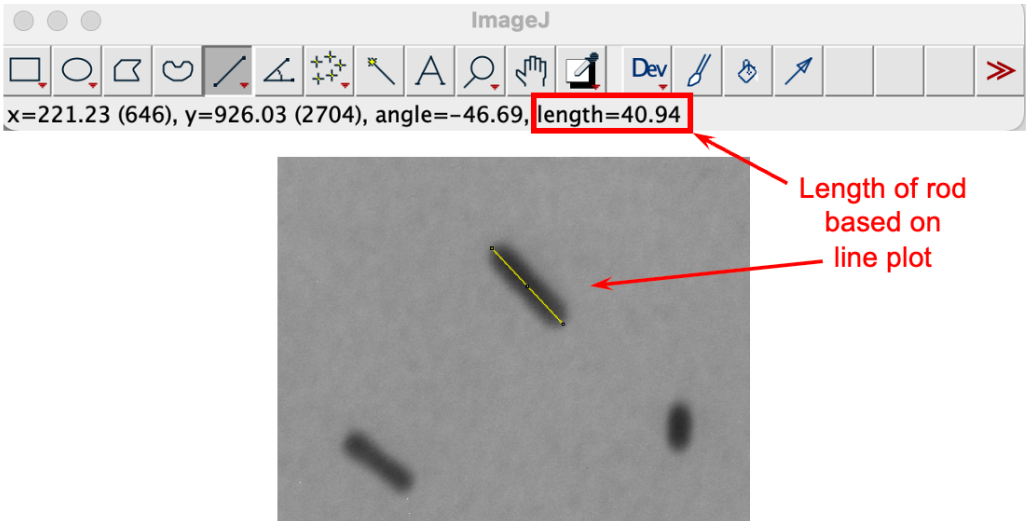


Figure B.2: ImageJ analysis of a single GNR from Fig. B.1 micrograph, showing how the length is measured. The same can be done for the diameter.

Appendix C

CAD Technical Drawings

C.1 Laser Holder Clamp

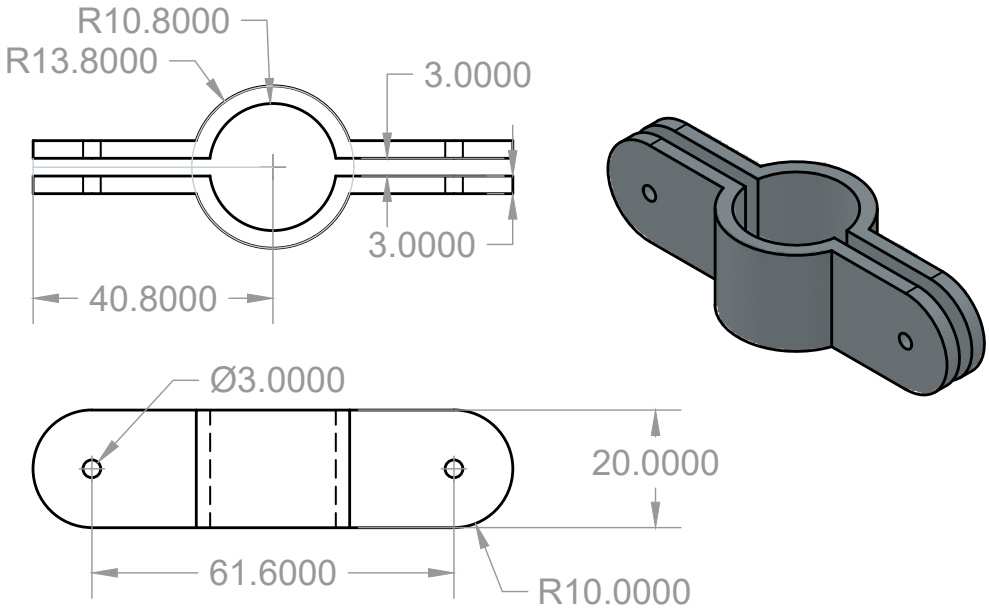


Figure C.1: CAD schematic for laser clamp (AutoCAD).

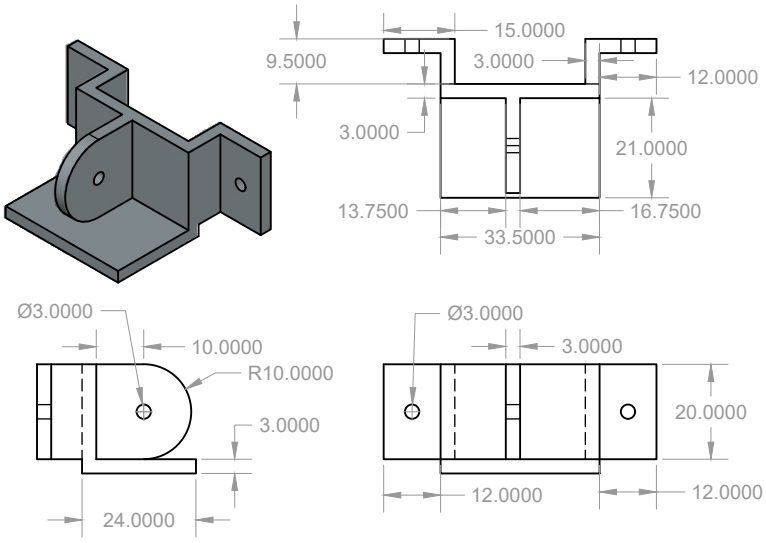


Figure C.2: CAD schematic for the front piece of the stand clamp. Unit = mm, created in AutoCAD.

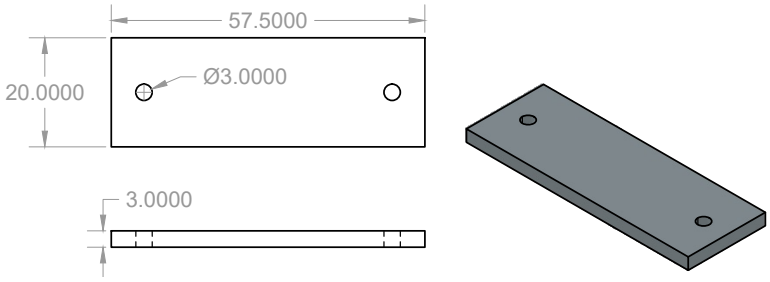


Figure C.3: CAD schematic for the back piece of the stand clamp. Unit = mm, created in AutoCAD.

C.2 Stacked Glass Filter Holder as Microscope Head Attachment

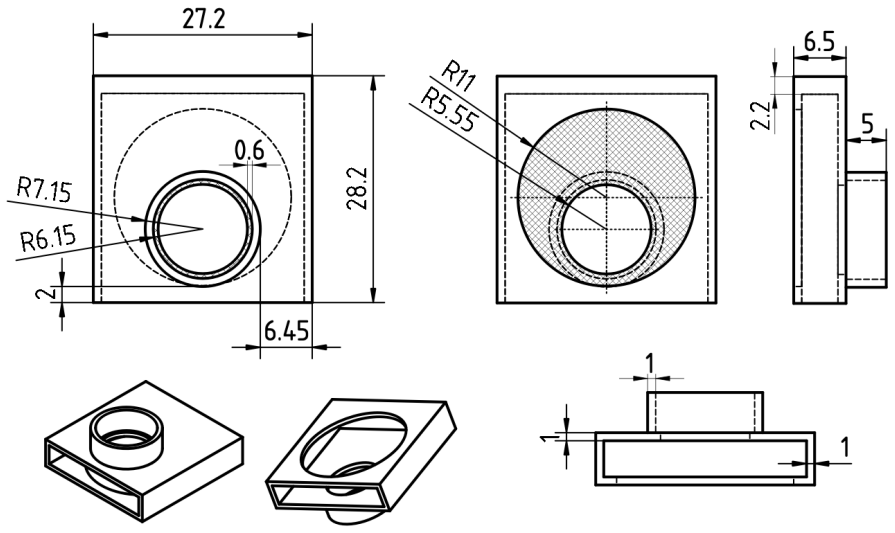


Figure C.4: CAD schematic for stacked glass filter holder which is attached to a USB microscope head for laser spot observation. Unit = mm, created in FreeCAD.

Appendix D

Python Scripts for Laser Control and RTD Measurements in Photothermal Characterization Scheme

The `LTWSystem` class (file: LTW_System.py, displayed in Listing D.1) was written to include all laser control functions. For laser alignment and laser power checks, the PWM code (Listing D.2) is run. The variable `duty_cycle` can be modified to vary laser power output, according to the PWM-to-laser output relation provided in 3.3.

To carry out the temperature collection scheme reported in Section 3.4, Listing D.3 is used. The Python shell prompts the user for four inputs. The appropriate inputted values for the study are provided:

1. Enter length of time for BASELINE temperature readings before turning on laser (recommended 5 s): 5
2. Enter length of time for LASER ON: 30
3. Enter time cutoff (in s): 60
4. Enter desired laser mod duty cycle for step test (0-100%): 20, 40, or 60where 20%, 40%, and 60% duty cycling correspond to 0.98, 1.7, and 2.4 W, respectively.

Listing D.1: LTW class for laser control functions.

```
"""
Created on Fri Dec 7 15:51 2023

This class contains all functions required for the operation of the BoLa
    Diode Laser.

@author: michellehuynh
"""
import numpy as np
import time
import threading

#For laser
import RPi. GPIO as GPIO

class LTWSystem:
    def __init__(self):
        self.PINS = {
            'LASER_GPIO': 21, #MOD+ pin for laser driver
        }

    def initialize_laser(self, initial_mod):
        """
        Initializes laser modulation voltage based on user-defined duty
            cycle.

        Parameters:
            Args:
                initial_mod (float): A duty cycle from 0 - 100 which
                    controls the relative length of digital HIGH pulses to
                    the laser modulation pin.
            Returns:
                None
        """
        global pi_pwm

        #Pin setup
        GPIO.setwarnings(False)
        GPIO.setmode(GPIO.BCM)
        GPIO.setup(self.PINS['LASER_GPIO'], GPIO.OUT)
        pi_pwm = GPIO.PWM(self.PINS['LASER_GPIO'],1000) #1 kHz frequency PWM

        #Turn on laser
        pi_pwm.start(initial_mod) #Set duty cycle
```

```
41          time.sleep(0.0001) #In seconds
42
43          input("Laser modulation voltage initialized at {0}%".format(
                initial_mod))
44
45      def modulate_laser(self, duty_cycle):
46          """
47          Modulates the laser power via PWM (pulse-width modulation). Duty
                cycle arguments that are below 0 or above 100 are treated as 0
                and 100, respectively.
48
49          Parameters:
50              Args:
51                  duty_cycle (float): A duty cycle value which controls the
                        relative length of digital HIGH pulses to the laser
                        modulation pin.
52              Returns:
53                  duty_cycle (float)
54
55          """
56          #Set limits on laser output (PWM duty cycle range is 0-100)
57          if duty_cycle > 100:
58              duty_cycle = 100
59          elif duty_cycle < 0:
60              duty_cycle = 0
61
62          #Modulate laser power
63          pi_pwm.start(duty_cycle)
64          time.sleep(0.0001)
65
66          return duty_cycle
67
68      def estimate_laser_pwr(self, duty_cycle):
69          """
70          Calculates the estimated laser power corresponding to a given
                modulation duty cycle. The calculation is based on empirically
71          derived relationship between duty cycle and laser power measured by
                power meter.
72
73          Parameters:
74              Args:
75                  duty_cycle (float): A duty cycle value which controls the
                        relative length of digital HIGH pulses to the laser
                        modulation pin.
76              Returns:
```

```
77                  laser_pwr(float): Estimated laser power in Watts
78
79          """
80          #Empirical model to calculate laser power
81          if duty_cycle == 0:
82              laser_pwr = 0
83          elif duty_cycle == 100:
84              laser_pwr = 4
85          else:
86              laser_pwr = 0.0355 * duty_cycle + 0.2652
87
88          return laser_pwr
```

Listing D.2: Python script for outputting constant laser power via PWM.

```
1  """
2  Test code for laser PWM
3  (Michelle 20-Sep-2023)
4
5  """
6
7  import RPi.GPIO as GPIO
8  import time
9
10 pwm_pin = 40
11 duty_cycle = 60 #In percentage
12
13 GPIO.setwarnings(False)
14 GPIO.setmode(GPIO.BOARD)
15 GPIO.setup(pwm_pin,GPIO.OUT)
16 pi_pwm = GPIO.PWM(pwm_pin,1000) #1 kHz frequency PWM
17
18 pi_pwm.start(duty_cycle)
19
20 time.sleep(0.0001) #In seconds
```

Listing D.3: Python script for user-set temperature collection and concurrent laser irradiation.

```
1  """
2  SPI connection and Pt100 sampling portions are adapted from original script
       by Adafruit
3  SPDX-FileCopyrightText: 2021 ladyada for Adafruit Industries
4  SPDX-License-Identifier: MIT
5
6  Summary: Real-time temperature output of PT100 temperature sensor using
       Adafruit MAX31865 amplifier module and laser control to a set duty cycle.
```

```
    The user is prompted to input baseline temperature, irradiation time,
    cutoff time and laser duty cycle. A csv file with temperature data is
    outputted in real time.
7
8   @author: michellehuynh
9   """
10
11  #Import necessary libraries
12  from LTW_System import *
13  ltw = LTWSystem()
14
15  #For PT100:
16  import board
17  import digitalio
18  import adafruit_max31865
19  import time
20  import csv
21  from datetime import datetime
22
23  #Initialize SPI connection with PT100
24  spi = board.SPI()
25  cs = digitalio.DigitalInOut(board.D26) #CS on sensor is attached to GPIO 26
26  pt100 = adafruit_max31865.MAX31865(spi, cs, wires=4, rtd_nominal=100.0,
        ref_resistor=430.0)
27
28  #Ask user for sampling time, baseline collection time and laser duty cycle
29  baseline_time = float(input("Enter length of time for BASELINE temperature
        readings before turning on laser (recommended 5 s): "))
30  lasing_time = float(input("Enter length of time for LASER ON: "))
31  time_cutoff = float(input("Enter time cutoff (in s): "))
32  const_duty_cycle = float(input("Enter desired laser mod duty cycle for step
        test (0-100%): "))
33
34  #Initialize csv file:
35  fieldnames = ['Time (s)','Temperature (\u00b0C)']
36  filename = datetime.now().strftime('%Y_%m_%d %H_%M PT100_{0}s Baseline_{1}DC
        .csv'.format(baseline_time,const_duty_cycle))
37
38  with open(filename, 'w') as csv_file: #'w' mode specifies writing on the
        file
39      csv_writer = csv.DictWriter(csv_file, fieldnames=fieldnames)
40      csv_writer.writeheader()
41
42  input("CSV file created. Press Enter to continue...")
43
```

```
#Initialize laser at 0% duty cycle
ltw.initialize_laser(0)
input("You may now turn on the manual laser switch. Press Enter to continue...")

#Ask user to press Enter to start experiment
input("ATTENTION: Press Enter to start the experiment -- temperature readings will start immediately.")

#Take first measurement
time_value = (-1) * baseline_time
start_time = time.monotonic()
temp_value = pt100.temperature

#laser_on = 0
while True:
    #When baseline collection time is reached, turn on the laser
    if (time_value > 0) and (time_value < lasing_time):
        #laser_on = 1
        ltw.modulate_laser(const_duty_cycle)
    if time_value > lasing_time:
        #laser_on = 0
        ltw.modulate_laser(0)

    if time_value > (time_cutoff + 0.25):
        break

    with open(filename, 'a') as csv_file: #'a' mode specifies appending data to file
        csv_writer = csv.DictWriter(csv_file, fieldnames=fieldnames)

        #Create dictionary variables for incoming data to append under the specified headers:
        info = {
            'Time (s)': time_value,
            'Temperature (\u00b0C)': temp_value
            }

        csv_writer.writerow(info)
        print('Time: {0} sec'.format(round(time_value,2)), 'Temperature: {0:.3f}\u00b0C'.format(temp_value))

        #Update data
        temp_value = pt100.temperature
        time_value = time.monotonic() - start_time + (-1) * baseline_time
```

Appendix E

Laser Spot Size Estimation

White, 0.5 mm thick polyethylene terephthalate (PET) sheets were placed directly beneath the laser head. Other white backgrounds, such as printer paper and Teflon sheets were previously implemented, but these were found to scatter or distort the light from the laser spot, rendering the images unusable for analysis.

Similar to the procedure described in Section 3.2, a USB microscope with stacked glass filters was positioned overhead the laser output. The laser duty cycle was set to 40%, corresponding to approximately 1.7 W, and an image of the laser spot was captured using the USB microscope. The laser was turned off and the procedure was repeated to obtain a total of five micrographs. An example micrograph is shown in Fig. E.1.

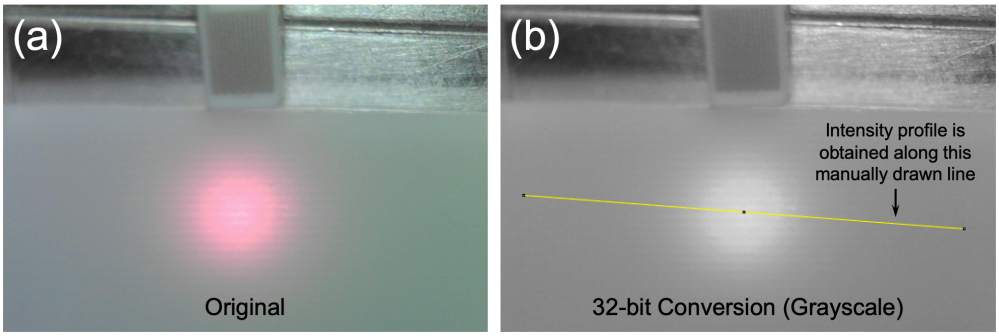


Figure E.1: Example micrograph used for laser spot size estimation for the laser configuration illustrated in Fig. 3.4: (a) Original image, (b) Processed image in ImageJ software with line plot indicated.

The images were imported into the ImageJ software and converted to 32-bit format (grayscale). The pixel-to-distance scale was set by using the Pt100 width (2 mm) as a reference. Following this, a line was drawn across the laser spot (see Fig. E.1b). A gray value intensity profile was then generated using the "Plot Profile" function under the "Analyze" tab. The gray value vs. distance data were exported.

The diameter of the laser spot was estimated using the full width at half maximum (FWHM) parameter. The FWHM is the width of a Gaussian profile at half of its maximum value. To calculate the FWHM, the gray value vs. distance data were imported into a Jupyter notebook and the `curve_fit` function from the `scipy.optimize` Python library was used to fit each micrograph's intensity profile to a Gaussian function:

$$y = A \exp\left(\frac{-(x-x_0)^2}{2\sigma^2}\right) + H \tag{E.1}$$

From these Gaussian fits, the FWHM was then calculated. For illustrative purposes, this process is plotted in Python as well (Fig. E.2). Table E.1 reports the calculated FWHM values, as well as the mean and standard deviation. The Python scripts for the FWHM analysis and plotting is provided in Listing A.6.1.

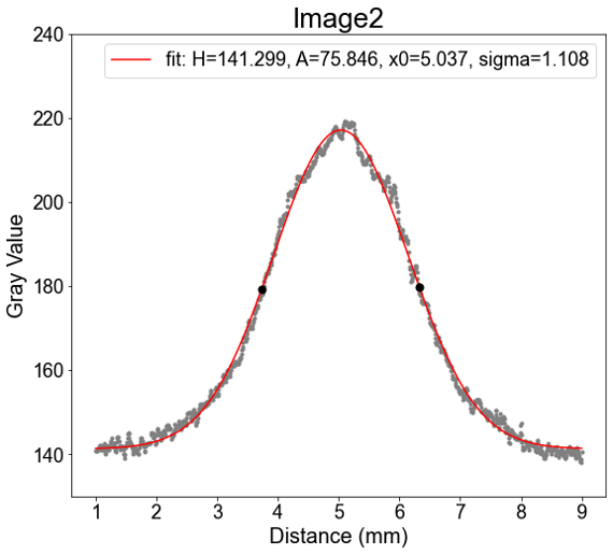


Figure E.2: Intensity profile of the example micrograph shown in Fig. E.1. The Gaussian fitted parameters are listed as well. The black dots indicate the half-maximum points on either side of the Gaussian curve.

Table E.1: FWHM values calculated for each micrograph.

Image No.	**FWHM or Laser Spot Diameter** (mm)
1	2.7327
2	2.5941
3	2.7656
4	2.8000
5	2.7198
Mean ± SD	2.722 ± 0.0699

Listing E.1: Jupyter (Python) Notebook for estimating laser spot size. Analysis for one laser spot image is provided.

```
#Import necessary libraries
import matplotlib.pyplot as plt
plt.rcParams["font.family"] = "Arial"
import pandas as pd
import numpy as np
from scipy.optimize import curve_fit

import os
import glob

#Import csv file
path = "/Users/michellehuynh/Documents/Mayer Group/Work/GNRs/Uncertainty/
    Laser Spot Uncertainty Experiment/Raw images - PET newer microscope/
    ImageJ Intensity Profiles - Raw Data"
csv_files = glob.glob(os.path.join(path, "*.csv"))

file_count = 0
dfs = []
file_locs = []
file_names = []

#Store csv files in dataframes, as well as file locations and names
for file in sorted(csv_files):
    df = pd.read_csv(file)

```

```
24      dfs.append(df)
25      file_locs.append(file)
26      file_names.append(file.split("/")[-1])
27
28      file_count += 1
29
30  print("Total no. of csv files parsed: {0}".format(file_count))
31  print("Files in order:")
32  for i in range(len(file_names)):
33      print(file_names[i])
34
35  #For one example gray value csv file
36  i = 1
37  #Define Gaussian fitting function
38  def fitting_fn(x, H, A, x0, sigma):
39      return H + A * np.exp(-(x - x0)**2 / (2 * sigma **2))
40
41  #Add x and gray value data to arrays (crop distance window to mainly contain
        laser spot)
42  x_data[i] = dfs[i].loc[(dfs[i]['Distance_(mm)'] >= 1) & (dfs[i]['Distance_(
        mm)'] <= 9)]['Distance_(mm)']
43  gray_values[i] = dfs[i].loc[(dfs[i]['Distance_(mm)'] >= 1) & (dfs[i]['
        Distance_(mm)'] <= 9)]['Gray_Value']
44
45  #Determine the Gaussian parameters
46  popts[i], pcovs[i] = curve_fit(fitting_fn , x_data[i], gray_values[i])
47
48  #Calulate FWHM
49  fit_data = fitting_fn(x_data[i], *popts[i])
50  maximum = fit_data.max()
51  minimum = fit_data.min()
52  maximum_index = fit_data.idxmax()
53
54  half_max = minimum + (maximum - minimum) / 2
55  half_max_index1 = fit_data.iloc[(fit_data - half_max).abs().argsort()[:1]].
        index[0]
56  half_max_index2 = maximum_index + (maximum_index - half_max_index1) - 1
57
58  fwhm_indices = [half_max_index1 ,half_max_index2]
59  fwhm = round(abs(x_data[i][fwhm_indices].to_list()[1] - x_data[i][
        fwhm_indices].to_list()[0]),4)
60
61  fwhm_values.append(fwhm)
62
63  #Change font size here
```

```
64  title_fontsize = 26
65  axis_fontsize = 20
66  axis_ticksize = 18
67  legend_fontsize = 18
68
69  #Example plot of Gaussian fit for determining spot size
70  #Initialize plot
71  fig, ax = plt.subplots(nrows=1, ncols=1, figsize=(9,8))
72  fig.patch.set_facecolor('xkcd:white')
73
74  #Plot data
75  plt.plot(x_data[i], gray_values[i], '.', color='gray',zorder=1)
76  plt.plot(x_data[i], fitting_fn(x_data[i], *popts[i]), 'r-', zorder=2,
77           label='fit: H=%5.3f, A=%5.3f, x0=%5.3f, sigma=%5.3f' % tuple(popts[
                 i]))
78
79  #Plot FWHM indicators
80  plt.scatter(x_data[i][fwhm_indices].to_list(), fit_data[fwhm_indices].
        to_list(),
81              color='black', marker='o', s=50, zorder=3)
82
83  ax.set_xlabel('Distance (mm)', fontsize=axis_fontsize)
84  ax.set_ylabel('Gray Value', fontsize=axis_fontsize)
85  ax.set_ylim([130,240])
86  plt.legend(loc='upper right',fontsize=legend_fontsize)
87  ax.tick_params(axis='both', which='major', labelsize=axis_ticksize)
88  plt.title('Image2', fontsize=title_fontsize)
```

Appendix F

Internal SOPs

F.1 Gold Nanorod Synthesis SOP

Protocol Synthesis of Gold Nanorods (GNRs) Tuned to λ ~800 nm	Author(s): Michelle Huynh Kai Zhang
Last Updated: 2025-Jan-20	Version 3.1

Table of Contents

Table of Contents 1
1.0 Background 2
1.1 Procedure Summary 2
1.2 GNR-Forming Mechanism 2
1.3 Procedure Timeline 2
2.0 Safety Considerations 3
3.0 Chemicals & Reagents 5
4.0 Required Items 7
5.0 Equipment 8
6.0 Navigating the "GNR Synthesis Reagent Calculator" Spreadsheet 9
7.0 Detailed Procedure 11
7.1 Chill materials for $NaBH_4$ stock solution preparation (in Section 7.2 step 6) 11
7.2 Stock solutions preparation 11
7.3 Preparation of seed solution 13
7.4 Preparation of growth solution 14
7.5 Generate gold nanorods (GNRs) 14
7.6 Washing and Quality Control 15
7.6.1 Remove large spherical nanoparticles from solution 16
7.6.2 GNR size selection and dispersion in 1X PBS 16
7.6.3 GNR concentration determination 16
8.0 Storage 18
8.1 Colloidal GNRs 18
8.2 Stock solution storage 18
9.0 Waste Disposal 19
References 21
Version Changelog 22

Protocol Synthesis of Gold Nanorods (GNRs) Tuned to λ ~800 nm	Author(s): Michelle Huynh Kai Zhang
Last Updated: 2025-Jan-20	Version 3.1

1.0 Background

1.1 Procedure Summary

This procedure was adapted from the seed-mediated growth method reported by Nikoobakht & El-Sayed in 2003 [1]. The product of this procedure is a solution of CTAB-capped gold nanorods (GNRs) dispersed in 1X phosphate buffered saline (PBS); it can then be used for incorporation into gel matrices. The GNRs possess a longitudinal plasmon band tuned to λ ~800 nm. Safety considerations, materials, devices, tools, and equipment needed are listed in Sections 2-5. Storage and disposal are explained in Sections 7-8.

The procedure involves the reduction of the salt, gold (III) chloride trihydrate ($HAuCl_4 \bullet 3H_2O$). Based on five stock solutions, two solutions called the "seed solution" and "growth solution" are prepared in a cetyltrimethylammonium bromide (CTAB)-rich solution. The seed solution is prepared by the reduction of $HAuCl_4 \bullet 3H_2O$ (Au^{3+}) into elemental gold "seeds" (i.e., nanoparticles < 2 nm in diameter) using sodium borohydride. These seeds serve as nucleation sites for GNR growth. The growth solution is prepared via the weak reduction of the gold salt Au^{3+} into Au^{+}, using L-ascorbic acid.

1.2 GNR-Forming Mechanism

Upon mixing the seed and growth solutions, the reduction of Au^{+} into elemental gold Au^{0} is catalyzed on the surface of the seeds. CTAB preferentially binds to the {110} and {100} facets of the growing GNRs, which causes gold reduction to mainly occur on the ends (or {111} facets). This leads to anisotropic growth in the longitudinal direction [2], [3]. GNRs synthesized by this SOP are shown in Figure 1.

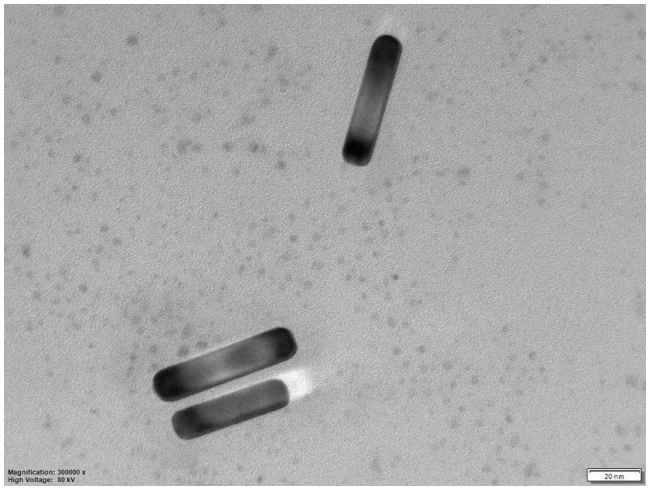


Figure 1: TEM micrograph of in-house synthesized GNRs.

1.3 Procedure Timeline

An estimated timeline of the procedure is given in Table 1, extending over two days. The estimated total time includes a 1.5 h preparation phase and 1.75 h finalization phase, separated by a 24 h (overnight) incubation phase.

Table 1: Procedure timeline.

Day	Task(s)	Time Commitment Estimation (hr)	Corresponding SOP Section(s)
1	Prepare 5 stock solutions	0.5 (active)	6.1 to 6.5
	Prepare seed solution	0.5 (active)	
	Prepare growth solution	0.5 (active)	
	Start overnight incubation	24 (idle)	
2	Spherical particle removal	0.25 (active), 0.5 (idle)	6.6
	GNR size selection	0.5 (active), 0.5 (idle)	

2.0 Safety Considerations

PPE requirements: Goggles, lab coat, nitrile gloves

Sodium borohydride (*$NaBH_4$*):
A highly reactive chemical that needs to be stored appropriately to prevent it from reacting with moisture in the air which would create hydrogen, a combustible gas.
There are two methods for storing/handling $NaBH_4$:

1. Storage under an inert gas (e.g., argon):
    a. Attach the syringe with one end removed to the end of the balloon and parafilm it.
    b. Obtain argon gas.
    c. Work in a fume hood and move the fine balance into it.*
    d. Measure the required mass of sodium borohydride needed and set aside.
2. Storage in a fume hood (never near an open flame), as shown in Figs. 2a and 2b:
    a. Ensure the container is wrapped in spill kit padding material and placed upright in its metal cannister.
    b. Work in a fume hood and move the fine balance into it.*
    c. Measure the required mass of sodium borohydride needed and set aside.

*In the case where the balance cannot be moved to a fume hood, a protective respirator should be worn.

It should be noted that the hydrogen gas production is minimal given amounts/dilutions of $NaBH_4$ used in this protocol.
In case of exposure, contact Ontario Poison Center Toll-Free: 1-800-268-9017.

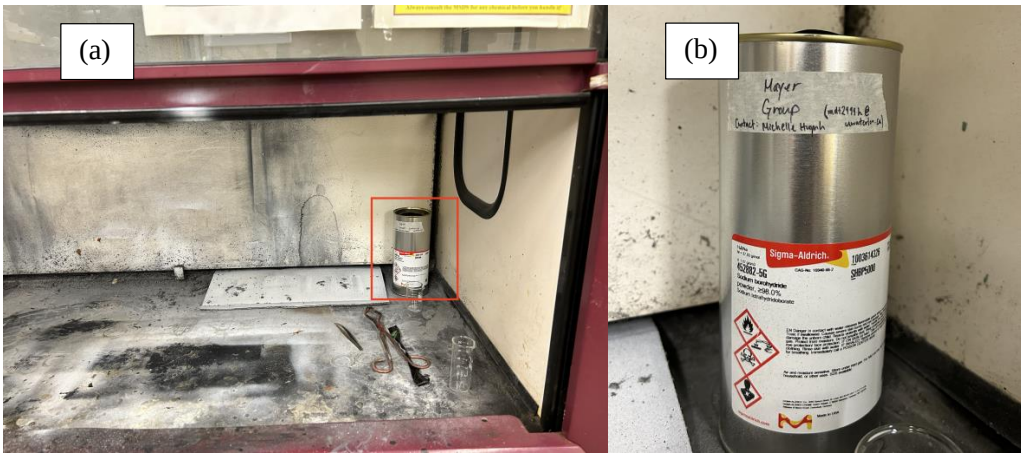


Figure 2: $NaBH_4$ powder stored in E3-2118G fume hood using storage method #2 (a) part of fume hood, (b) zoomed-in for detail.

Protocol Synthesis of Gold Nanorods (GNRs) Tuned to λ ~800 nm	Author(s): Michelle Huynh Kai Zhang
Last Updated: 2025-Jan-20	Version 3.1

3.0 Chemicals & Reagents

The chemicals and reagents necessary for the procedure, together with suppliers and lab locations, are listed in Table 2.

Table 2: Chemical name, supplier information and storage location.

Chemical Name	**Procured From/CAS No.** (if applicable)	**Current Location**	**Minimum Required Amount for SOP** (assuming no previously made stock solutions are available)
Gold (III) chloride trihydrate ($HAuCl4 \bullet 3H_2O$) (>99.99%)	Sigma Aldrich/ 16961-25-4	E6-3009 Our Box (Dr. Bill Anderson's Lab)	0.0200 g
Cetyltrimethylammonium bromide (CTAB) (>98%)	Sigma Aldrich/ 57-09-0	E6-3009 Our Box	1.4578 g
Sodium borohydride ($NaBH_4$) (>98.0%)	Sigma Aldrich/ 16940-66-2	E3-2118G Fume Hood (Dr. Adrian Gerlich's Lab)	0.0045 g
Silver nitrate ($AgNO_3$) (>99.0%)	VWR (or Sigma Aldrich)/ 7761-88-8	E3-2169 Chemical Cabinet (CAMJ Water Lab)	0.0102 g
L-ascorbic acid (99%)	Sigma Aldrich/ 50-81-7	E6-3009 Our Box	0.0139 g
Ultra-pure water (18 MΩ)	Chemstores	E6-3009 Benchtop	60 mL
1X phosphate buffered saline (PBS), pH 7.4, liquid	Sigma Aldrich	E6-3009 Our Box	2 mL

Protocol Synthesis of Gold Nanorods (GNRs) Tuned to λ ~800 nm	Author(s): Michelle Huynh Kai Zhang
Last Updated: 2025-Jan-20	Version 3.1



Figure 3: Chemicals listed in Table 2; (top row, left to right) HAuCl4 • $3H_2O$, CTAB, $NaBH_4$, $AgNO_3$; (bottom row, left to right) L-ascorbic acid, ultra-pure water, 1X PBS.

4.0 Required Items

Materials necessary for the procedure, together with suppliers and lab locations, are listed in Table 3.

Table 3: Material name, supplier information and storage location.

Item Name	Procured From	Current Location
Stainless steel micro-scoopula	Chemstores	E6-3009 Our Box (Dr. Bill Anderson's Lab)
Large stainless-steel scoopula	Chemstores	E6-3009 Our Box
Small plastic scoopula	E6-3009	E6-3009 Sink
20 mL scintillation vials	Chemstores	E6-3009 Our Box
7 mL scintillation vial (optional)	Chemstores	E6-3009 Our Box
50 mL conical tubes	Chemstores	E6-3009 Our Box
15 mL conical tubes	Chemstores	E6-3009 Our Box
10 mL graduated cylinder	E6-3009	E6-3009 Sink
250 mL beaker(s)	E6-3009	E6-3009 Sink
Ice in Styrofoam container	E6-3009 (ice on E6 4th floor)	E6-3009
Aluminum foil	E6-3009	E6-3009
Glass slides (optional)	Chemstores	DC-2726
1.7 mL microcentrifuge tubes	Chemstores	E6-3009

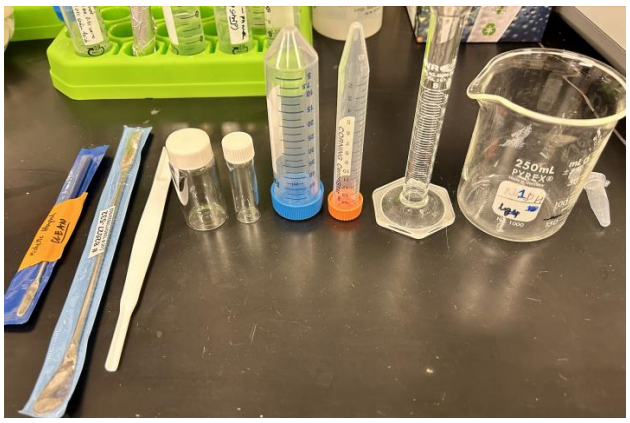


Figure 4: Select materials listed in Table 3 (from left to right); stainless steel micro-scoopula, large stainless-steel scoopula, plastic scoopula, 20 mL scintillation vial, 7 mL scintillation vial, 50 mL conical tube, 15 mL conical tube, 10 mL graduated cylinder, 250 mL beaker, 1.7 mL microcentrifuge tube.

5.0 Equipment

Equipment necessary for the procedure, together with lab locations, are listed in Table 4.

Table 4: Equipment name and location.

Equipment Name	Current Location
Micropipettes	E6-3009
Vortex mixer	E6-3009
Bath sonicator	E6-3009
Microwave	E6-3009
Hot plate	E6-3009 or DC-2726
BioTek Epoch plate reader	E6-3009 (must request access from member of Dr. Anderson's Lab)



Figure 5: Select equipment listed in Table 4 (from left to right); micropipettes, vortex mixer, bath sonicator, microwave, plate reader.

6.0 Navigating the "GNR Synthesis Reagent Calculator" Spreadsheet

This SOP generates 30 mL of GNR solution. To see how the reagent amounts were determined for this SOP, or to prepare different volumes of GNR solution, the following calculator (Excel spreadsheet) can be used: GNR Synthesis Reagent Calculator

(***Link***: https://uofwaterloo-my.sharepoint.com/:x:/r/personal/mdt2999h_uwaterloo_ca/_layouts/15/Doc.aspx?sourcedoc=%7B31728A3E-220A-4C6A-A8F8-2E98AA2DBDE6%7D&file=GNR%20Synthesis%20Reagent%20Calculator.xlsx&action=default&mobileredirect=true)

The three tables in the spreadsheet must be used in order. Only the yellow-highlighted cells require user input. All other cells must *not* be altered. Formulae employed can be accessed by double-clicking relevant cells. Details for each table are provided below:

Calculator Table 1: Set desired final volume for GNR synthesis.

- *User input cells (highlighted yellow in spreadsheet)*:
  - "Target GNR Solution Volume (mL)" (A6)
  - "Target Seed Solution Volume (mL)" (D6)
- *How to use*:
  - Input the desired total GNR volume (prior to washing and quality control) into cell "Target GNR Solution Volume (mL)" (A6). **Default = 30 mL**.
    - *Outputs*:
      - "Required Seed Solution Volume (mL)" (B6)
      - "Growth Solution Volume (mL)" (C6)
  - The required seed solution volume (B6) is in the microliter range (e.g., 35 µL seed solution is required to prepare a 30 mL GNR solution). Reliably preparing such a small volume is unrealistic; it is therefore recommended to prepare the seed solution in excess.
  - Input the desired seed solution volume into cell "Target GNR Solution Volume (mL)" (A6). **Default = 5 mL**.
    - *Outputs*: All required stock solution volumes in **Calculator Table 2** (C12:C17). The values are indicated as red text.
    - Record these values in your lab book, as they are required to carry out Section 7.3 "Preparation of seed solution".

Calculator Table 2: Reagent requirements for a single batch of Nikoobakht & El-Sayed GNR recipe (10.282 mL) which is used to scale up to the desired volumes inputted in Table 1.

- *User input cells*: None
- *How to read*:

- Based on the desired GNR and seed solution volumes inputted in **Calculator Table 1**, the following outputs are provided (indicated in red text):
  - "Total volumes required for seed solution" column (C12:C17)
  - "Total volumes required for growth solution" column (E12:E18)
    - Record these values in your lab book, as they are required to carry out Sections 7.4 "Preparation of growth solution" and 7.5 "Generate gold nanorods (GNRs)".
  - "Total volumes required for (seed + growth)" column (F12:F18)
    - These values are the minimum water and stock solution volumes required to prepare the desired GNR volume.

Calculator Table 3: Stock solution guide to determine (1) target powder weight, and (2) solvent volume adjustments based on actual powder weight.

- *User input cells (highlighted yellow in spreadsheet)*:
  - "Target Stock Volume (mL)" column (C24:C28)
  - "Actual Powder Weighed (g)" column (E24:E28)
- *How to use*:
  - Refer to Table 5 of this SOP document, column "Ultra-pure Water Volume (mL)" in Section 7.2. Input these volumes into the **Calculator Table 3** "Target Stock Volume (mL)" column (C24:C28) for each of the powders listed.
    - *Outputs*: "Target Powder Weight (g)" column (D24:D28)
      - Record both the "Target Stock Volume (mL)" column and "Target Powder Weight (g)" column in your lab book.
      - For each of the powders, aim to weigh out these amounts when preparing the stock solutions according to Section 7.2.
  - When measuring out the target powder weights in Section 7.2, it is likely that the exact weight (to a resolution of 0.1 mg) cannot be achieved. Therefore, the volume of solvent added (ultra-pure water) must be adjusted to maintain the concentration of the stock solution.
  - Input the actual powder weights into "Actual Powder Weighed (g)" (E24:E28).
    - *Outputs*: "Adjusted Volume H2O Required (mL)" column (F24:F28)
      - Record these values in your lab book and prepare the stock solutions with these adjust ultra-pure water volumes following the steps in Section 7.2.

7.0 Detailed Procedure

7.1 Chill materials for $NaBH_4$ stock solution preparation (in Section 7.2 step 6)

1) Pour **5-10 mL** of **ultra-pure water** in a 15 mL centrifuge tube and put on ice (in Styrofoam container).
    a. Always use fresh ultra-pure water for this step! (i.e., Do not use leftover ultra-pure water that has been sitting in a conical tube for more than a day.)
2) Chill a new, empty 20 mL scintillation vial on ice as well.

7.2 Stock solutions preparation

Prepare each of the stock solutions in Table 5, as outlined in the following steps.

Table 5: Overview of stock solution composition and how often they should be prepared.

Stock Solution	**Concentration** (M)	**Powder Required** (g)	**Ultra-pure Water Volume** (mL)	**Frequency of Preparation/ Shelf Life**	**Stored In**
L-ascorbic acid	0.0788	0.0139	1.00	Must be prepared fresh	N/A (discard after use)
$AgNO_3$	0.0040	0.0102	15.0	Can use the same batch for up to **10 months**	E6-3009 Benchtop
$HAuCl_4 \cdot 3H_2O$	0.0127	0.0200	4.00	Can use the same batch for up to **10 months**	E6-3009 Benchtop
CTAB	0.200	1.4578	20.0	Must be prepared fresh	N/A (discard after use)
$NaBH_4$	0.030	0.0045	4.00	Must be prepared fresh	N/A (discard after use)

1) Thoroughly rinse all scoopulas with DI water and dry completely with Kimwipes. It is recommended to prepare the stock solutions in the order outlined in steps 2 to 6.
2) Prepare an L-ascorbic acid stock solution at 0.0788 M:
    a. Using a micro-scoopula, add **13.9 mg of L-ascorbic acid** powder to a new 20 mL scintillation vial.
    b. Pipette **1 mL of ultra-pure water** into the same vial.
    c. Wipe the plastic scoopula thoroughly with a Kimwipe.
3) Prepare an $AgNO_3$ stock solution at 0.0040 M:

a. Using a small **plastic** scoopula, add **10.2 mg of $AgNO_3$** powder to a new 20 mL scintillation vial wrapped in aluminum foil, as it is susceptible to photodegradation.
    i. Do not use a stainless-steel scoopula as $AgNO_3$ is corrosive to metals!
b. Using a 10 mL graduated cylinder, add **15 mL of ultra-pure water** into the same vial.
c. Wipe the micro-scoopula thoroughly with a Kimwipe.

4) Prepare an $HAuCl_4 \cdot 3H_2O$ stock solution at 0.0127 M:
    a. Pipette **4.00 mL of ultra-pure water** into a new 20 mL scintillation vial wrapped in aluminum foil, as it is susceptible to photodegradation.
    b. Using a small **plastic** scoopula, quickly measure **20.0 mg of $HAuCl_4 \cdot 3H_2O$ granules** and add it to the same vial. Keep the lid of the $HAuCl_4 \cdot 3H_2O$ container closed whenever possible.
        i. $HAuCl_4 \cdot 3H_2O$ is hygroscopic (absorbs moisture), so air exposure should be limited!
        ii. Do not use a stainless-steel scoopula as the gold salt will corrode it!
5) Prepare a CTAB stock solution at 0.200 M:
    a. Using a 10 mL graduated cylinder, add **20 mL of ultra-pure water** to a new 50 mL conical tube.
    b. Using a large scoopula, measure **1.4578 g of CTAB powder** and add it to the same tube.
        i. Try to scoop smaller clumps, or break up larger clumps, before adding to the ultra-pure water for faster dissolution.
    c. Place the conical tube in a sufficiently tall beaker (e.g., 250 mL beaker). Make sure the tube cap is screwed on ¼ of the way to allow proper venting.
    d. Place the tube and beaker in the microwave. Microwave in 4 second bursts, making sure to gently swirl the tube between each heating.
        i. Do not microwave for more than 4 seconds at a time, as the CTAB solution will bubble over.
    e. When the solution is mostly clear (with a few clumps visible), it is time to sonicate the solution. (Note that sonication can be skipped if the CTAB is fully dissolved after microwaving).
        i. Fill the beaker with DI water until the water level in the beaker is fairly close to that in the CTAB tube.
        ii. Place the beaker in the bath sonicator and make sure the water level of the sonicator is sufficiently high.
        iii. Sonicate for 5-7 min, occasionally rotating the CTAB tube in the water-filled beaker. When no clumps are visible in the CTAB solution, it is ready to use.

6) Prepare a $NaBH_4$ stock solution at 0.030 M:
    a. Pipette **4.00 mL of ice-cold ultra-pure water** (that was chilled at the start of the procedure) into the chilled 20 mL scintillation vial.
    b. Using a micro-scoopula, very quickly measure **4.5 mg of $NaBH_4$ powder** and add it to the same vial. Work quickly, otherwise the $NaBH_4$ powder will absorb moisture from the air and stick to the weighing paper!
        i. $NaBH_4$ is hygroscopic (absorbs moisture), so air exposure should be limited!

7.3 Preparation of seed solution

For all subsequent pipetting steps, it is imperative to **pipette against the side of the tube** (such that the solution trickles down into the tube). This will limit foam formation in the CTAB solution which could have unintended effects on nanoparticle growth.

1) Pipette **2.358 mL of CTAB stock solution** into a new 15 mL centrifuge tube.
    a. The 100 µL–1000 µL range micropipette can be used to achieve this dispensing resolution.
    b. First do two dispenses of 1000 µL, followed by one dispense of 358 µL.
2) To the same tube, pipette **2.266 mL of ultra-pure water** and then **92.9 µL of $HAuCl_4 \cdot 3H_2O$ stock solution** (to produce a 0.00050 M $HAuCl_4 \cdot 3H_2O$ dilution).
3) Mix gently by swirling/inverting the tube.
4) Pipette **283 µL of the $NaBH_4$ stock solution** to the same tube and mix vigorously on the highest vortex mixer setting for 2 minutes.
    a. The solution should turn a dark reddish brown colour (as shown in Figure 6).
5) Set aside at room temperature for up to 2-3 hours.

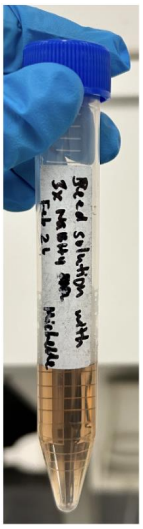


Figure 6: Seed solution immediately after vortex mixing.

7.4 Preparation of growth solution

1) Using a 10 mL graduated cylinder and micropipette, add **13.440 mL of ultra-pure water** to a new 50 mL conical tube.
    a. If making smaller GNR volumes, DO NOT use a 15 mL conical tube. The narrower dimensions will encourage nanorod aggregation.
2) Using a 10 mL graduated cylinder and micropipette, add **14.589 mL of CTAB stock solution** to the same tube.
3) Mix gently by swirling the tube.
4) Pipette **1.149 mL of $HAuCl_4 \bullet 3H_2O$ stock solution** to the same tube for a final concentration of 0.001 M.
5) Mix gently by swirling the tube.
6) Pipette **584 µL of $AgNO_3$ stock solution** to the same tube.
7) Mix gently by swirling the tube.
8) Pipette **209 µL of L-ascorbic acid stock solution** to the same tube.
9) Mix gently by swirling the tube.
    a. The solution should turn colourless indicating successful reduction.
    b. If the solution still has a slight yellowish hue (can compare against the clear CTAB stock solution), then add an additional 10 µL of L-ascorbic acid stock solution to the growth solution. Mix gently by swirling the tube.
10) Wrap the tube in aluminum foil.

7.5 Generate gold nanorods (GNRs)

1) Add **35 µL of seed solution** prepared in "*6.3 Preparation of seed solution*" to the growth solution tube.
2) Prepare the hot plate for incubation.
    a. If the GNR solution in only one 50 mL conical tube:
        i. Place the tube in a 250 mL beaker (or any size beaker that can hold the conical tube). Place the beaker onto the hot plate.
        ii. Set the hot plate temperature to 26°C. Cover the entire hot plate base with a dome of aluminum foil (as shown in Figure 7, left).
    b. If multiple 50 mL conical tubes contain GNR solution:
        i. Tape the tubes together, such that they can remain upright on their own.
        ii. Place three glass slides on the base of the hot plate and place the tubes upright on the glass slides.
        iii. Set the hot plate temperature to 26°C. Cover the entire hot plate base with a dome of aluminum foil (as shown in Figure 7, left).
3) Following overnight incubation, the solution changes from colourless to faintly pink (see Figure 7, right).

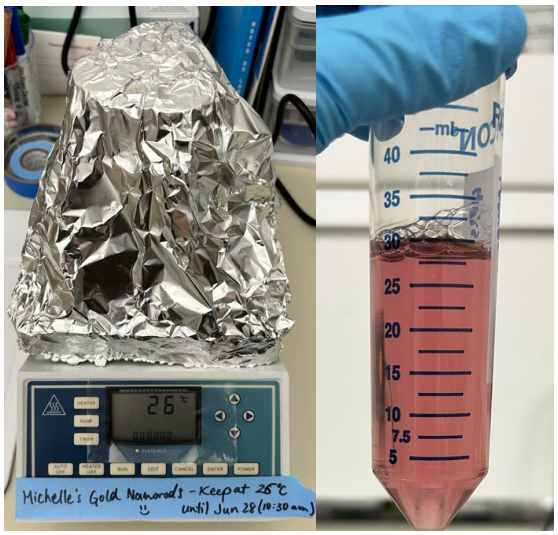


Figure 7: Incubation setup (left) and GNR solution after 20.5 h incubation (right).

7.6.1 Remove large spherical nanoparticles from solution

4) Divide the **30 mL of GNR solution** into two 15 mL conical tubes (i.e., 15 mL solution per tube).
    a. Ensure the tubes' weights are within 100 mg of each other. If not, transfer an appropriate volume between them.
5) Centrifuge at 6500 rpm for 15 min to pull out the spherical nanoparticles (which are contained in the pellet).
6) Decant the solution and reserve the supernatant (i.e., the liquid solution remaining after centrifugation).
7) Split the supernatant equally into two 15 mL conical tubes.
    a. Ensure the tubes' weights are within 100 mg of each other. If not, transfer an appropriate volume between them.
8) Centrifuge at 6500 rpm for 15 min to further improve yield. Reserve the supernatant.

7.6.2 GNR size selection and dispersion in 1X PBS

1) Transfer 1 mL aliquots of the supernatant solution into 1.7 mL microcentrifuge tubes.
2) Centrifuge the 1 mL aliquots at 11000 rpm for 10 min.
    a. Ensure the tubes are evenly spaced in the centrifuge to maintain balance.
3) Discard the supernatant. Resuspend the pellet in 50 µL of 1x PBS.
4) Transfer all GNRs in PBS to a single 20 mL scintillation vial (or 7 mL scintillation vial if less volume is produced). The resultant GNR stock is highly concentrated (typically >4 nM) and should be dark reddish-brown in colour (see Figure 8).



Figure 8: Photograph of concentrated GNR stock solution (ready-to-use).

7.6.3 GNR concentration determination

1) Obtain an absorbance spectrum for the GNR stock solution using UV-vis-NIR spectroscopy:
    a. Pipette 200 µL of the GNR stock solution into a well in a 96-well plate.

b. **Request usage of the Epoch plate reader from a lab member in Dr. Anderson's lab** (Armandeep can assist with this).
c. Through the Gen5 software, obtain a spectrum from 400 to 999 nm with a step size of 4 nm. Export and save the data to as an Excel file. Note that OD (optical density) on the y-axis is absorbance.
d. The position of the longitudinal plasmon peak should be ~800 nm. The magnitude of the longitudinal plasmon peak should be at least 2 times the magnitude of the transverse plasmon peak (see Figure 9 for an example spectrum).

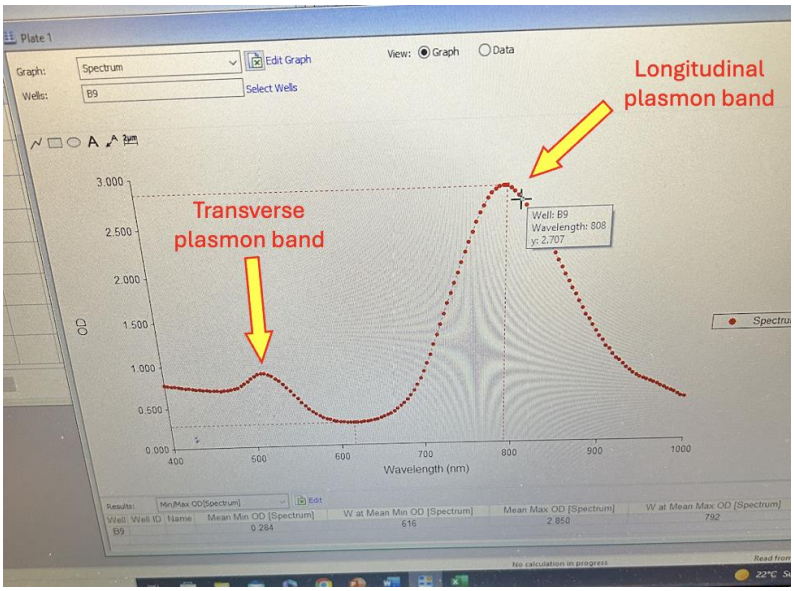


Figure 9: Example absorbance spectrum of GNR solution (in Gen5 user interface).

2) Estimate the concentration using a standard curve previously obtained using commercial GNRs of a known concentration:
   a. Note down the absorbance value at λ = 808 nm.
   b. Using the standard curve (Figure 10), calculate the concentration of the GNR sample using the equation:

$$[\text{GNR}]\ (\text{nM}) = (\text{Absorbance}_{808\ \text{nm}} - 0.044) / 0.6055$$

   c. Label the glass vial with this concentration.

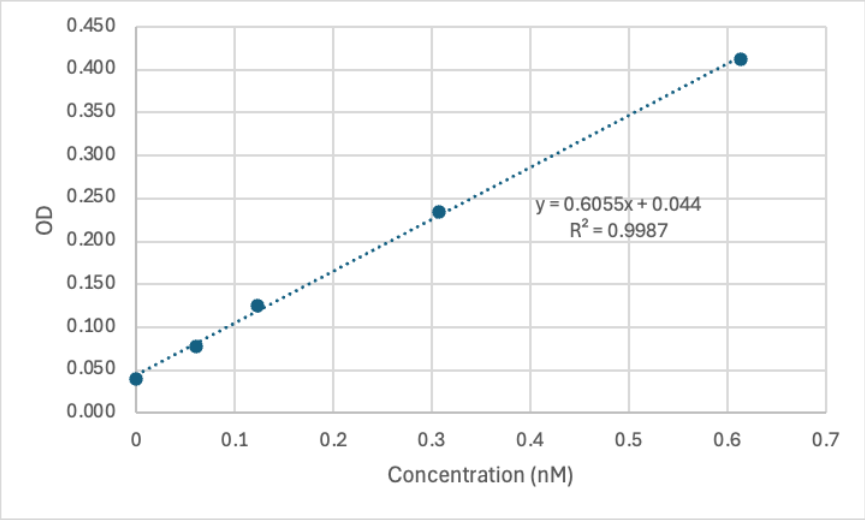


Figure 10: Standard curve for determining GNR concentration.

8.0 Storage

8.1 Colloidal GNRs

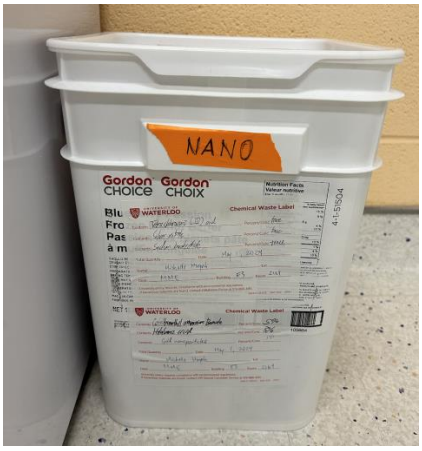
GNR solutions produced by this procedure can be stored at room temperature for several months. Obtain an absorbance spectrum of the GNR solution before use to determine degradation or aggregation if there is concern about their stability.

8.2 Stock solution storage

Any leftover $AgNO_3$ stock solution can be used to produce future GNR batches (they can be stored on the benchtop, wrapped in aluminum foil). Discard the CTAB, L-ascorbic acid, and $NaBH_4$ stock solutions (as these should be prepared fresh every time). $HAuCl_4 \bullet 3H_2O$ stock solutions can be reused as well (as long as they are wrapped in foil).

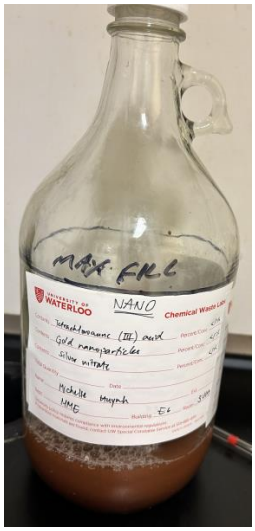
9.0 Waste Disposal

GNR-contaminated solid waste
(bin located on E6-3009 floor next to mini fridge)



Ensure that all solid waste (including, but not limited to, pipette tips, Kimwipes, gloves, etc.) that have been in contact with any of the reagents involved in this protocol are appropriately stored in the designated waste bin containing a completed waste label with "NANO" written on it. The waste should be "double-bagged" as it contains nanomaterial waste.

GNR liquid waste
(container located in E6-3009 fume hood)



All solutions used during this procedure can be deposited in the liquid waste container. When re-securing the container cap, ensure it is only tightened ¼ of the way. This accommodates venting in case any leftover reactions occur in the waste container. Make sure the waste container has a completed waste label with "NANO" written on it. Keep the waste container in the fume hood until disposal at the Environmental Safety Facility (ESF). Make sure the waste container has a completed waste label.

Waste Drop-Off Procedure

1. Book a waste drop-off appointment through this link (Environmental Safety Facility (ESF) location is **ESC 150**): https://uofwaterloo.sharepoint.com/sites/safety/chemsafety/SitePages/Hazardous-Waste---ESF-(Main-Campus).aspx
2. Prior to arriving at the waste appointment, print and fill out the Waste Profile Form: https://uwaterloo.ca/safety-office/sites/default/files/uploads/files/waste_profile_form_fillable_v.1.1_mar2022.pdf
    a. Instructions on how to fill out the Waste Profile Form can be found here: https://uwaterloo.ca/safety-office/sites/default/files/uploads/files/how_to_fill_out_the_waste_profile_form.pdf
    b. A hard copy of this form must be brought to the waste appointment!
3. Prepare the waste containers for drop-off:
    a. **For the solid waste bin**, ensure that BOTH waste bags are individually taped shut (this is to minimize nanomaterial exposure to the individual processing the waste).
    b. For the liquid waste container,
        i. Ensure the bottle is not filled more than 80% (i.e., the liquid level cannot exceed the "bend" line of the container). Over-filled containers are not accepted at the waste facility.
        ii. Carry the container to ESF in a "tote" (totes can be found in the CAMJ Water Lab, E3-2169).
4. At the appointment time, wait in the hallway outside of the waste facility (i.e., stand in the hallway across from the ESC 1st floor elevators). The waste facility manager retrieves you when ready.
5. After the waste has been processed, a new solid waste bin or liquid waste container is provided. Replace waste labels with appropriate information as needed. Store new containers in their designated locations, as before.

References

[1] B. Nikoobakht and M. A. El-Sayed, "Preparation and Growth Mechanism of Gold Nanorods (NRs) Using Seed-Mediated Growth Method," *Chem. Mater.*, vol. 15, no. 10, pp. 1957–1962, May 2003, doi: 10.1021/cm020732l.

[2] K. Park *et al.*, "Growth Mechanism of Gold Nanorods," *Chem. Mater.*, vol. 25, no. 4, pp. 555–563, Feb. 2013, doi: 10.1021/cm303659q.

[3] J. Mosquera, D. Wang, S. Bals, and L. M. Liz-Marzán, "Surfactant Layers on Gold Nanorods," *Acc. Chem. Res.*, vol. 56, no. 10, pp. 1204–1212, May 2023, doi: 10.1021/acs.accounts.3c00101.

Protocol Synthesis of Gold Nanorods (GNRs) Tuned to λ ~800 nm	Author(s): Michelle Huynh Kai Zhang
Last Updated: 2025-Jan-20	Version 3.1

Version Changelog

Version 3.1

- Added Table of Contents.
- Minor edits to improve clarity.
- Included column of minimum required amounts of reagents for procedure in Table 2.
- Included column of storage location for stock solutions in Table 5.
- Provided more details about GNR Synthesis Reagent Calculator including structure, usage, and outputs.

Version 3.0

- Relevant photos were embedded.
- Included a summary and timeline of the procedure in section "1.0 Background".
- Updated "2.0 Safety Considerations" regarding alternative $NaBH_4$ storage.
- Added locations for chemicals, materials and equipment.
- Reworded certain parts of "6.0 Procedure" for better readability and flow.
- Included more details in "8.0 Waste Disposal" regarding waste drop-off procedures.
- Revision to Section "6.5 Generate gold nanorods (GNRs)"
- Revisions to Section "6.6 Washing and Quality Control" regarding centrifugation cycles and dispersion in 1x PBS.
- Updated equipment list according to above changes.

Version 2.1

- Changed incubation temperature from 28°C to 25°C and adjusted incubation time.
- Following centrifugation, the supernatant is reserved (contains the GNRs) as opposed to the pellet.
- All volumes were scaled back up to produce a total GNR volume of 30 mL.
- Guidance on adding the appropriate amount of L-ascorbic acid to the growth solution was adjusted (based on scaled up volume).

Version 2.0

- Several procedural details were included, relating to:
    - Volume changes:
        - Only a total of 5 mL seed solution is prepared to conserve reagents.
        - All volumes related to growth solution were scaled down by a factor of 4 (to match the original procedure outlined by Nikoobakht & El-Sayed).
        - The silver nitrate stock solution volume to add to the growth solution was also adjusted to match the paper.

        - The volume of L-ascorbic acid stock solution to add *prior* to seed solution addition will vary from batch to batch. A guide for the appropriate amount to add is provided.
        - Additional L-ascorbic acid following overnight incubation is no longer added.
    - Higher concentration sodium borohydride is used (from 0.010 M to 0.030 M).
    - Very detailed instructions related to technique were added (to avoid contamination).
    - Reformatted sections for better flow.

Version 1.1

- The sequence of steps (for both seed solution and growth solution preparation) was slightly modified from the previous version.
- More volume of L-ascorbic acid stock solution was added after incubation to improve the longitudinal plasmonic peak height in the absorbance spectrum.
- Instructions pertinent to washing the GNRs were added.

Version 1.0

- First writeup of the protocol

F.2 Preparation of Hyaluronic Acid Guar Gum Gold Nanorod Gel SOP

Protocol Hyaluronic Acid Guar Gum Gold Nanorod Gel Preparation	**Author(s):** Michelle Huynh
Last Updated: 2024-Dec-5	**Version** 1.0

Version Changelog

Version 1.0

- First writeup of the protocol

1.0 Background

Hyaluronic acid (HA) guar gum (GG)-based hydrogels containing gold nanorods (GNRs) are photothermal materials that we developed to use as biological solders in laser tissue welding. HA is the matrix material, GNRs are the photoabsorbing components responsible for amplified heat generation, and GG is an additive to adjust viscosity, as well as improve the stability, and therefore photothermal conversion, of dispersed GNRs.

This protocol details how to prepare biological gel solders with an example composition of 2.75% w/v HA and 0.25% w/v GG, with GNR concentrations of 0 nM (control) and 0.7 nM.

2.0 Chemicals & Reagents

Table 1: Chemical name, supplier information and storage location.

Chemical Name	Procured From/CAS No. (if applicable)	Current Location
Hyaluronic acid sodium salt from *Streptococcus equi*	MilliporeSigma/ 9067-32-7	E6-3009 Freezer Door
Guar gum	MilliporeSigma/ 9000-30-0	E6-3009 Our Box
GNR stock solution	Synthesized in-house using SOP “Protocol - GNR Synthesis - Version 3.0”	E6-3009 Bench
1X phosphate buffered saline (PBS), pH 7.4, liquid	MilliporeSigma	E6-3009 Our Box

3.0 Materials

Table 2: Material name, supplier information and storage location.

Item Name	Procured From	Current Location
10 mL graduated cylinder	E6-3009	E6-3009 Sink (Dr. Bill Anderson’s Lab)
15 mL conical tube	Chemstores	E6-3009 Our Box
Stainless steel micro-scoopula	Chemstores	E6-3009 Our Box
7 mL scintillation vials	Chemstores	E6-3009 Our Box
1.5 mL microcentrifuge tubes	Chemstores	E6-3009 Our Box
50 mL beaker	E6-3009	E6-3009 Sink

4.0 Equipment

Table 3: Equipment name and location.

Equipment Name	Current Location
Micropipettes	E6-3009
Vortex mixer	E6-3009
Bath sonicator	E6-3009

5.0 Procedure

Note that this procedure produces **1 mL** of each gel sample. Amounts stated here can be scaled to any desired final volume.

5.1 Prepare GG stock solution (0.4% w/v)

1. Using a 10 mL graduated cylinder, add **10 mL of 1X PBS** to a 15 mL conical tube.
2. Weigh out **40 mg of GG** and add it to the conical tube.
3. Vortex-mix until fully combined.
4. Over several days, the GG may sediment out of solution. If this occurs, simply vortex-mix until it has resuspended.

Note: A GG stock solution concentration of 0.4% w/v was selected as any higher concentration may make the solution too viscous to pipette.

5.2 Calculate amounts of gel components required

The target gel volume for each batch is 1 mL. Example calculations are shown and summarized in Table 4.

1. For 2.75% w/v HA:

$$m_{HA} = (2.75\%\ \text{w/v})(1\ \text{mL})$$
$$= \left(\frac{2.75\ \text{g HA}}{100\ \text{mL}}\right)(1\ \text{mL})$$
$$\boldsymbol{m_{HA} = 27.5\ \text{mg HA}}$$

2. For 0.25% w/v GG:

$$(0.4\%\ \text{w/v})(V_{stock,GG}) = (0.25\%\ \text{w/v})(1\ \text{mL})$$
$$\boldsymbol{V_{stock,GG} = 625\ \mu\text{L}}$$

3. For 0.7 nM GNRs:

Note: The calculated GNR stock volume, $V_{stock,GNR}$, depends on the GNR stock concentration! What is shown below is an example calculation with GNR stock concentration = 5.9736 nM. The GNR stock concentration should be adjusted accordingly

(as determined by a concentration calibration curve obtained via UV-vis NIR spectroscopy).

$(5.9736\ \text{nM})(V_{stock,GNR}) = (0.7\ \text{nM})(1\ \text{mL})$
$\boldsymbol{V_{stock,GNR} = 117\ \mu\text{L}}$

4. <u>For 1X PBS</u>:
   $V_{total} = 1\ mL = V_{stock,GG} + V_{stock,GNR} + V_{PBS}$
   $V_{PBS}\ [\mu\text{L}] = 1000 - 625 - V_{stock,GNR}$
   $V_{PBS}\ [\mu\text{L}] = 375 - V_{stock,GNR}$

Table 4: Gel sample recipe summary for HA-GG gels at three GNR concentrations.

Vial No.	GNR Concentration (nM)	HA:GG Ratio	HA to add, m_{HA} (mg)	GG stock to add, $V_{stock,GG}$ (µL)	GNR stock to add, $V_{stock,GNR}$ (µL)	1X PBS to add, V_{PBS} (µL)
1 (Control)	0.0	2.75:0.25	27.5	625	0	375
2	0.7	2.75:0.25	27.5	625	Depends on GNR stock concentration See step 3 in 5.2	Depends on $V_{stock,GNR}$ See step 4 in 5.2

5.3 Add hyaluronic acid to vials

1. Label two new 7 mL scintillation vials with:
   - "2.75:0.25 HA:GG, 0 nM"
   - "2.75:0.25 HA:GG, 0.7 nM"
2. Using the stainless steel micro-scoopula, weigh out and transfer 27.5 mg HA pellets to each vial.
3. Place the original source bottle of HA back in the freezer as soon as weighing is finished.

5.4 Pre-mix gold nanorods with guar gum for stabilization

1. Into a new 1.5 mL microcentrifuge tube labelled "GG-GNRs 0 nM", pipette **375 µL of 1X PBS** and **625 µL of 0.4% w/v GG stock solution**.
2. Vortex-mix the tube for a few seconds.
3. Into another new 1.5 mL microcentrifuge tube labelled "GG-GNRs 0.7 nM", pipette the appropriate volume of, sequentially: 1X PBS, GG stock solution, and GNR solution.
4. Vortex-mix for the tube for a few seconds.

5.5 Prepare gel samples

1. Pipette the contents of microcentrifuge tube "GG-GNRs 0 nM" into the vial "2.75:0.25 HA:GG, 0 nM" that contains HA pellets.
2. Immediately use the stainless steel micro-scoopula to rapidly mix the vial contents.
3. Continue mixing until a gel is formed.
    a. If there are clumps of HA, the sharp edge of the micro-scoopula can be used to break them apart.
4. Repeat steps 1-3 with the microcentrifuge tube "GG-GNRs 0.7 nM" and the vial "2.75:0.25 HA:GG, 0.7 nM".
5. Place the vials in a 50 mL beaker and fill the beaker halfway with water.
6. Place the vial in the bath sonicator and sonicate for 10 minutes.
7. Remove from sonicator and use the micro-scoopula to mix by hand and/or further break up HA clumps.
8. Repeat steps 6-7 until the gel is visually homogeneous. This usually takes a total of 40 min cycling between sonication and hand-mixing.
9. Leave the vials to sit at room temperature overnight to reduce the presence of bubbles. The gel samples are then ready for use.
    a. See Figure 1 for a wide range of gel formulations prepared by this method.

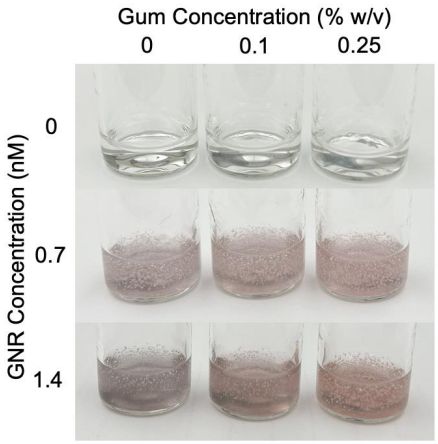


Figure 1: Images of different HA-GG gel formulations prepared by this method.

6.0 Storage and Disposal

The heating performance of the gels is known to degrade over time under ambient conditions. Therefore, it is recommended that gels stored at room temperature be used within 1-3 days of preparation.

Control gel vials (containing no GNRs) can simply be disposed of in regular garbage receptacles. Vials of GNR-containing gels must be transferred to “NANO” contaminated solid waste bins (with appropriate chemical waste labels filled out) as shown in Figure 2. These can be found in both E6-3009 and DC-2726.

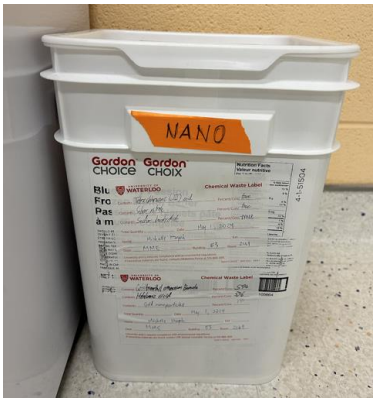


Figure 2: Designated waste bin for nano-contaminated solids.